# Mesoscale Optoelectronic Design of Wire-Based Photovoltaic and Photoelectrochemical Devices

Thesis by

Katherine T. Fountaine

In Partial Fulfillment of the Requirements for the Degree

of

Doctor of Philosophy


CALIFORNIA INSTITUTE OF TECHNOLOGY

Pasadena, California

2015

(Defended May 19th, 2015)

# Acknowledgements

I am incredibly grateful to everyone who made this thesis possible, including those who supported me through these past five years at Caltech and those who helped me get here in the first place. I could not have done it on my own. Thank you.

First, and foremost, I would like to thank my adviser, Harry Atwater. His scientific knowledge, enthusiasm, and creativity truly know no bounds, and I am grateful to have had the opportunity to learn from such a talented scientist. I would also like to thank my committee members, John Brady, Richard Flagan, Hans Joachim (Achim) Lewerenz, and Nathan S. Lewis, for their support and time throughout my graduate years. An extra special thank you to Achim for his guidance and discussions, both scientific and otherwise.

I would also like to thank the many talented graduate students, post-docs, and staff that I have had the opportunity to work with over the past five years, in the Atwater group, JCAP, and the Molecular Foundry. In particular, I am very grateful to Matt Shaner and Shu Hu for sharing experimental results which served as inspiration and basis for much of the theoretical work discussed herein. A special thank you is also due to Mike Kelzenberg and Dan Turner Evans for their pioneering work on many of the theoretical methods used in my thesis. The contributions of Will Whitney and my SURF, Christian Kendall, were also instrumental in the theoretical work on GaAs. I would also like to thank Dr. Shaul Aloni at the Molecular Foundry, Melissa Melendes in the KNI, Chris Chen, Jim Fakonas, Kelsey Whitesell, and Colton Bukowksy for their patience, help and training in nanofabrication methods. I am also excited for and appreciative of the two young graduate students, Sophia Cheng and Phillip Jahelka, who are building on my work—I look forward to following their work. Furthermore, I am incredibly thankful for all of the hard work by the

Atwater administrative assistants, Tiffany Kimoto, Jennifer Blankenship, and Lyra Haas, for always making sure things are running smoothly. The work presented in this thesis would not have been possible without all of these people.

On a more personal note, I want to thank my family and friends. In particular, I am tremendously grateful to my parents, Adrienne and Drew Fountaine, for their unwavering support, love, sage advice, and encouragement. I also want to thank my friends for being my shelter from the storm, especially Colton Bukowsky, Joel Schmidt, Amanda Stephens, Erik Zinn, John Wright, Vanessa E'Voen, Eyrun Eyjolfsdottir, Jacquie Mitchner, Mia Yamauchi, Karina Martinez, Jennifer Othart, and so many more. I feel so lucky to have such an amazing support group. I truly could not have done this without them.

# Abstract

The overarching theme of this thesis is mesoscale optical and optoelectronic design of photovoltaic and photoelectrochemical devices. In a photovoltaic device, light absorption and charge carrier transport are coupled together on the mesoscale, and in a photoelectrochemical device, light absorption, charge carrier transport, catalysis, and solution species transport are all coupled together on the mesoscale. The work discussed herein demonstrates that simulation-based mesoscale optical and optoelectronic modeling can lead to detailed understanding of the operation and performance of these complex mesostructured devices, serve as a powerful tool for device optimization, and efficiently guide device design and experimental fabrication efforts. In-depth studies of two mesoscale wire-based device designs illustrate these principles—(i) an optoelectronic study of a tandem Si|$WO_3$ microwire photoelectrochemical device, and (ii) an optical study of III-V nanowire arrays.

The study of the monolithic, tandem, Si|$WO_3$ microwire photoelectrochemical device begins with development and validation of an optoelectronic model with experiment. This study capitalizes on synergy between experiment and simulation to demonstrate the model's predictive power for extractable device voltage and light-limited current density. The developed model is then used to understand the limiting factors of the device and optimize its optoelectronic performance. The results of this work reveal that high fidelity modeling can facilitate unequivocal identification of limiting phenomena, such as parasitic absorption via excitation of a surface plasmon-polariton mode, and quick design optimization, achieving over a 300% enhancement in optoelectronic performance over a nominal design for this device architecture, which would be time-consuming and challenging to do via experiment.

The work on III-V nanowire arrays also starts as a collaboration of experiment and simulation aimed at gaining understanding of unprecedented, experimentally observed absorption enhancements in sparse arrays of vertically-oriented GaAs nanowires. To explain this resonant absorption in periodic arrays of high index semiconductor nanowires, a unified framework that combines a leaky waveguide theory perspective and that of photonic crystals supporting Bloch modes is developed in the context of silicon, using both analytic theory and electromagnetic simulations. This detailed theoretical understanding is then applied to a simulation-based optimization of light absorption in sparse arrays of GaAs nanowires. Near-unity absorption in sparse, 5% fill fraction arrays is demonstrated via tapering of nanowires and multiple wire radii in a single array. Finally, experimental efforts are presented towards fabrication of the optimized array geometries. A hybrid self-catalyzed and selective area MOCVD growth method is used to establish morphology control of GaP nanowire arrays. Similarly, morphology and pattern control of nanowires is demonstrated with ICP-RIE of InP. Optical characterization of the InP nanowire arrays gives proof of principle that tapering and multiple wire radii can lead to near-unity absorption in sparse arrays of InP nanowires.

# Table of Contents

# List of Figures

# List of Tables

# List of Publications and Intellectual Property

**K.T. Fountaine**, W.S. Whitney, H.A. Atwater, "Resonant absorption in semiconductor nanowires and nanowire arrays: Relating leaky waveguide modes to Bloch photonic crystal modes" *J. Appl. Phys.* 116 (15) 153106 (2014).

**K.T. Fountaine**, H.J. Lewerenz, H.A. Atwater, "Interplay of Light Transmission and Catalytic Exchange Current in Photoelectrochemical Systems" *Appl. Phys. Lett.* 105 (17), 173901 (2014).

**K.T. Fountaine**, W.S. Whitney, H.A. Atwater, "Achieving near-unity broadband absorption in sparse arrays of GaAs NWs via a fundamental understanding of localized radial modes," *Photovolt. Spec. Conf., 2014 IEEE 40$^{th}$* 3507-3509 (2014).

**K.T. Fountaine**, H.A. Atwater. "Mesoscale Modeling of Photoelectrochemical Devices: Light Absorption in Monolithic, Tandem, Si|$WO_3$ Microwires" *Opt. Exp.* 22 (S6) A1453-1461 (2014).

**K.T. Fountaine**, C.G. Kendall, H.A. Atwater. "Near-Unity Broadband Absorption Designs for Semiconducting Nanowire Arrays via Localized Radial Mode Excitation," *Opt. Exp.* 22 (S3) A930-A940 (2014).

M.R. Shaner, **K.T. Fountaine**, S.A. Ardo, R.H. Coridan, H.A. Atwater, N.S. Lewis. "Photoelectrochemistry of Core–Shell Tandem Junction n-$p^+$-Si|n-$WO_3$ Microwire Array Photoelectrodes," *Energy Environ. Sci.* 7 (2) 779-790 (2014).

M.R. Shaner, **K.T. Fountaine**, H.J. Lewerenz. "Current-Voltage Characteristics of Coupled Photodiode-Electrocatalyst Devices," *Appl. Phys. Lett.* 103 (14) 143905 (2013).

S. Hu, C. Chi, **K.T. Fountaine**, M. Yao, H.A. Atwater, P.D. Dapkus, N.S. Lewis, C. Zhou. "Optical, Electrical, and Solar Energy-conversion Properties of Gallium Arsenide Nanowire-array Photoanodes," *Energy Environ. Sci.* 6, 1879-1890 (2013).

**Semiconductor Devices for Fuel Generation**; U.S. Patent App. No.: 13/856,353; Date Filed: 4/3/2013.

**Spectrum-Splitting for Photoelectrochemical Devices**; Invention Disclosure CIT No.: 15-29; Date Filed: 11/25/2014.

**Near Unity Absorption via Dispersive and Resonant Optics in Tandem for Photovoltaic and Photoelectrochemical Devices**; Preliminary Patent App. CIT No.: CIT-7027-P; Date Filed: 10/20/2014.

# Chapter I: Introduction and Background for Solar Energy

## 1.1 Motivation

Currently, fossil fuels account for the majority of global energy usage. The problem with fossil fuels is three-fold: pollution, foreign energy dependence, and finite resources. The replacement of fossil fuels with solar-generated energy reconciles all three of these issues simultaneously, and is arguably the only renewable energy resource that has the potential to meet the entirety of the world's growing energy needs. Today, worldwide power consumption amounts to approximately 17 TW,[1] which is less than 1% of the 23 PW of constant terrestrial, land-based solar insolation.[2,3] Over the past few decades, photovoltaic (PV) devices have been extensively researched and developed as a means of directly converting sunlight to electricity. At the end of 2013, the global installed capacity for PV was roughly 140 GW, and PV accounted for 0.23% of U.S. energy consumption in 2013,[4] more than doubling from 0.1% in 2010.[5] PV is steadily on the rise as efficiencies increase, prices become more competitive with fossil fuels, and public recognition of global warming increases.

### 1.1.1 Solar Fuels

Despite the increasingly favorable outlook for solar-generated electricity, the inherent intermittency of the terrestrial solar resource imposes an upper limit on its role in our current energy market. PV represents a complicated variable supply to the electricity grid, which is dependent upon time of year, time of day, and somewhat unpredictable spatial and temporal variations in weather conditions. Thus, the development of a method to store and, ideally, transport solar energy is critical to enable the solar resource to supply all of or even a significant portion of the global energy needs. One attractive storage and transportation solution is solar-

generated chemical fuels. Typically beginning with water and/or carbon dioxide, photoelectrochemical (PEC) reactions harness the energy from incident solar photons to convert low energy supply molecules to higher energy molecules that are useful fuels, such as hydrogen and carbon-based fuels, including methanol and methane.

Unlike PV, there is no existing industry or fully developed technology for integrated photoelectrochemical devices. Currently, solar fuels can be produced via a two-step conversion process: (i) solar to electric, using PV, and (ii) electric to hydrogen, using an electrolyzer. The combination of these two steps into one integrated PEC device could arguably lower the cost of solar fuels via (i) reducing materials usage and cost in the device and most notably in the balance and (ii) enabling coupled optimization of the individual process steps for higher overall device efficiency. However, the additional materials requirements and operating condition constraints that arise from PEC integration present a unique challenge for researchers.

The Department of Energy, Office of Basic Energy Sciences established the Joint Center for Artificial Photosynthesis (JCAP) in 2010 as an Energy Innovation Hub to address this challenge—the development of a fully-integrated, efficient and earth abundant photoelectrochemical device. Specifically, the first five years of JCAP have focused on solar hydrogen production via light-driven water-splitting. This large science and engineering hub consists of approximately 200 researchers, who are tackling the numerous challenges of this endeavor in parallel and collaboratively. The complete, end-to-end design and fabrication of a PEC device is a complex task, with many issues that need to be addressed, from the atomic scale to the module level. As such, JCAP is structured into eight different subgroups, which range from focusing on individual materials discovery and development, to materials integration, mesoscale device design, and device prototyping.

### 1.1.2 Mesoscale Design

Mesoscale device design bridges the gap between materials integration and device prototyping. The focus of this thesis is mesoscale optoelectronic design of photovoltaic and photoelectrochemical devices, which plays the critical role of optimizing design variables to maximize device efficiency by studying device operation on the length scale of tens of nanometers to centimeters. Specifically, mesoscale design of photoelectrochemical devices affords chemical engineers a unique opportunity for significant contribution because (i) consideration of the three core subjects of chemical engineering—thermodynamics, kinetics, and transport—is crucial to a successful design and (ii) dimensionless number analyses are useful for the simplification of complex system modeling. On these "meso" length scales coupling of light absorption, transport of charge carriers, reactants, products, and electrolyte species, and catalysis occurs and, in a practical device, these phenomena must all function cooperatively. Due to this inherently coupled nature, design of experiments that effectively isolate one phenomenon without altering the nature of the device, is both challenging and time-intensive. For this reason, it is advantageous to employ a mesoscale design approach that capitalizes on synergy between experiment and simulation. This thesis studies the application of this approach to both photovoltaic and photoelectrochemical devices and aims to (i) demonstrate the advantages of using simulation tools to quickly identify and understand limiting factors, (ii) subsequently optimize design parameters, and (iii) apply this knowledge to experimental fabrication.

## 1.2 Background

The following section offers a brief explanation of the governing physics of photovoltaic and photoelectrochemical devices as a basis for understanding the mesoscale device design that makes up the remainder of this thesis. For a more detailed treatment, the reader is referred to

Kittel[6] for solid state physics, Sze[7] for semiconductor device physics, and Bard[8] for electrochemistry. This brief background begins with photovoltaic device operation, addressing the light absorption and charge carrier transport phenomena in semiconductors, and subsequently provides an overview of complete photoelectrochemical device operation, building on photovoltaic device operation to incorporate the phenomena of catalysis, and solution and membrane transport. Finally, the added complexity of mesostructured devices is discussed.

### 1.2.1 Photovoltaic Device Physics

Photovoltaic device operation hinges on the properties of semiconductor materials. Semiconductors are a class of materials that have electrical and optical properties in the grey area between insulators and metals. Material classification at the classical level occurs based on electrical conductivity – metals having nearly infinite conductivity, insulators approaching zero conductivity, and semiconductors lying somewhere in between. Quantum mechanically, the relation between the electronic density of states and the Fermi level position, which is defined as the energy of an electronic state that has 50% probability of occupancy, determines material classification. From this perspective, metals are materials in which the Fermi level lies within a band, which translates to large free carrier populations and conductivities. Conversely, insulators and semiconductors are materials in which the Fermi level lies within a gap in the electronic density of states; smaller gaps (~1 eV at 300 K), in which a small population of free carriers can be thermally excited into the conduction band, designate semiconductors, giving them small yet significant conductivities. These small electronic bandgaps, and the phenomena that arise as a result, are the basis for semiconductor devices, including photovoltaic devices.

The two critical processes in photovoltaic devices are generation and separation/collection of charge. Considering the first of the two, charge generation refers to light absorption, and depends

upon the optical properties of the material and the device structure. In most cases, the electronic bandgap is identical to the optical bandgap. Thus, the bandgap defines the absorption region because only photons with energy greater than the semiconductor bandgap can excite an electron from the valence band to the conduction band. This excitation of an electron creates a hole in the valence band, which carries positive charge, and the two together constitute an electron-hole pair. The creation of energetic electron-hole pairs causes the splitting of the equilibrium Fermi level into the separate electron and hole quasi-Fermi levels, and this difference in carrier energy levels corresponds to the device voltage. The rate and density of charge carrier generation in a specific system is wavelength-dependent and is determined by the incident spectrum, the complex refractive index of the materials, and the device architecture. Sections 1.2.1.2 and 2.2 discuss these details and governing equations in greater detail.

Power generation depends upon the separation and collection of these excited electron-hole pairs as current. The two primary mechanisms for charge transport are drift, driven by an electric field, and diffusion, driven by concentration gradients (see Section 2.3 for the governing equations of charge carrier transport). While differences in the electron and hole effective masses result in slightly disparate diffusion rates, diffusive current does not have any directional charge dependence and is therefore not particularly useful for charge separation. In contrast, carrier charge is directly proportional to drift current, due to its dependence on electric field, and, thus, drift current is typically the driver of charge separation and current collection in photovoltaic devices. Semiconductors do not intrinsically have electric fields, but an electric field can be established at a semiconductor interface with a material of differing Fermi level, creating a “junction.” Many different types of junctions exist; the work discussed herein includes

semiconductor-liquid junctions and buried p|n homojunctions, described in the following sections.

#### *1.2.1.1 Semiconductor|Liquid Junction*

When a semiconductor material is initially placed in contact with a redox couple ($A|A^-$), charge flows across the interface to equilibrate the electrochemical potentials of the semiconductor (the Fermi level, $E_F$) and the solution (redox potential). The transfer of charge creates an electric field at the interface that balances the initial difference in potential. The electric field only persists in a small space close to the interface, called the depletion region in a solid-state material and the Helmholtz layer in solution, in which unbalanced charge persists. The size of the depletion region varies with semiconductor dopant concentrations, with higher dopant concentrations corresponding to smaller depletion regions, typically on the order of 100s of nanometers to microns, because greater charge carrier densities balance inequities in electrochemical potentials over shorter distances. In a metal or solution, which have orders of magnitude higher charge carrier concentrations than semiconductors (~$10^{22}$ $cm^{-3}$), this distance is on the order of a few Ångstroms to nanometers. Therefore, Schottky junctions (a semiconductor|metal junction) and semiconductor|liquid junctions are treated as abrupt, one-sided junctions, in which the entirety of the band bending occurs within the semiconductor.

The creation of a power-producing semiconductor|liquid junction requires the selection of an n-type (p-type) semiconductor with a Fermi level more positive (negative) than the solution redox potential. Note that this thesis adopts the device physicist convention for positive energy direction, as indicated in the diagram of Figure 1. When an appropriate n-type (p-type) semiconductor and liquid come into contact, electrons (holes) flow into solution, causing the semiconductor bands to bend upwards (downwards) with respect to their bulk positions to form

a semiconductor|liquid junction that has an electric field that directs minority carriers into solution to perform an oxidation (reduction) reaction. Figure 1 displays this evolution for an n-type semiconductor|liquid junction.

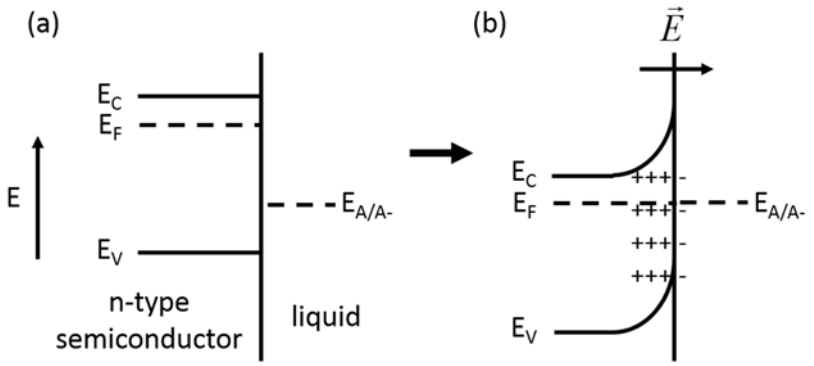


**Figure 1: Energy diagrams for an n-type semiconductor|liquid interface (a) before equilibrium and (b) after equilibrium, illustrating the junction formation process and indicating the direction of positive energy (device physics convention) and the electric field direction in the depletion region.**

For a semiconductor|liquid junction, the initial difference between the redox potential and the semiconductor Fermi level sets the limit on extractable junction voltage, knowns as the built-in voltage, $V_{bi}$. For photovoltaic devices, both of these potential levels are tunable. Conversely, the selection of a desired chemical reaction in photoelectrochemical devices fixes the solution redox potentials, with slight modulation achievable by changing the relative concentrations of the two redox species. Therefore, the photovoltage of a liquid junction is less tunable and can only be controlled, with varying degrees of success, by semiconductor doping level, surface modifiers, and solution pH.[17]

#### *1.2.1.2 Solid-State Junction*

The same principles govern the creation of a semiconductor|semiconductor, buried p|n homojunction, where homojunction refers to the fact that both the p-type and n-type components are the same material. Initially, the Fermi level of the n-type semiconductor is greater than that of the p-type semiconductor; when brought into contact, electrons flow from the n-type semiconductor to the p-type semiconductor to establish equilibrium. The p-type bands bend down and the n-type bands bend up with respect to their bulk positions, establishing an electric field that directs electrons from the p-type into the n-type semiconductor. A large initial Fermi level difference, attainable with high doping concentrations, is desirable for a p|n junction because it generates a greater built-in voltage. Figure 2 illustrates junction formation for a symmetric p|n homojunction.

Unlike semiconductor|liquid junctions, p|n junctions are not abrupt because band bending occurs in both materials. Nevertheless, to improve carrier transport in a device and simultaneously maximize built-in voltage, it is common to create an asymmetric junction where the material type (p or n) with lower mobility is thin and highly doped. This junction design increases the built-in voltage of the device and concentrates the important carrier generation and separation processes in the material with higher mobility, resulting in improved optoelectronic performance. In some cases, these high doping levels result in a junction that approaches an abrupt, one-sided junction.

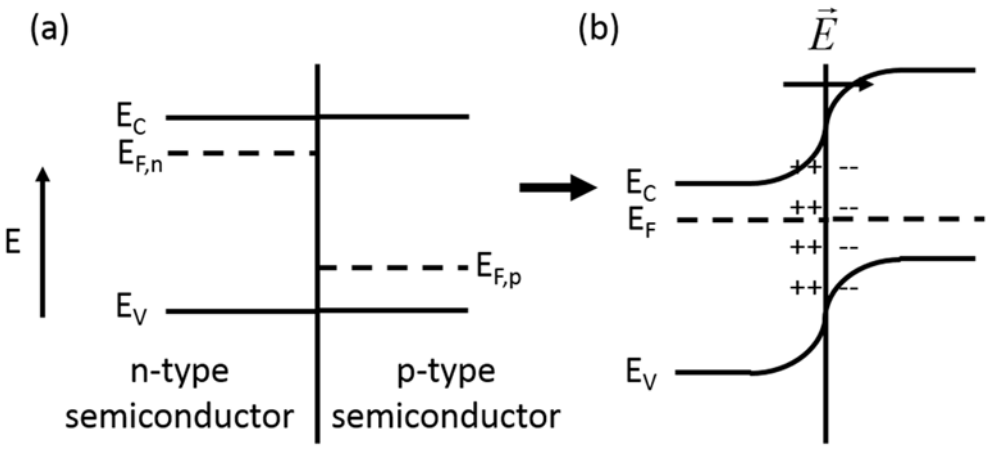


**Figure 2: Energy diagrams for a p|n semiconductor-semiconductor interface (a) before equilibrium and (b) after equilibrium, illustrating the junction formation process and indicating the direction of positive energy (device physics convention) and the electric field direction in the depletion region.**

### 1.2.2 Photovoltaic Limiting Efficiencies

The charge generation and separation processes in a photovoltaic device ultimately determine its efficiency. This section outlines the limiting efficiency for photovoltaic devices. Equation (1) defines the limiting efficiency for a single junction photovoltaic device, $\eta_{PV}$, where $V_{OC}$ is the open circuit voltage, $j_{SC}$ is the short circuit current density, $ff$ is the fill factor, and $P_{in}$ is the incident power.

$$\eta_{PV} = \frac{V_{OC}\, j_{SC}\, ff}{P_{in}} \tag{1}$$

Figure 3 displays current density vs. voltage for an ideal photovoltaic device, normalized to its short circuit current density and open circuit voltage, and thereby illustrates the role of each of the terms in Equation (1), which are defined and discussed in the following paragraph along with equations for ideal behavior (i.e. maximum efficiency).

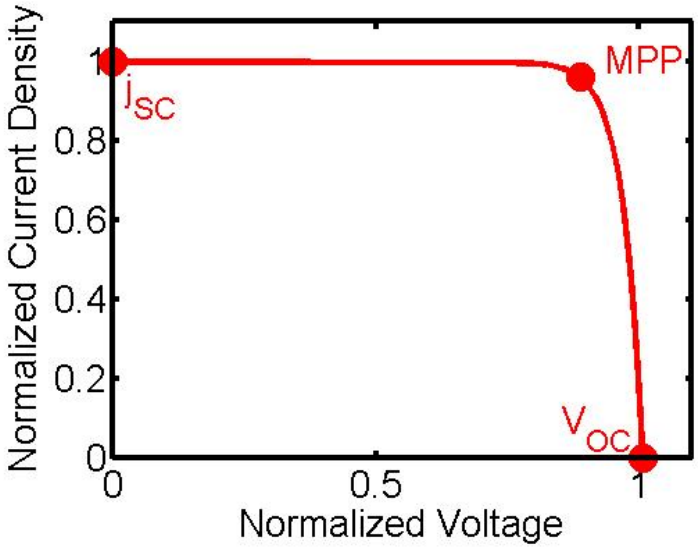


**Figure 3: A normalized *j-V* curve for a photovoltaic device—current density vs. voltage normalized to short circuit current and open circuit voltage, respectively, and illustrating the maximum power point.**

The incident solar spectrum sets the incident power, $P_{in}$. In reality, the terrestrial spectrum varies spatially and temporally, but the AM1.5G spectrum, shown in Figure 4, is a common approximation of average terrestrial solar insolation. The AM1.5G spectrum represents the solar spectrum after passing through 1.5 atmospheres and includes both direct and diffuse light. The short circuit current density, $j_{SC}$, is defined as the current density of the photovoltaic device at zero bias. The upper limit for the short circuit current density in a defect-free material occurs for complete absorption of incident photons with energy greater than the material bandgap, and

complete collection of the generate charge carriers, with the exception of those lost to radiative recombination for the semiconductor black body emission; Equation (2) quantifies this upper limit, known as the "detailed balance" between the incident spectrum (first term) and the black body emission of the photovoltaic device at short circuit (second term), where *q* is the elementary charge, *h* is Planck's constant, *c* is the speed of light in vacuum, $E_g$ is the material bandgap, $k_B$ is the Boltzmann constant, and *V* is the device voltage determined by the quasi-Fermi level separation, which is zero at short circuit.[9] Herein, the solar spectrum is treated as a black body emission at $T_{sun}$.

$$j_{SC} = j(\mathrm{V}=0) = \frac{2\pi q}{h^3 c^2}\left( \int_{E_g}^{\infty} \frac{E^2}{e^{\frac{E}{k_B T_{sun}}} - 1} dE - \int_{E_g}^{\infty} \frac{E^2}{e^{\frac{E-V}{k_B T_{cell}}} - 1} dE \right) \tag{2}$$

The ideal diode equation under light bias, Equation (3), simplifies to Equation (4) to give the open circuit voltage, where $J_o$ is the dark current density and in the ideal, radiative recombination limit is defined by Equation (5), where σ is the Stefan-Boltzmann constant and $\chi$ is a useful variable substitution, $E/k_B T_{cell}$. In real systems, this ideal dark current density is difficult, if not impossible, to reach due to non-radiative recombination mechanisms.

$$V(j) = \frac{k_B T_{cell}}{q} \ln\left( \frac{j_{SC} - j}{j_o} + 1 \right) \tag{3}$$

$$V_{OC} = \frac{k_B T_{cell}}{q} \ln\left( \frac{j_{SC}}{j_o} + 1 \right) \tag{4}$$

$$j_0 = \frac{15\sigma q {T_{cell}}^3}{\pi^4 k_B} \int_{\frac{E_g}{k_B T}}^{\infty} \frac{\chi}{e^{\chi} - 1} d\chi \tag{5}$$

The fill factor is the ratio between the product of the current density and voltage at the maximum power point, $j_{MPP}$ and $V_{MPP}$, to the product of the open circuit voltage and the short circuit current density. The maximum power point is found by calculating the maximum of the product of the voltage, *V*, and the current density, *j*, given by Equation (2).

$$ff = \frac{j_{MPP} V_{MPP}}{j_{SC} V_{OC}} \tag{6}$$

The incorporation of Equations (2), (3), (5), and (6) into Equation (1), results in the detailed balance efficiency for a single junction photovoltaic device as a function of bandgap. Figure 4 displays the detailed balance efficiency for a single junction photovoltaic device illuminated with the AM1.5G spectrum as a function of bandgap (blue, left axis), with the AM1.5G spectral irradiance overlaid (green, right axis). The efficiency falls off at both small and large bandgaps. Small bandgap materials absorb a large portion of the spectrum and, consequently, achieve a higher current density, but the smaller bandgap also results in significant reduction in voltage, and thus, efficiency. Conversely, larger bandgap materials have larger voltages, but smaller current densities because they absorb only a minimal portion of the AM1.5G spectrum. The ideal efficiency peaks at around 33% for materials with bandgaps between 1.1 and 1.4 eV. Silicon (Si) and gallium arsenide (GaAs), the two most common photovoltaic materials, have bandgaps that lie in this optimal range, at 1.1 and 1.42 eV, respectively.

The only losses accounted for in the above limiting efficiency analysis are thermalization of carriers and radiative emission losses. The assumption is that the device absorbs 100% of the incident light and collects 100% of the generated charge carriers, with the exception of the radiative emission losses. However, in a real, traditional planar device, the efficiencies of these two processes, absorption and collection, are often at odds. A real device has a finite thickness, nonzero absorption length, and finite conductivity/collection length. The necessary thickness to achieve near 100% absorption is large, especially for indirect gap materials, like silicon, which have long absorption lengths. Near 100% collection requires a thickness smaller than the collection length, which reflects the electronic quality of the material. Therefore, in a real (planar) device, the absorption length needs to be smaller than the collection length and the thickness set appropriately to maximize device performance and approach the limiting efficiency for a given material.

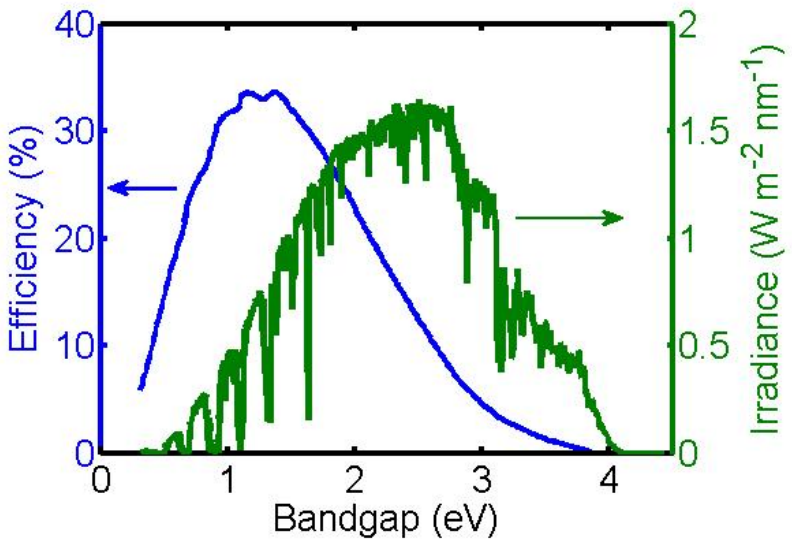


**Figure 4: Detailed balance efficiency for a single junction photovoltaic device illuminated with the AM1.5G spectrum as a function of material bandgap (blue line, left y-axis); spectral irradiance of the AM1.5G spectrum (green line, right y-axis).**

### 1.2.3 Photoelectrochemical Device Physics

A fuel-generating photoelectrochemical device is based upon the same photovoltaic phenomenon as solar cells—the generation and separation of charge. The functional difference is that its final energy product is chemical fuel rather than electrical current, and thus, photoelectrochemical devices have a third critical step: catalysis. The fuel conversion step also places a constraint on the output voltage of the photovoltaic component of the device, which must exceed the thermodynamic potential of the desired reaction. Additional requirements, depending on the device configuration and operating conditions, may include semiconductor band alignment with the reaction redox potentials, and semiconductors and catalyst materials that are stable in strong acidic, basic, reducing and oxidizing conditions. Figure 5 illustrates the basic setup and operation of a planar tandem photoelectrochemical device with an ionic transport membrane for water-splitting.

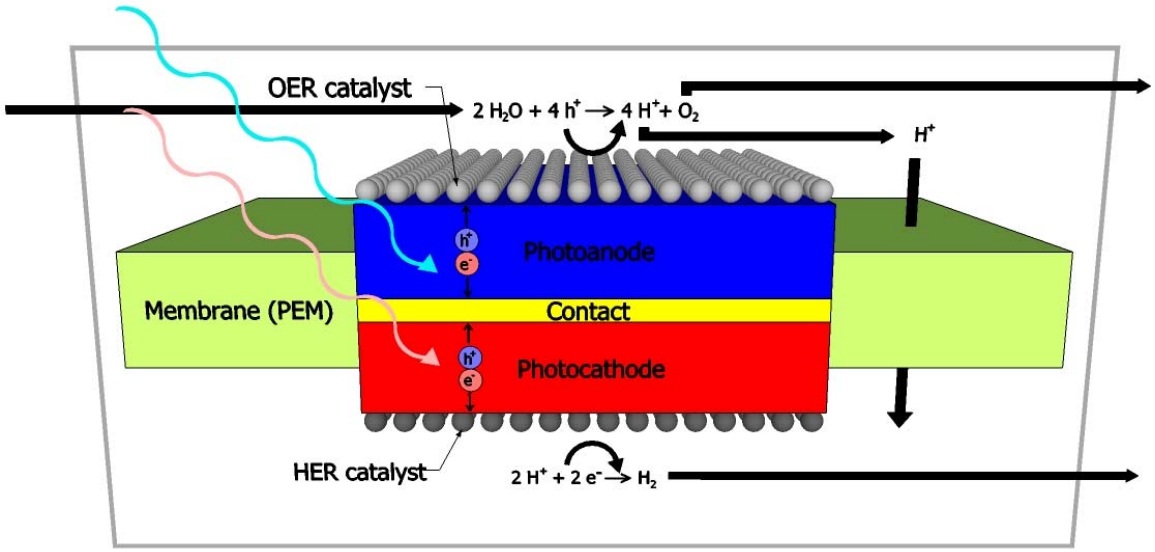


**Figure 5: Planar tandem photoelectrochemical device with a proton-conducting membrane, illustrating the three main processes—charge generation, charge separation and catalysis.**

As previously mentioned, the first five years of JCAP (2010-2015), and consequently the work discussed herein, focus on the water-splitting reaction. The photoelectrolysis of water splits water into hydrogen and oxygen gas, via the following chemical reaction:

$$H_2O_{(l)} \leftrightarrow H_{2(g)} + \frac{1}{2}O_{2(g)} \tag{7}$$

The thermodynamic potential at standard conditions, $\Delta E°$, for this reaction is 1.23 V, and thus, the most basic requirement for the photoelectrochemical (PEC) production of hydrogen is an operating voltage greater than 1.23 V. Water vapor, via 100% humidity air, can replace liquid water and reduces the potential difference slightly to 1.19 V.[10] The Nernst equation, Equation (8), relates this potential to the Gibbs free energy of reaction, $\Delta G^0$, where $n$ is the number of electrons involved in the reaction, and $F$ is Faraday's constant. The absolute values signs remove the directionality associated with the Gibbs free energy because the electrochemical potential difference is an absolute difference, invariant to the reaction direction.

$$\Delta E° = \left| \frac{\Delta G°}{nF} \right| \tag{8}$$

Under non-standard operating conditions, the thermodynamic potential shifts according to Equation (9), where $\Delta E$ is the actual potential difference, $R$ is the universal gas constant, $T$ is temperature, and $a_i$ and $v_i$ are the activity and stoichiometric coefficients of each species, respectively.

$$\Delta E = \Delta E^\circ + \frac{RT}{nF} \ln \prod_i \frac{a_{i,prod}^{\nu_i}}{a_{i,react}^{\nu_i}} \quad (9)$$

The above equation also applies to the half-cell reactions. Equations (10) and (11) represent the two half-cell reactions for water-splitting under acidic conditions with potentials expressed vs. SHE (standard hydrogen electrode). According to Equation (9), the half-cell reaction potentials shift ~60 mV per pH unit, indicating that a pH gradient can significantly alter the thermodynamic potential for the reaction.

$$2H^+ + 2e^- + \frac{1}{2}O_2 \leftrightarrow H_2O \qquad E^\circ = 1.23V \quad (10)$$

$$2H^+ + 2e^- \leftrightarrow H_2 \qquad E^\circ = 0V \quad (11)$$

At standard conditions, photons with an energy of 1.23 eV or greater could theoretically carry out this reaction at the thermodynamic limit. In practice, a greater voltage is necessary to kinetically drive multi-electron reactions and overcome any resistive losses in solution or in the membrane. This kinetic driving force is termed the catalyst overpotential. The Butler-Volmer equation, Equation (12), describes the relationship between the current density, $j$, as a function of the overpotential, $\eta$, for a specific catalyst, where $j_{0,cat}$ is the catalytic exchange current density, $\alpha_A$ and $\alpha_C$ are the charge transfer coefficients for the anodic and cathodic reactions, respectively, and $n_e$ is the electron transfer number. As current density increases, the kinetic overpotential required to drive the reaction also increases.

$$j = j_{0,cat}\left( e^{\frac{\alpha_A n_e F \eta}{RT}} - e^{-\frac{\alpha_C n_e F \eta}{RT}} \right) \quad (12)$$

### 1.2.4 Photoelectrochemical Limiting Efficiencies

The photoelectrochemical device efficiency derives from chemical fuel value, rather than the voltage at which electricity is produced, as in a photovoltaic device. Equation (13) defines the photoelectrochemical device efficiency, $\eta_{PEC}$, where $j_{op}$ is the operating current density, and $\eta_F$ is the Faradaic efficiency. The Faradaic efficiency is the fraction of the current density that produces the desired product.

$$\eta_{PEC} = \frac{j_{op} \Delta E^{\circ} \eta_F}{P_{in}} \quad (13)$$

Examination of the maximum achievable efficiency in photoelectrochemical devices requires the development of a *j-V* characteristic similar to the ideal diode equation, Equation (3), for photovoltaic devices. The series configuration of this device lends itself to a voltage vs. current density, *V(j)*, formulation, as shown in Equation (14), where $V_{PV}$ is the photovoltaic voltage from a variable number of semiconductor junctions, *i*, $\eta_{cat,a}$ and $\eta_{cat,c}$ are the anodic and cathodic overpotentials, respectively, and $V_{series}$ is the series resistance loss from ionic transport through solution and membrane. As previously stated, in order for the reaction to proceed, the total output voltage of the device, $V_{PEC}$, must be greater than the reaction potential, $E_{rxn}$.

$$V_{PEC}(j) = \sum_i V_{PV,i}(j) - \eta_{cat,a} - \eta_{cat,c} - V_{series}(j) \geq E_{rxn} \quad (14)$$

Equation (3), the ideal diode equation, can be substituted for the photovoltaic voltage terms, $V_{PV,i}$. Additionally, the series resistance term is simply expressed as $jR_S$, where $R_S$ is the effective series resistance to ionic transport through the solution and membrane. Applying one of two possible assumptions leads to a simplified inverse formulation of Butler-Volmer kinetics, Equation (12), that replaces the overpotential terms, $\eta_{cat,a}$ and $\eta_{cat,c}$. The first assumption is that the two charge transfer coefficients, $\alpha_A$ and $\alpha_C$, are equal ($\alpha_A=\alpha_C=\alpha$) and this, along with the application of the mathematical identity shown in Equation (15), yields Equation (16).

$$2\sinh\left(\frac{\alpha n_e F\eta}{RT}\right)=e^{\frac{\alpha n_e F\eta}{RT}}-e^{-\frac{\alpha n_e F\eta}{RT}} \tag{15}$$

$$\eta(j)=\frac{RT}{\alpha n_e F}\sinh^{-1}\left(\frac{j}{2j_{0,cat}}\right) \tag{16}$$

Inserting Equation (3) and (16) into (14) yields an analytic expression, Equation (17), for the voltage as a function of current density for a photoelectrochemical device with equivalent anodic and cathodic charge transfer coefficients. Here, the *a* and *c* designations on the catalysis term refer to the anodic and cathodic catalysts, rather than to reaction directions.

$$V_{PEC}(j)=\sum_i \frac{kT}{q}\ln\left(\frac{j_{L,i}-j}{j_{0,PV,i}}+1\right)-\sum_{\mathrm{a,c}}\frac{RT}{\alpha_{\mathrm{cat,a/c}}n_e F}\sinh^{-1}\left(\frac{j}{2j_{0,cat,\mathrm{a/c}}}\right)-jR_s\geq E^0_{rxn} \tag{17}$$

Catalysts that have significantly disparate charge transfer coefficients require the use of a different assumption. Sufficiently large overpotentials justify the omission of the negative exponential term in the Butler-Volmer equation, which then simplifies to the well-known Tafel equation, Equation (18). The Tafel equation is accurate within 1% for $|\eta|\geq 118mV/n_e$.

$$\eta(j) = \frac{RT}{\alpha_{A/C} n_e F} \ln\left(\frac{j}{j_{0,cat}}\right) \tag{18}$$

Inserting Equation (3) and (18) into (14) yields an alternate analytic expression, Equation (19), for the voltage as a function of current density for a photoelectrochemical device operating at a significant overpotential.

$$V_{PEC}(j) = \sum_i \frac{kT}{q} \ln\left(\frac{j_{L,i} - j}{j_{0,PV,i}} + 1\right) - \sum_{\text{a,c}} \frac{RT}{\alpha_{Aa/Cc} n_e F} \ln\left(\frac{j}{j_{0,cat,\text{a/c}}}\right) - jR_s \geq E^0_{rxn} \tag{19}$$

Figure 6 compares the normalized *j-V* curves of a photovoltaic device, calculated from the first term of Equation (17), and a photoelectrochemical device with no series resistance, calculated from the first and second terms of Equation (17). The distinctive feature of the photoelectrochemical device is the exponential increase in current density from open circuit. This exponential "turn-on" originates from the Butler-Volmer kinetics, and demonstrates the detrimental effect of poor catalysis on photoelectrochemical device performance. Slow exponential "turn-on" arises from low catalytic exchange current densities and manifests as lower device current densities at a given operating voltage.

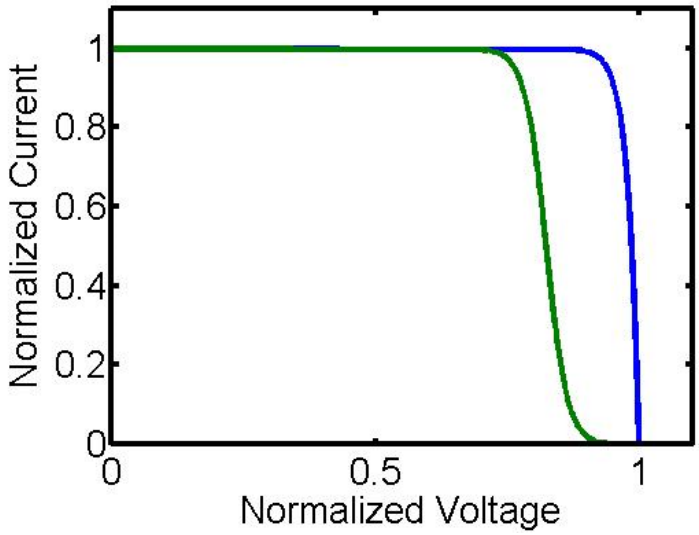


**Figure 6: Normalized current vs. normalized voltage for a photovoltaic device (blue) and a photoelectrochemical device (green) based on Equation (17).**

Insertion of either Equation (17) or (19) into Equation (13) and assuming 100% Faradaic efficiency and AM1.5G illumination establishes a starting point for the calculation of photoelectrochemical efficiencies. However, material specific assumptions must be made about catalyst properties in order to arrive at a bandgap-dependent efficiency, paralleling that for photovoltaic devices (Figure 4). Both catalytic exchange current density and charge transfer coefficients are material and often deposition method specific. Catalytic exchange current density and Tafel slope, the coefficient of Equation (18), are typically experimentally determined. Tafel slopes can vary with voltage; therefore, the alternative assumption of $\alpha$=0.5 is used for the following limiting efficiency calculations based on Equation (17). Additionally, catalytic exchange current densities of 0.01 $mA \cdot cm^{-2}$ and $1x10^{-3}$ $mA \cdot cm^{-2}$ are assumed for the hydrogen evolution and oxygen evolution reactions, respectively, matching top values reported in literature.[11,12,13,14,15] This efficiency calculation assumes 100% Faradaic efficiency and omits solution resistance because, in an ideal device configuration, these losses would be negligible. Figure 7 shows the results of the

calculations for maximum water-splitting efficiency under the aforementioned assumptions for single and dual junction photovoltaic units ($i$=1,2). The contour plot for the dual junction device efficiency has labeled contour lines from 0 to 35% efficiency in intervals of 5%.

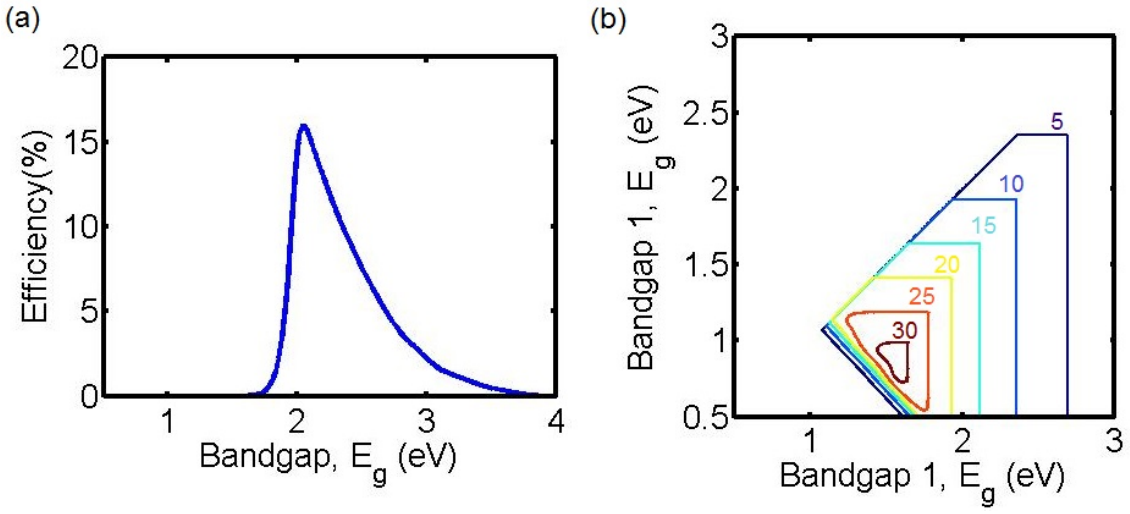


**Figure 7: Single and dual junction photoelectrochemical water-splitting device efficiencies as a function of semiconductor bandgap(s) calculated from Equation (17), assuming AM1.5G illumination, $T$=300 K, $R_s$=0, $n_e$=2, $\alpha$=0.5, $j_{0,cat,a}$=$10^{-3}$ mA·cm$^{-2}$, and $j_{0,cat,c}$=$10^{-2}$ mA·cm$^{-2}$.**

Due to the large voltage needed to kinetically drive water-splitting, a single junction photovoltaic unit requires a large bandgap semiconductor, which severely limits its efficiency. The highest achievable efficiency with a single junction is 16% using a semiconductor with a 2.04 eV bandgap. Dual junction configurations can achieve much higher efficiencies due to their ability to capture a more significant portion of the AM1.5G spectrum with lower thermalization losses and large operating voltages. Based on these calculations, the optimum bandgap combination is 0.92 eV and 1.58 eV, which has an ideal efficiency of 31.8%. Real systems require larger bandgap semiconductors because, in most cases, the ideal diode equation grossly overestimates the attainable photovoltage by disregarding entropic losses from unrestricted angular emission,

incomplete light trapping, and non-unity internal quantum efficiency.[16] Therefore, considering performance of currently available semiconductors which fall about 200-300 mV shy of their ideal voltages, the limiting efficiency of a single junction water-splitting device is around 12% with a 2.25 eV bandgap semiconductor, and that of a dual junction device is around 26% with 1.1 eV and 1.75 eV bandgap semiconductors.

Unlike photovoltaic devices in which the power output can be maximized by simultaneously adjusting the voltage and current density, the reaction potential sets the photoelectrochemical device voltage. Consequently, semiconductor bandgaps more strongly affect photoelectrochemical device efficiencies than photovoltaic device efficiencies. The sharpness of the peak in the single junction photoelectrochemical efficiency (Figure 7) compared with the smooth curve of the photovoltaic efficiency (Figure 4) illustrates this fact and demonstrates the importance of material selection in photoelectrochemical device design.

### 1.2.5 Additional Photoelectrochemical Device Considerations

Both buried junction and semiconductor|liquid junctions have advantages for application in photoelectrochemical devices. A buried solid-state junction presents a means to avoid band alignment and stability requirements (discussed below) and, in some cases, exceed the voltage obtained from liquid junctions because of the ability to tune the Fermi level of both sides of the junction. Nevertheless, these advantages come at the price of more fabrication steps and possibly more material, which increases device cost.

In device configurations with semiconductor|liquid junctions, the semiconductors must also have the appropriate band alignment to carry out the reaction. Using the same energy convention as before, the conduction band of the photocathode, which performs the hydrogen evolution reaction (HER), must be more positive than the $H^+|H_2$ potential; similarly, the valence band of the

photoanode, which performs the oxygen evolution reaction (OER), must be more negative than the $H_2O|O_2$ potential in order for electrons to flow in the correct direction and drive the water-splitting reaction. Figure 8 demonstrates this concept for a tandem photoelectrochemical device.

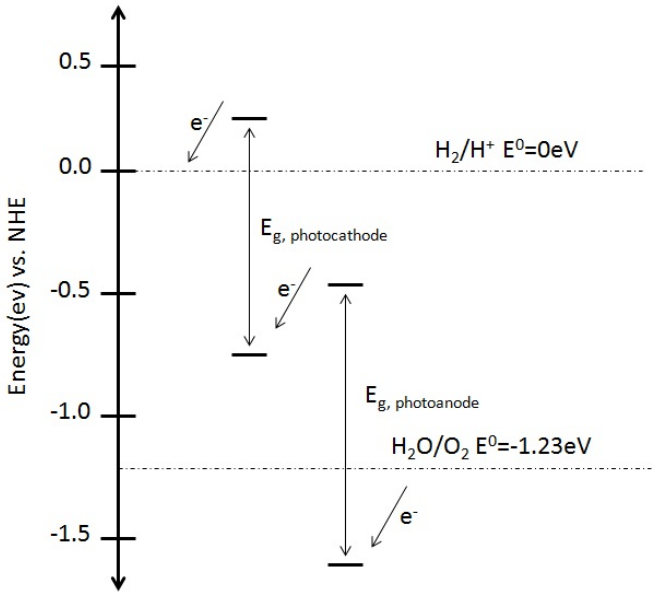


**Figure 8: Energy band diagram for water-splitting with two photoelectrodes in eV on the NHE scale; this diagram is the origin of the term "Z-scheme" for this system.**

More specifically, the quasi Fermi-levels of the photoelectrodes under illumination need to be sufficiently off-set from the redox potentials to supply the kinetic overpotentials. Figure 9 illustrates this point with band diagrams for a tandem photoelectrochemical device that consists of an n-type semiconductor|liquid junction at the water oxidation potential and a buried p|n junction at the hydrogen reduction potential. The band diagram under illumination (Figure 9b) demonstrates the required band alignments for the forward reaction. The hole (electron) quasi Fermi level is more negative (positive) than the water oxidation (hydrogen reduction) potential by a voltage corresponding to the kinetic overpotential. A tunnel junction or ohmic contact exists between the two junctions to facilitate the addition of their photovoltages in series.

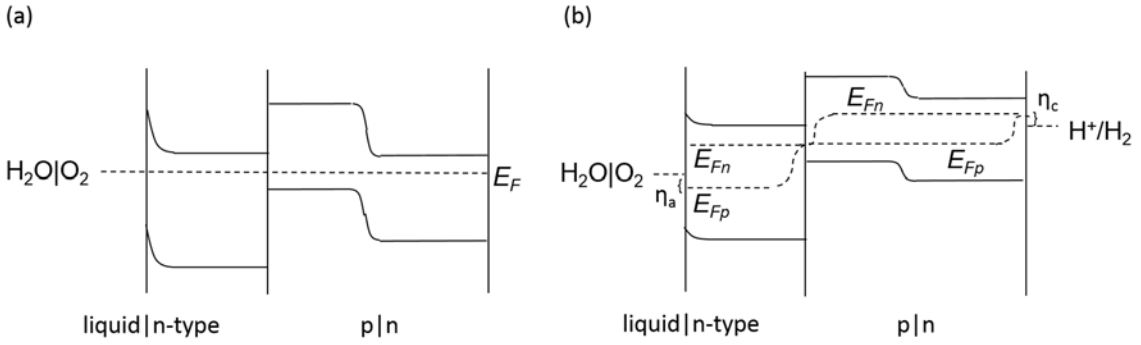


**Figure 9: Band diagrams for a tandem photoelectrochemical device consisting of an n-type semiconductor|liquid junction for water oxidation and a buried p|n junction for the hydrogen reduction reaction (a) in the dark in equilibrium with the water oxidation potential and (b) under illumination with quasi-fermi levels and overpotentials labeled.**

The power curve analysis is a simple and useful way to determine the operating current for a tandem photoelectrode, without integration of the two half cells. Figure 10 illustrates this method by overlaying the separate experimental measurements of the *j-V* curves of the two exemplary photoelectrodes. The maximum attainable operating current (assuming a perfect interface between the two photoelectrodes) is the point at which their *j-V* curves overlap.

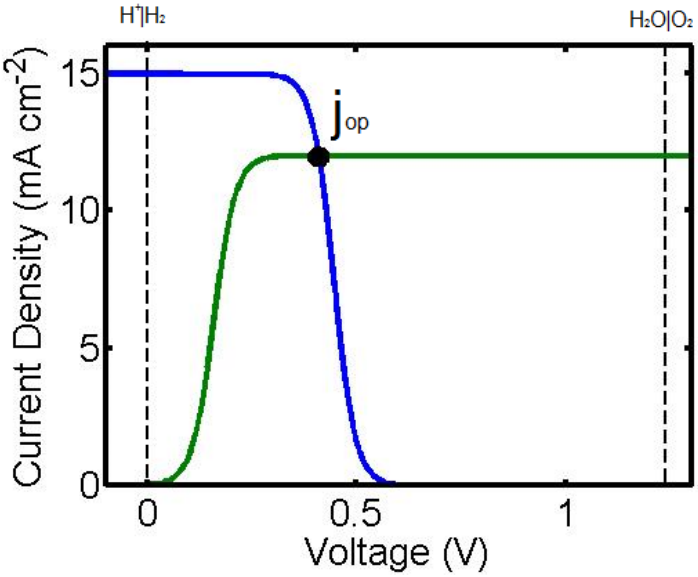


**Figure 10: Power curve, or load line, analysis for two exemplary photoelectrodes.**

For the case of semiconductor|liquid junctions, if the band alignment and photovoltage requirements are not inherently met at pH 0, it is possible to alter the redox potentials by changing the pH per Equation (9), thereby modifying the band alignment. However, the available pH window depends on material stability and catalyst performance. Additionally, this parameter has limited tunability because band edge positions can also be sensitive to pH and solution properties. For example, a liquid junction with p-type silicon with an unmodified surface and the $H^+|H_2$ redox couple has an essentially constant photovoltage over a wide pH range due to surface hydroxyl groups that protonate and deprotenate based on pH.[17]

Stability is also a primary concern. To maintain operation at the same efficiency over long periods, the photoelectrodes and catalysts must be photoelectrochemically stable under illumination and reducing (photocathode) and oxidizing (photoanode) conditions. This stability can be of either kinetic or thermodynamic origin.[18] For complete thermodynamic stability (using device physics convention for energy direction), the reductive and oxidative decomposition potentials, the

potentials at which material corrosion begins, must be more positive than the conduction band edge and more negative than the valence band edge, respectively. For kinetic stability, the reductive and oxidative decomposition potentials must be more positive than the reduction and oxidation reaction potentials, respectively, so that the desired reaction occurs faster than the electrode decomposition.[19] Stability is a particularly difficult criterion to meet for the photoanode; the well-known water-splitting photoanodes that are photoelectrochemically stable are wide bandgap oxides, which do not absorb in the visible, and thus, render low overall efficiencies. To relax this requirement for buried junctions, protective, conductive coatings are currently a topic of intensive research in the photoelectrochemistry community; one such coating is a "leaky" $TiO_2$ layer that can conduct holes.[20]

### 1.2.6 Mesostructured Device Advantages

The work discussed herein focuses on micro- and nano-structured photovoltaic and photoelectrochemical devices. Mesostructured designs, and particularly nanowire and microwire designs, have many advantages for both applications. Figure 11 illustrates a few of these advantages via a comparison of simplified schematics of a planar and wire-based photoelectrochemical device, where the semiconductor is in red and the membrane is in green. The most obvious advantage is that microwire and nanowire arrays can reduce material usage, and thus, cost, especially for sparse arrays. This asset is especially important for devices that incorporate rare and expensive materials, such as III-V compounds. A second advantage is the ability to orthogonalize the directions of light absorption (axially) and carrier collection (radially) by use of a radial junction in vertically-oriented wire arrays. Figure 11 highlights this advantage by schematically contrasting the directions of light absorption and carrier collection for planar and wire design cases.[21] In traditional planar designs, high efficiency devices require the absorption

length, $\alpha_L$, to be much less than the collection length, $L_C$; nanowire and microwire designs decouple these characteristic lengths, enabling higher efficiencies in slowly absorbing and/or low electronic quality materials. Furthermore, nanowires can enable high quality, lattice-mismatched growth.[22] The materials used in traditional planar multijunction devices must have matching lattice constants in order to achieve high quality, epitaxial growth. This lattice-matching requirement dictates certain material combinations and, consequently, bandgap combinations, and these bandgap combinations do not necessarily line up with the maximum device efficiencies. However, nanowires allow for radial strain relaxation, and thus, high quality epitaxial growth with lattice mismatched materials, thereby eliminating material lattice constant as a constraint in materials selection and device design optimization. Nanowires and microwires also exhibit light trapping, and it is this quality that enables sparse arrays, and thus less material, to achieve equivalent performance to planar devices.[23,24] The analysis and manipulation of these optical properties are a primary interest in this thesis.

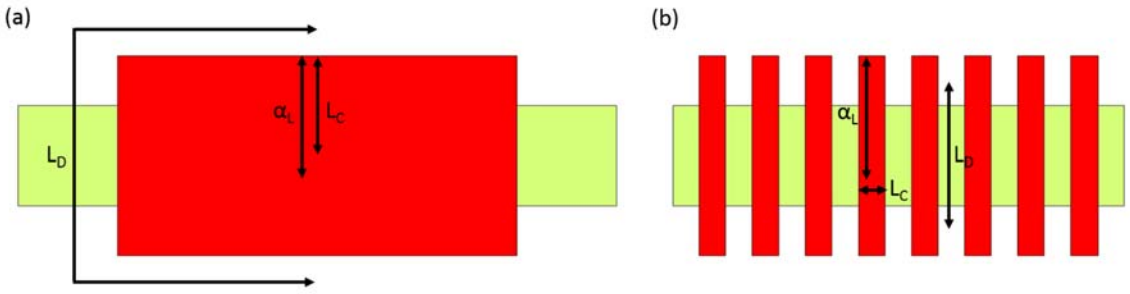


**Figure 11: Simplified schematic of a planar and a wire-based photoelectrochemical device, illustrating the orthogonalization of light absorption and carrier collection and short diffusion pathways that benefit wire-based designs. Red blocks are semiconductor, green blocks are membrane, $\alpha_L$ is the absorption length, $L_C$ is the carrier collection length, and $L_D$ is the diffusion**

**pathway for the electrolyte. More detailed figures for planar and wire-based photoelectrochemical devices can be found in Figure 5 and Figure 16, respectively.**

Additional advantages exist for mesostructured designs for photoelectrochemical devices. Microwires and nanowires have greater surface area for catalyst placement. This advantage can be capitalized on in one of two ways—(i) a higher catalyst loading decreases overpotential, which consequently can enable higher efficiencies or the use of earth abundant catalysts with intrinsically higher overpotentials, and (ii) careful catalyst placement can increase optical transmission through the illumination-side catalyst layer. The next section (Section 1.2.6.1) discusses this tradeoff between optical transmission and catalyst overpotential in more detail. Furthermore, microwire- and nanowire-based designs allow for completely monolithic photoelectrochemical devices by facilitating direct integration of the ion-conducting membrane into the array. This monolithic structure also enables short electrolyte diffusion pathways, as illustrated in Figure 11, which minimizes solution resistance losses.[25]

### *1.2.6.1 Mesostructured Catalyst*

The section considers the influence of an illumination-side catalyst on the performance of a photoelectrochemical device. Specifically, a semi-analytic expression for the influence of mesostructuring the catalyst demonstrates the interplay between light transmission and catalytic overpotential on the optoelectronic performance.

A complete photoelectrochemical device requires both an anodic and a cathodic catalyst, which, in traditional planar device designs such as the one shown in Figure 5, reside on opposite sides of the device; therefore, one of the catalysts lies on the illuminated side of the device. This catalyst is typically metallic in character and, therefore, reflects and absorbs some of the incident light, which results in optical losses. Analytically, this optical loss modifies the ideal diode equation, by

a transmission factor, $f_T$, which represents the incident light intensity reduction and, consequently, the short circuit current density reduction, introduced by the catalyst layer. This factor is always less than one, which lowers device efficiency. Additionally, nanoparticle catalyst layers do not necessarily have equivalent surface area to a planar device. Therefore, a surface area factor, $f_{SA}$, is used to normalize the catalyst surface area to the planar device area, by modifying the catalytic exchange current density term in the Butler-Volmer kinetics. This factor can be greater or less than one depending on nanoparticle size, surface roughness and the deposition amount; factors greater than one decrease the overpotential and improve efficiency. Equation (20) displays these modifications to Equation (17) to account for nanoparticle catalysts on photoelectrochemical device performance.

$$V_{PEC}(j) = \sum_i \frac{kT}{q} \ln\left( \frac{j_{L,i} f_{T,i} - j}{j_{0,PV,i}} + 1 \right) - \sum_{a,c} \frac{2RT}{n_e F} \sinh^{-1}\left( \frac{j}{2 j_{0,cat,a/c} f_{SA,a/c}} \right) - jR_{series} \geq E^0_{rxn} \quad (20)$$

Figure 12 exhibits the effect of modulating both factors, $f_T$ and $f_{SA}$, on the *j-V* characteristic of a tandem (*i*=2) photoelectrochemical device in terms of the normalized voltage ($V/V_{OC}$) and normalized current density ($j/j_{SC}$). A decrease of catalyst surface area by a factor of 10 (blue to red line, $f_{SA}$=0.1) results in a slower catalyst turn-on and a reduction in the output voltage of the tandem device at a given current density. A 40% decrease in the light transmission through the catalyst (blue to green line, $f_T$=0.6) directly results in a 40% decrease in the light-limited current density, which consequently also causes a lower output voltage by the photodiode due to the logarithmic dependence of photodiode voltage on absorbed photocurrent density.

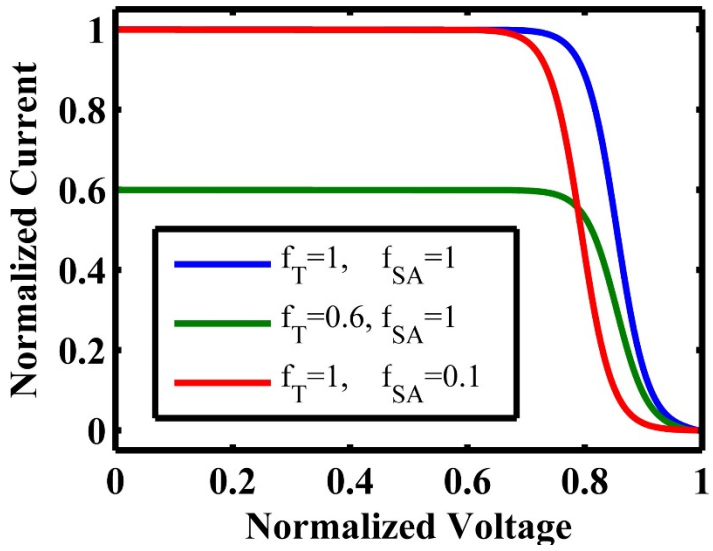


**Figure 12: Normalized current density vs. normalized voltage for (i) $f_T$=1, $f_{SA}$=1 (blue), (ii) $f_T$=0.6, $f_{SA}$=1 (green), (iii) $f_T$=1, $f_{SA}$=0.1 (red), calculated from Equation (20) using $j_L$=18.5 mA-cm$^{-2}$, $j_{0,PV1}$=10$^{-19}$ mA-cm$^{-2}$, $j_{0,PV2}$=10$^{-11}$ mA-cm$^{-2}$, $j_{0,cat}$=0.1 mA-cm$^{-2}$, $n_e$=2, $R_{series}$=0 V.**

Intuitively, complete transmission through the illumination-side catalyst ($f_T$=1) and maximization of catalytic surface area (large $f_{SA}$) optimizes tandem device efficiency. However, in real systems, these two factors cannot be independently optimized. Near unity transmission through a catalyst requires minimal usage of catalyst material, which subsequently implies low catalytic surface area.

To illustrate the interplay between these two factors, $f_{SA}$ and $f_T$, we consider a tandem system consisting of indium gallium phosphide (InGaP) and indium gallium arsenide (InGaAs) photodiodes and rhodium (Rh) electrocatalysts that have been employed in water-splitting half cells[13] with demonstrated high efficiency and stability for water-splitting(Figure 13).[26] Optimization of this system involves careful tuning of catalyst deposition, typically experimentally performed via photoelectrodeposition which generates an interfacial phosphate layer *in situ*.[27] Full-wave electromagnetic simulations of Rh hemispherical particles on a 10 nm interfacial layer of indium

phosphate ($InP_xO_y$) and an optically thick InGaP substrate determined the values of $f_T$ for this system. Section 2.2 discusses these simulation methods in more detail. Table 1 summarizes the results of these simulations for varying Rh particle radius, *r*, and particle spacing, *p*, where $f_{T1}$ is the fraction of light transmitted through the catalyst up to the band edge of InGaP ($E_g$=1.78 eV) and $f_{T2}$ is the fraction transmitted between the band edge of InGaP and InGaAs ($E_g$=1.26 eV). Transmission fractions are appropriately weighted to account for the power distribution of the AM1.5G spectrum. Constant values of *p/r* correspond to equal aerial fill fraction and surface area enhancement factors, $f_{SA}$, for any value of particle radius, making it an ideal parameter to compare across multiple particle sizes. With some exceptions due to particle resonances, the transmission fractions, $f_{Ti}$, increase with decreasing $f_{SA}$ (increasing *p/r* ratio), as expected.

**Table 1: Transmission factor values, $f_{T1}|f_{T2}$, for Rh hemispherical particles with varying radius, *r*, and spacing, *p*.**

| p/r ($f_{SA}$) | r (nm) | | | | | | | | | | | |
|---|---|---|---|---|---|---|---|---|---|---|---|---|
| | 10 | | 25 | | 50 | | 100 | | 150 | | 250 | |
| 2 (1.57) | 0.52 | 0.53 | 0.35 | 0.33 | 0.20 | 0.17 | 0.19 | 0.10 | 0.22 | 0.16 | 0.11 | 0.26 |
| 3 (0.70) | 0.67 | 0.71 | 0.66 | 0.72 | 0.48 | 0.70 | 0.56 | 0.40 | 0.60 | 0.62 | 0.45 | 0.62 |
| 4 (0.39) | 0.68 | 0.72 | 0.68 | 0.73 | 0.56 | 0.71 | 0.64 | 0.57 | 0.61 | 0.70 | 0.55 | 0.61 |
| 6 (0.17) | 0.67 | 0.72 | 0.67 | 0.72 | 0.63 | 0.70 | 0.65 | 0.66 | 0.64 | 0.70 | 0.62 | 0.68 |

Photoelectrodeposited Rh catalyst particles (Figure 13) have a distribution of radii; the optical response, $f_T$, of this system for a given *p/r* or $f_{SA}$ value is approximated by obtaining the $f_T$ value for each particle size and spacing individually, and then averaging the $f_T$ values for a given *p/r* ($f_{SA}$). Incorporation of these $f_T$ ($f_{SA}$) pairs with Equation 5 generates a model of the *j-V* characteristic for this tandem system to demonstrate the effects of varying nanostructured catalyst loading on the device performance.

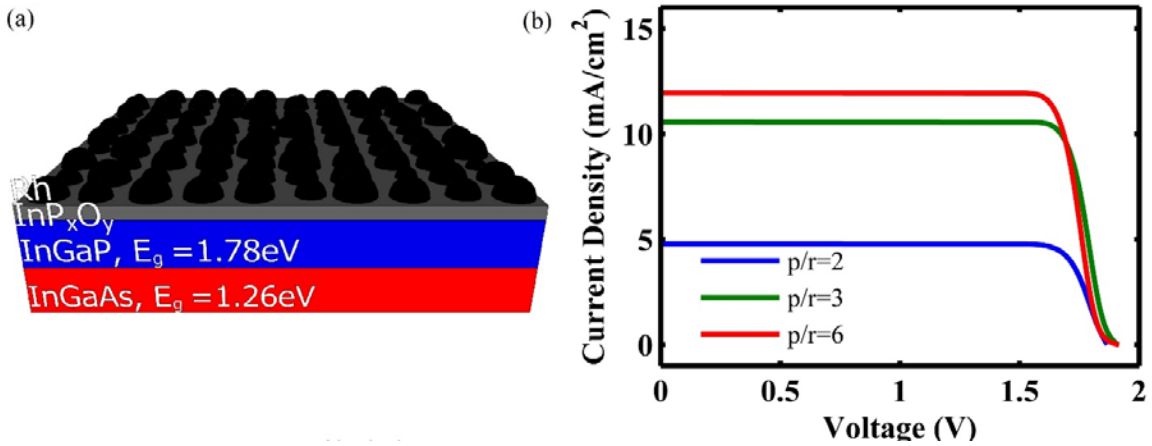


**Figure 13: (a) Schematic of modeled InGaAs|InGaP|interfacial $InP_xO_y$|Rh nanoparticle photoelectrochemical device; (b) current density vs. voltage for three values of nanoparticle spacing divided by particle radius (*p/r*= 2, 3, 6). Equation (20) was used with $j_{SC}$=18.5 mA-cm$^{-2}$, $j_{0,PV1}$=10$^{-19}$ mA-cm$^{-2}$, $j_{0,PV2}$=10$^{-11}$ mA-cm$^{-2}$, $j_{0,cat}$=0.1 mA-cm$^{-2}$, $n_e$=2, $n_d$=1, $R_{series}$=0.**

Figure 13 shows the *j-V* characteristic for a tandem InGaAs|InGaP|Rh photoelectrochemical device for the *p/r* values of 2 (blue), 3 (green), and 6 (red). For close-packed Rh hemispheres (*p/r*=2, blue), the low transmission factor lowers the light-limited current density and, consequently, also decreases the photodiode voltage output. The *p/r* values of 3 and 6 illustrate the main trade-off in nanostructured catalyst design for a tandem photoelectrochemical device. The moderate catalyst loading case (*p/r*=3) has fairly good transmission, and, thus, short circuit

current density, and a sharp catalytic turn-on. For the sparsely-packed Rh particles (*p/r*=6, green), the high transmission factor results in a large light-limited current density, but the catalytic turn-on is slower than in the case of *p/r*=3 due to low catalyst loading.

The optimum catalyst loading is dependent upon the selected materials, device architecture and desired reaction. For the device design selected, the sparse catalyst loading is optimum because it maximizes the device current density and, despite the voltage penalty associated with decreasing the catalyst loading, the voltage supplied by the two photodiodes is more than sufficient to drive the water-splitting reaction ($E_{water\text{-}splitting}$=1.23 V). In general, the device performance is more sensitive to changes in transmission than catalyst surface area because current density depends linearly on the transmission factor and voltage depends approximately logarithmically on catalytic surface area ($\sinh^{-1}(x) \sim \ln(2x)$ for $x$>>1). Ultimately, this brief study of nanoparticle catalyst effects on photoelectrochemical device performance demonstrates the importance of complete device modeling, particularly for mesostructured designs.

# Chapter II: Mesoscale Design Approach and Optoelectronic Simulation Techniques

As previously stated, this thesis focuses on mesoscale optoelectronic design of photovoltaic and photoelectrochemical devices. The goal of mesoscale studies, such as the semi-analytic discussion of the effect of nanoparticle catalysts on the photoelectrochemical device performance in the previous chapter, is to understand the role of and optimize design variables to maximize device efficiency by studying device operation on the length scale of tens of nanometers to centimeters. In photovoltaic devices, light absorption and carrier transport are coupled together. In photoelectrochemical devices, the picture is more involved; light absorption, transport of charge carriers, reactants, products, and electrolyte species, and catalysis all interact. Each of these phenomena must function cooperatively in a practical, efficient device. In real mesostructured systems, device design is quite complex and analytic theoretical studies, or even semi-analytic theoretical studies, are insufficient to develop thorough and accurate understandings of device performance. Similarly, design of experiments that effectively isolate one phenomenon without altering the nature of the device, is both challenging and time-intensive. Therefore, the development of a simulation tool that integrates all phenomena is crucial to accurately model mesostructured device designs. Such a simulation tool can be used synergistically with experiment to serve as a tool to quickly identify and understand limiting factors, optimize design parameters, and subsequently, guide device fabrication efforts. The following sections outline the simulation techniques used for optical and optoelectronic modeling of both photovoltaic and photoelectrochemical mesostructured devices.

## 2.1 Identification of Photoelectrochemical Device Limiting Factors

The development of a complete and integrated model for mesostructured photovoltaic systems is fairly straightforward, as it involves only two main phenomena—light absorption and charge carrier transport. Conversely and as previously stated, a photoelectrochemical device is much more complex. The identification of limiting phenomena in a system enables simplification of the model. Therefore, it is a useful exercise to identify the expected limiting phenomena in a photoelectrochemical device prior to developing a complex mesoscale model. This section covers some general and some design-specific analysis. The specific design considered is the silicon microwire-based design, which is the subject of Chapter 3. Throughout the following discussion, it may be useful to refer to Figure 5 and Figure 16 for complete schematics of planar and wire-based photoelectrochemical devices, respectively.

### 2.1.1 Light Absorption

Regardless of materials discovery and device design, solar insolation sets an inherent limit on solar fuel production rate. Additionally, as demonstrated in Section 1.2.4, which outlines limiting efficiencies for photoelectrochemical devices, the operating current density is the primary efficiency parameter. While this operating current density can be affected by many things, such as low electronic quality materials and poor catalysis, these properties are insignificant if the semiconductor does not first efficiently absorb light. In the previous discussion (Section 1.2.6.1) on nanoparticle catalyst loading, Figure 13 illustrates the crippling effect that low light absorption has on device performance, even in the presence of good catalysis.

### 2.1.2 Carrier Transport

In the low injection level limit in which the photogenerated carrier density is less than the doping concentration, most carrier transport processes scale linearly with carrier density. Therefore,

regardless of the magnitude of photogenerated carriers, a given device configuration with set electronic material parameters collects a set fraction of the photogenerated carriers, and thus, charge carrier transport has a direct effect on device efficiency. The term for this collection fraction is the internal quantum efficiency, IQE, which is the ratio of collected charge carriers to photogenerated charge carriers. This quantity is specific to a given device design, and changes with material properties and geometric design. An intrinsic material property that is related to charge carrier transport is the material diffusion length, which can be used to approximate the collection efficiency of a given design. Equation (21) expresses the diffusion length as a function of the minority carrier lifetime, $\tau$, and the minority carrier mobility, $\mu$, where $D$ is the diffusion length and relates to the mobility via the Einstein relation.

$$L_D = \sqrt{\tau D} = \sqrt{\tau \frac{\mu k_B T}{q}} \tag{21}$$

The minority carrier is the less abundant carrier type (electrons or holes) in a doped semiconductor. In an n-type semiconductor with donor dopants, the minority carriers are holes, and in p-type, they are electrons. Under low level injection conditions, minority carrier transport governs collection efficiency because low excitation levels only slightly perturb the majority carrier concentration from its equilibrium value.

For a planar, 1 mm thick silicon p|n junction, device efficiency increases from approximately 1% to 18% when the minority carrier diffusion length increases three orders of magnitude from 100 nm to 100 µm. In a microwire geometry, the difference is less stark, with the efficiency increasing from approximately 10% to 17% due to the orthogonalization of carrier collection and light absorption in the microwire geometry. The gap between the two cases widens for larger trap

densities in the depletion region.[21] These statistics demonstrate that material electronic properties and device design greatly influence the carrier collection efficiency, and thus, overall device efficiency.

### 2.1.3 Catalysis

As discussed in Section 1.2.4 and demonstrated in detail in Section 1.2.6.1, catalysts impact device operation via their kinetic overpotential, an additional voltage required to drive the reaction. This additional voltage loss needs to be counteracted by photovoltage from the semiconductor junctions. Therefore, large catalytic overpotentials directly translate to the need for large bandgap semiconductors and, consequently, lower absorbed photocurrent densities and device efficiencies. To demonstrate this, Figure 14 shows contour plots of water-splitting tandem photoelectrochemical efficiencies with and without catalytic overpotentials, where the case with catalytic overpotentials matches the values used in Section 1.2.4. These calculations also follow the method used in Section 1.2.4. Although it is perhaps not immediately obvious, the tandem photoelectrochemical efficiency with no catalytic overpotential losses is not identical to that of a tandem photovoltaic because a photovoltaic device has a variable voltage and power output, whereas the electrochemical potential difference required to drive the desired reaction sets the voltage output of a photoelectrochemical device.

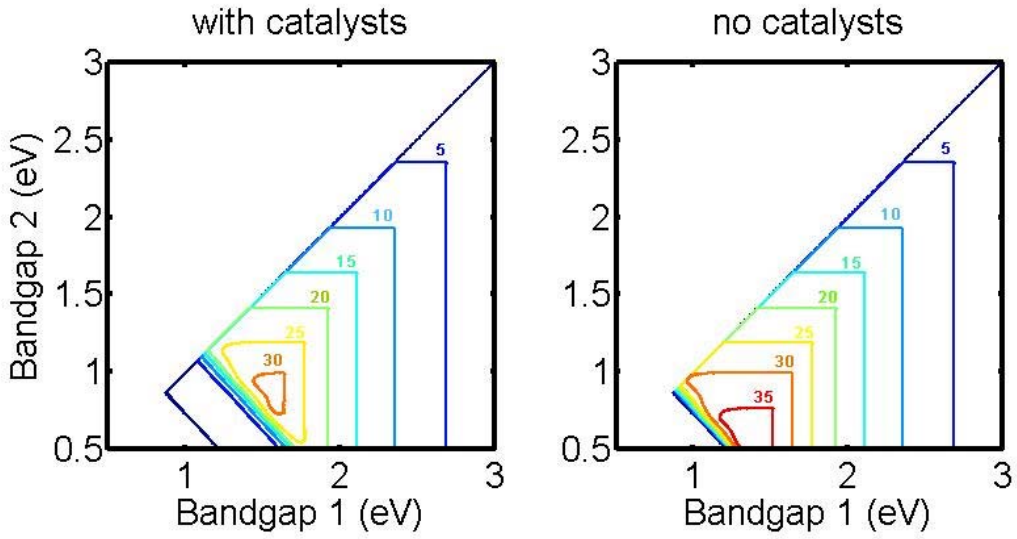


**Figure 14: Contour plots of efficiencies for water-splitting tandem photoelectrochemical devices illuminated with the AM1.5G spectrum for (a) reasonable catalytic overpotentials and (b) no catalytic overpotentials.**

These contour plots demonstrate that decreasing catalytic overpotential increases the maximum efficiency of a tandem photoelectrochemical device. That said, this increase only occurs for small bandgap combinations. For larger bandgap combinations corresponding to maximum efficiencies of 25% and lower, the absence of catalyst overpotentials does not make a noticeable difference because these large bandgaps supply an excess of photovoltage.

Additionally, as mentioned in Section 1.2.6, a mesostructured device design potentially has an increased surface area over that of a planar device. For example, a 7 μm pitch square array of 50 μm long and 1 μm diameter silicon microwires has a surface area enhancement factor of 6.5. This structure can achieve a much larger surface area enhancement factor by, for example, arranging 100 nm radii catalyst particles in a fcc close-packed network that completely fills the microwire array void space; this arrangement corresponds to a surface area enhancement factor of

approximately $10^5$. As demonstrated in Section 1.2.6.1, catalytic surface area enhancements effectively lower the catalytic overpotential. At a $10^5$ enhancement factor in surface area, a catalyst with reasonable performance has negligible overpotential for current densities achievable under the unconcentrated AM1.5G spectrum and could be neglected in a device model.

Therefore, consideration of the specific device design (materials, architecture, desired reaction) to determine whether catalysis is an important phenomenon to include in the device simulation is necessary. In particular, a comparison of the achievable photovoltage for a given bandgap combination and the kinetic overpotential requirements for a given catalytic surface area is instrumental in an evaluation of the effect of catalysis on device efficiency.

### 2.1.4 Reactant and Product Transport

If the reaction is not catalytically-limited, then it is transport-limited. Either charge carrier transport or solution species transport could be the source of this transport limitation. This section examines the latter, considering water, protons, oxygen, and hydrogen transport in acidic conditions. For a device immersed in water, diffusion of water to the OER catalysis site is trivial. Additionally, the assumption of irreversible reactions negates the issue of product transport (oxygen and hydrogen). The assumption of irreversibility is valid for liquid junctions as well as buried junctions with a catalyst. For the case of liquid junctions, the electric field at the junction immediately extracts the charge carriers, thereby preventing the back reaction. For the case of a buried junction with a catalyst, the forward reaction is strongly favored at a sufficient overpotential. Consequently, proton transport is the only potential issue for solution species transport. The most simple and elegant way to analyze whether catalysis or proton transport limits the HER reaction is the examination a modified Damköhler number, a dimensionless

number that compares the diffusive and reaction time scales via a ratio of their fluxes. The diffusive flux, $J_{diff}$, of an ion in one dimension and in the absence of an electric field is found simply from Fick's first law, where $D$ is proton diffusivity in water, $c$ is proton concentration (calculated based on the solution pH), and $x$ is the direction of diffusion. The calculation of the Damköhler number assumes a linear concentration gradient, with the change in concentration being equal to the solution proton concentration, $c_0$, and the distance equal to the maximum length over which protons must diffusion, $L$.

$$J_{diff} = D\frac{\partial c}{\partial x} = D\frac{c_0}{L} \tag{22}$$

The reaction rate, $r$, is the flux of reactant consumed in the reaction and is calculated based on the device current density, $j$.

$$r = \frac{j}{n_e F} \tag{23}$$

The ratio of these two fluxes gives the modified Damköhler number, $K$.

$$K = \frac{r}{J_{diff}} = \frac{jL}{D_0 c_0 n_e F} \tag{24}$$

For a 7 μm pitch array of 1 μm radii microwires, the void space fraction is 0.94, indicating that the semiconductor volume is not confining transport. Using this simplification, protons will have to diffuse a maximum distance of the length of the wire, 100 μm. Therefore, the Damköhler number

is evaluated with $L$=100 µm, $D$=9.31x10$^{-5}$ cm$^2$·s$^{-1}$,[28] $j$=10 mA·cm$^{-2}$ (a reasonable current density for a microwire array), and a pH of 0. These parameters result in a Damköhler number of approximately 0.12. This value demonstrates that the diffusive rate is approximately an order of magnitude faster than the reaction rate, and is unlikely to be the rate-limiting factor in a microwire device at pH 0. This back-of-the-hand calculation can be repeated for other device designs to determine whether the inclusion of solution transport is necessary in a complete and accurate mesoscale simulation. However, it is important to be aware of two additional points; (i) this approximation breaks down for smaller void fractions and more basic pHs and (ii) this approximation is a conservative estimate of transport rates because it does not account for convection.

### 2.1.5 Membrane Transport

The incorporation of a membrane into a photoelectrochemical device is crucial to prevent product crossover and the associated efficiency loss due to the reverse reaction. Membrane materials have lower conductivities than solution, and therefore ionic transport across the membrane is potentially a limiting factor in transport, and can also result in significant voltage losses, depending on the membrane dimensions and conductivity. Nafion is the state-of-the-art proton-conducting membrane that is used in commercial PEM fuel cells; it has a conductivity, $\sigma$, of 0.1 S·cm$^{-1}$ in water at 80˚C.[29] Detailed transport models indicate that a Nafion layer of up to 30 µm may be required to prevent gas crossover.[30] Using these parameters and Ohm's law, the voltage loss associated with membrane resistance in a microwire array structure operating at 10 mA·cm$^{-2}$ is approximately 0.3 mV. This value is negligible and demonstrates that a material with an ionic conductivity similar to that of Nafion can readily support a current density of 10 mA·cm$^{-2}$ without significant voltage losses.

To evaluate membrane transport limitations, the concentration gradient across the membrane is approximated. The Damköhler analysis applied to solution transport in the previous section is not valid in this case because the reactant is not depleted at either interface, meaning that the concentration gradient is an unknown. The calculation of the concentration gradient required to drive proton diffusion across the membrane uses an assumed value for current density to determine the proton flux. A linear approximation of Fick's law, Equation (22), in tandem with this proton flux and the Nernst-Einstein equation, Equation (25), which estimates the diffusion constant, where *z* is the species valence number, *R* is the gas constant, and *T* is the temperature, gives the proton concentration gradient across the membrane.

$$\sigma = \frac{cD(zF)^2}{RT} \tag{25}$$

At 80˚C and a pH of 0, the proton diffusivity in Nafion is $3.15 \times 10^{-4}$ $cm^2 \cdot s^{-1}$. Thus, to support a current density of 10 $mA \cdot cm^{-2}$ in the microwire design, the proton concentration drop across a 30 µm-thick Nafion membrane is $1.05 \times 10^{-6}$ $mol \cdot cm^{-3}$, which is insignificant with respect to the total proton concentration of $1 \times 10^{-4}$ $mol \cdot cm^{-3}$ at pH 0. Again, at a more basic pH, ionic transport across the membrane may become an issue and a more in-depth analysis would be needed to determine whether proton diffusion across the membrane would limit device efficiency because both proton concentration and Nafion's ionic conductivity decrease with increasing pH.

Additionally, because the membrane will result in minimal losses, the prevention of gas crossover makes the incorporation of a membrane in the PEC device design beneficial to overall efficiency.

Based on the preceding analysis, the most important phenomena to model for device optimization of both photovoltaic and photoelectrochemical devices are light absorption and

charge carrier transport, especially in microwire designs. This coupled optoelectronic design is the focus of the remainder of this thesis and the following section outlines the methods used towards this end.

## 2.2 Light Absorption Modeling Methods

Many computational electromagnetic methods exist, including the transfer matrix method (TMM), discrete dipole approximation (DDA), rigorous coupled wave analysis (RCWA), and finite element method (FEM), to name a few. In this work, a finite difference time domain (FDTD) method was selected to simulate light absorption in mesostructured photovoltaic and photoelectrochemical devices. The FDTD method solves Maxwell's equations on a spatial and temporal grid, and while it is somewhat computationally expensive, this method was selected because it is intuitive, versatile, accurate and stable for many different geometries including complex nanostructures. Specifically, the FDTD simulations presented herein used a commercial software, Lumerical FDTD. Equations (26), (27), and (28) express Maxwell's equations for non-magnetic materials, where *D* is the electric displacement, *H* is the magnetic field, *E* is the electric field, and $\mu_0$ is the magnetic permeability of free space, as they are solved in Lumerical.

$$\frac{\partial D}{\partial t} = \nabla \times \vec{H} \tag{26}$$

$$\vec{D}(\omega) = \varepsilon_0 \varepsilon_r(\omega)\,\vec{\mathrm{E}}(\omega) \tag{27}$$

$$\frac{\partial \vec{H}}{\partial t} = -\frac{1}{\mu_0} \nabla \times \vec{E} \tag{28}$$

These full field electromagnetic simulations were performed in 2D for microwire-based designs and in 3D for nanowire-based designs. Computational expense considerations dictated the use of

2D simulations for microwire designs. These 2D simulations extend the microwire infinitely in the third Cartesian direction, creating a thin slab, rather than a microwire. While this approximation does not give completely accurate results, previous studies have indicated that 2D simulations give the correct qualitative trends.[31]

The Lumerical FDTD simulations require the input of the design geometry and the complex, frequency-dependent relative permittivity, $\varepsilon_r(\omega)$, of each material. In the directions perpendicular to the wire axis, periodic boundary conditions for normal incidence and Bloch boundary conditions for other angles of incidence simulated infinitely periodic arrays. Symmetric and antisymmetric boundary conditions, depending on field orientation, replaced the periodic boundary conditions in designs with planes of symmetry. The boundary conditions reduced the simulation region, and thus, the required computational power, by a factor of four when both were employed. In the axial direction, perfectly matched layer (PML) boundary conditions simulated infinite free space, and, in designs with back reflectors, a metal boundary condition simulated perfect reflection at the lower axial boundary. All simulations used plane wave illumination. The 2D microwire array simulations used transverse electric (TE) polarization, defined as the electric field oriented perpendicular to the infinite slab axis. The 3D nanowire simulation results are an arithmetic average of transverse electric (TE) and transverse magnetic (TM) simulation results to emulate unpolarized light. Some initial simulations and optimizations used broadband light sources, but all final results employed single wavelength simulations to ensure the accuracy of the results. The largest source of error that broadband simulations introduce is the use of a polynomial fit to the refractive index; this error is particularly notable near and beyond the band edge for semiconductors. The large frequency span for broadband simulations also enforces a short time pulse; for very short time pulses, simulations could fail to

capture coupling between modes of neighboring structures. Additionally, angular broadband simulations use a constant in-plane wavevector at all frequencies, which translates to a wavelength-dependent angle of injection. The single wavelength simulations used partial spectral averaging (PSA) to eliminate large fluctuations in reflection and transmission that can occur in thin substrates due to interference phenomena such as Newton's rings. PSA calculates a Lorentzian-weighted average of the electric field, with the spectral half-width, $\Delta f$, via Equation (29), where $f$ is the simulation frequency, $d$ is the smallest structure dimension, $n$ is the refractive index of that material, and $\lambda$ is the simulation wavelength.[31] Previous studies demonstrated that the single-wavelength PSA method outperforms the single-wavelength Standard Fourier Transform (SFT) method as well as broadband simulations.[31]

$$\Delta f = \frac{f}{1+\frac{nd}{\lambda}} \tag{29}$$

Figure 15 embodies the above description of Lumerical FDTD methods, displaying an exemplary setup for a 2D simulation of a tandem Si|$WO_3$ microwire structure that is illuminated at normal incidence with TE polarized light.

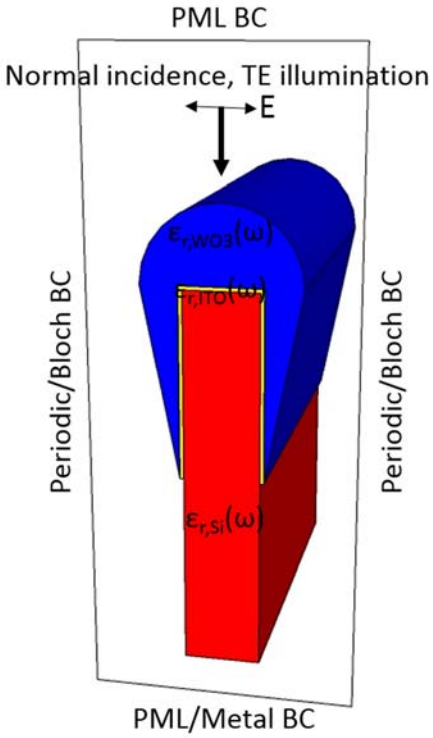


**Figure 15: Schematic of an exemplary Lumerical FDTD setup for a 2D simulation of a tandem Si|$WO_3$ microwire structure, illustrating different boundary condition options (periodic, Bloch, PML, and Metal), the orientation of the fields for a TE simulation, the required material parameter inputs, $\varepsilon_r(\omega)$, and the extension of the structure in the third dimension for 2D simulations.**

The absorbed current density was calculated via two methods, depending on the device design. The first and simplest method was the use of transmission monitors to directly measure the absorption fraction. However, because these transmission monitors are planar, this method was only useful for structures with one absorbing material present or structures in which all absorbing material interfaces could be separated by planar/linear monitors. The second method applied Equation (30) at the simulation frequency, ω, and involved recording the spatially resolved electric field, $E$, and complex relative permittivity, $\varepsilon$, to calculate the absorbed power, $P_{abs}$. This method

was necessary for more complex, multi-material device designs, in which the spatially resolved relative permittivity enabled distinction of materials.

$$P_{abs} = -\frac{1}{2}\omega\left|E\right|^2 \operatorname{Im}(\varepsilon) \tag{30}$$

A spatial integration of this expression for each material gave the fraction of power absorbed in each material at a given wavelength. From these absorption calculations, the device's absorbed current density (*IQE*=1) was calculated by weighting each wavelength with the AM1.5G spectrum and integrating. Performing this procedure at multiple angles of incidence (0 to 60˚) and weighting appropriately allowed the calculation of the average ideal daily power output for a photovoltaic device and the ideal day-integrated hydrogen production for a photoelectrochemical device. Equation (32) summarizes this process, in which $j_{abs,i}$ is the absorbed current density in a specific material, $f_{abs,i}$ is the fraction of power absorbed in a specific material at a given wavelength, $\lambda$, $E_g$ is the material bandgap in nanometers, $P_{AM1.5G}$ is the power density in the AM1.5G spectrum in $W{\cdot}m^{-2}{\cdot}nm^{-1}$ as it is obtained from the NREL website, and the $\lambda/1240$ factor converts power to current.

$$j_{abs,i} = \int_{\lambda=0}^{\lambda=E_g} f_{abs,i}(\lambda)\frac{P_{AM1.5G}(\lambda)\lambda}{1240}d\lambda \tag{31}$$

The spatially resolved electric field and relative permittivity were also necessary for the calculation of spatially resolved photogenerated carrier density for use in the carrier transport simulations, which are discussed in the following section. Equation (32) expresses the photogenerated carrier density, $C_{gen}$, as a function of the electric field, the imaginary part of the permittivity, and Planck's constant, $h$.

$$C_{gen} = \frac{\pi |E|^2 \, imag(\varepsilon)}{h} \tag{32}$$

## 2.3 Carrier Transport Modeling Methods

Synopsys TCAD Sentaurus, a finite element (FE) solver, simulated charge carrier transport. As with computational electromagnetics, many software options exist for charge carrier transport simulation, including software packages such as AFORS-HET, Lumerical (FDTD and Device), and COMSOL, which can perform coupled optoelectronic simulations. In this work, Synopsys TCAD Sentaurus was selected for the charge carrier transport simulations because it is versatile, accurate, and widely accepted and used by the semiconductor industry. Specifically, Sentaurus has advanced functionality and allows the input of detailed parameters, such as energy-dependent and spatially-variant defect levels, which are not available features in less application-specific software.

Synopsys TCAD Sentaurus solves, in a coupled fashion, the Poisson equation and transport equations for charge carriers, both electrons and holes. Equation (33) is the Poisson equation, which relates the electric potential, $\phi$, to the charge density, $\rho$, and the permittivity, and describes band bending in the depletion region. Equation (34) expresses the electron transport equation, where $n$ is the electron density, $G_n$ is the electron generation rate, $\Delta n$ is the excess carrier concentration, $\tau_n$ is the carrier lifetime, and $\mu_n$ is the electron mobility. The hole transport equation is identical except that the diffusion term is negative. In this equation, the generation term, $G_n$, relates to light absorption and typically has spatial dependence, and the $\Delta n / \tau_n$ term describes bulk recombination processes (boundary conditions account for surface

recombination). Within the divergence operator, the first term, $\mu_n nE$, corresponds to drift current, and the second term, $D_n \nabla n$, represents the diffusive current.

$$-\nabla^2 \varphi = \nabla \cdot E = \frac{\rho}{\varepsilon} \tag{33}$$

$$\frac{\partial n}{\partial t} = G_n - \frac{\Delta n}{\tau_n} + \nabla \cdot (\mu_n nE + D_n \nabla n) \tag{34}$$

The 2D cross sections of the structures in Sentaurus precisely matched those constructed in Lumerical FDTD, and radial symmetry was used for the third dimension. To create a coupled optoelectronic simulation, spatially resolved carrier generation rates were calculated from Lumerical FDTD results and Equation (32), and were subsequently input into Sentaurus for carrier transport simulations, using Matlab and the TCL tool within the Sentaurus workbench. Appendix C describes this coupling process in detail and includes critical code for its enactment. Sentaurus is an advanced simulation tool that allows the input of a variety of electronic properties, including doping concentration, lifetime, and surface recombination velocities, to mention a few. The parameters used and device physics enabled in specific device designs are discussed in their respective sections.

Solution of the coupled Poisson and charge carrier equations under illumination and no applied bias gave the short circuit, bulk recombination and surface recombination current densities. Voltage sweeps resulted in complete *j-V* curves.

# Chapter III: Optical and Optoelectronic Design of Microwire-Based Si|$WO_3$ Photoelectrochemical Devices

This study of microwire-based photoelectrochemical devices focuses on optoelectronic effects manifest at the mesoscale, demonstrating how geometric design parameters and optical materials selection can greatly alter the absorption efficiency for a photoelectrochemical device for a given set of photoabsorber materials. Specifically, the results demonstrate that modest geometrical modifications to a microwire photoelectrochemical device design can effect a three-fold increase in light absorption and short circuit current density relative to a nominal baseline design.

This chapter explores design aspects for a tandem, monolithic, microwire-based silicon (Si) | tungsten oxide ($WO_3$) photoelectrochemical device (Figure 16), using an experimentally validated model.[32] The recent development of Si microwire synthesis processes for photovoltaic applications inspired this design.[33] Deposition of a series-connected photoanode material on Si microwires enables the realization of a tandem device with an open circuit voltage suitable for water-splitting.[34,35] This tandem, microwire design affords many advantages, as detailed in Section 1.2.6. Additionally, silicon is an attractive choice for the photocathode material owing to the existing knowledge base for design and fabrication of Si microwire arrays with good fidelity and electronic quality.[33] Despite its wide optical bandgap ($E_g$= 2.6 eV), which limits its current density to approximately 5 mA·cm$^{-2}$,[36] $WO_3$ is an appropriate photoanode material because it is stable under oxidizing and acidic conditions,[37] and is intrinsically n-type and has a suitable band alignment with the water oxidation potential, enabling facile creation of a liquid junction with the $H_2O|O_2$ redox couple. Figure 16(b) and (c) display the band diagrams in the dark in equilibrium

with the water oxidation potential and under illumination for a tandem Si|$WO_3$ PEC device, using a buried p|n junction for Si and a semiconductor|liquid junction for $WO_3$. However, it is important to note that $WO_3$ preferentially oxidizes the anolyte in the presence of HCl, $H_2SO_4$, and $HClO_4$.[38] Regardless, these properties enable experimental fabrication, and thus, comparison of experiment and theory for this design.[32] Furthermore, the results of studying this design reveal how to optimize any microwire-based PEC system that is limited by light absorption in an indirect gap photoanode. A brief study on optimization of a planar device structure that is limited by light absorption in an indirect gap photoanode is presented in Appendix D.

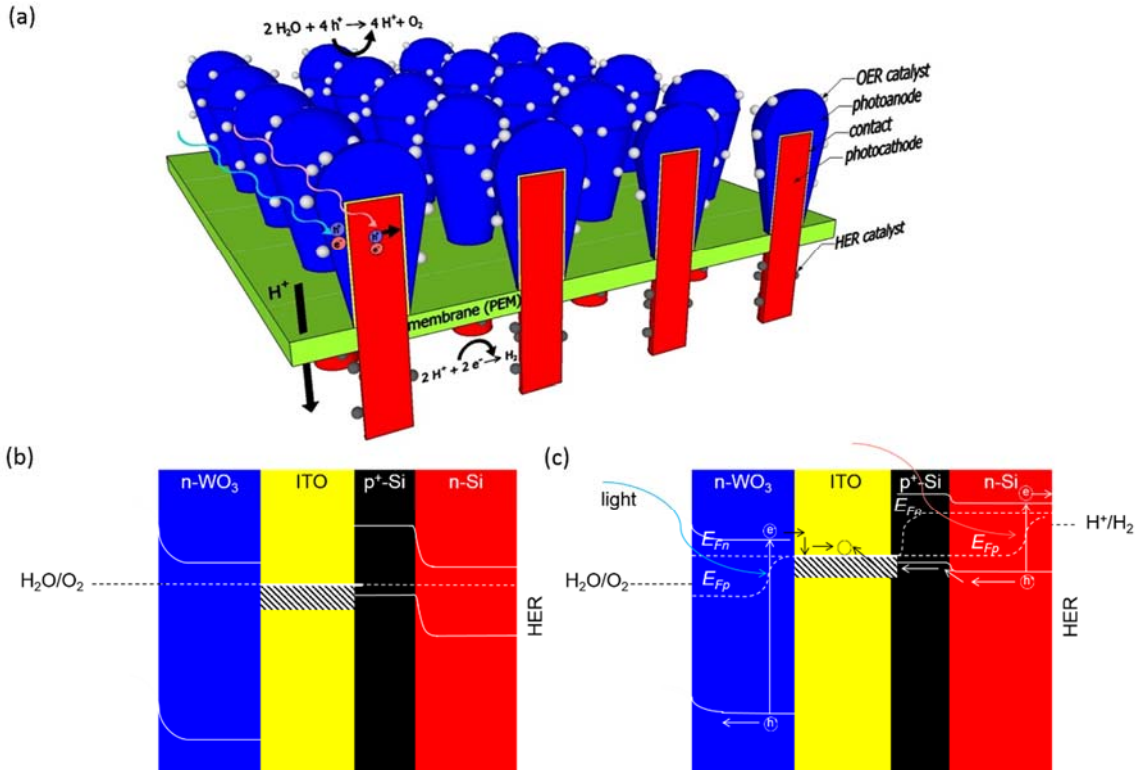


**Figure 16: (a) Diagram of a monolithic, tandem, microwire-based PEC device, including photoanode, photocathode, ohmic contact material between the two photoelectrodes, oxygen (OER) and hydrogen (HER) evolution catalysts, and ion-conducting membrane. Reactions are written for acidic conditions, and therefore, the membrane is labeled as a proton exchange**

**membrane (PEM); (b) band diagram for the structure in the dark and in equilibrium with the water oxidation potential, and (b) band diagram for the structure under illumination.**

## 3.1 Comparison of Experiment and Simulation

The design of an optimized device via simulation begins with the development and validation of the model. For this system, silicon is a well-known material that is consequently readily modeled. $WO_3$ is a difficult material to model because reports in literature of its bandgap, work function and doping concentration vary widely. Therefore, the validation process first matches the experimental and theoretical results of the *j-V* characteristic of a planar $WO_3$|liquid junction to determine $WO_3$ material parameters. Secondly, a comparison of the *j-V* characteristic of a $WO_3$|liquid junction fabricated on Si microwires is performed to validate model parameters. Finally, accurate prediction of which tandem structures (planar and microwire) have sufficient voltage to split water under certain illumination conditions validates the full tandem model.

### 3.1.1 Experimental Fabrication of Planar and Microwire-Based $WO_3$|Liquid Junctions and Tandem Planar and Microwire Si|$WO_3$ Devices

All experimental fabrication for this project was conducted by Matt Shaner. This section summarizes his fabrication efforts towards the comparison of simulation and experiment.

The planar and microwire-based $WO_3$|liquid junctions were experimentally fabricated on a boron-doped $p^+$-Si <111> wafer (<0.005 Ω-cm, Addison), and the planar tandem structure was fabricated on an arsine-doped n-Si <111> wafer (Silicon Inc., 0.7 Ω-cm). The tandem microwire Si|$WO_3$ structure was fabricated on an arsine-doped $n^+$-Si <111> wafer (<0.005 Ω-cm, Addison) with a 400 nm thermal oxide ($SiO_2$) patterned with 3 μm diameter holes spaced 7 μm apart and filled with Cu.

The growth of p-type Si microwire arrays was performed in a chemical-vapor deposition (CVD) furnace at atmospheric pressure using $SiCl_4$ (Strem, 99.9999+%) at 25 sccm flow rate, $H_2$ (Matheson, research grade) at 500 sccm flow rate, and $BCl_3$ (Matheson, 0.25% in $H_2$) at 1 sccm flow rate for 20 min or $PH_3$ (Matheson, 100ppm in $H_2$) at 0.3 sccm flow rate for 9 min. This process produced Si microwires that were 40-70 μm in length, 2 μm in diameter and acceptor doping densities on the order of $10^{17}$ $cm^{-3}$. Following growth, the samples were cooled to approximately 200 °C under a 500 sccm flow of He.

To create the boot and prevent junction shorting for the tandem microwire structure, the microwire arrays were then cleaned using a 6:1:1 (by volume) $H_2O$:HCl (fuming, aqueous):$H_2O_2$(30% in $H_2O$) metal etch (RCA 2) for 20 min at 60 °C. The samples were then subjected to a 15 s etch in buffered hydrofluoric acid, an $H_2O$ rinse, an organic (piranha) etch in 3:1 $H_2SO_4$ (99.6%, aqueous):$H_2O_2$ (30% in $H_2O$) for 10 min at room temperature, and an $H_2O$ rinse. Following a 30 s etch in 10% BHF and a rinse with $H_2O$, a 150 nm thick $SiO_2$ layer was grown via dry thermal oxidation in a tube furnace at 1050 °C under an $O_2$ atmosphere for 2.5 h. A 15 μm thick PDMS layer was deposited at the base of the wires by spin coating a solution, consisting of 1.1 g of polydimethylsiloxane (PDMS, Sylgard 185, Dow Corning) and 0.1 g of PDMS curing agent dissolved in 5 mL of toluene, on the sample at 3000 rpm for 30 s, followed by a 30 min cure in vacuum oven at 150 °C. These PDMS-infilled arrays were submerged in BHF for 5 min, to remove the $SiO_2$ on the exposed microwire surfaces. The PDMS was removed by a 30 min soak in 3:1 N-methyl-2-pyrrolidone (NMP):tetrabutylammonium fluoride (TBAF), followed by a 30 s rinse with $H_2O$. The samples were then dried under a stream of $N_2$(g). Residual organics were then removed by a 10 min etch in a piranha solution. Following the formation of the $SiO_2$ boot, a boron-doped $p^+$-Si radial emitter layer was formed on the n-Si microwire arrays to create a p|n junction in the

microwires. The emitter layer was formed via exposure of the samples in a CVD furnace to a 20:400 sccm flow of $BCl_3$ (Matheson, 0.25% in $H_2$):$H_2$(Matheson, research grade) at 950 °C for 30 min, immediately following a 30 sec etch in 10% BHF. This emitter layer formation step was also conducted on the planar n-type Si wafers to form a p|n Si junction for the planar tandem structure. The layer thickness was estimated to be approximately 200 nm. The samples were then rinsed with $H_2O$ and dried under a stream of $N_2$(g).

Prior to ITO deposition, the Si wafers (planar structures) and microwire arrays were prepared by a 15 s etch in 10% buffered hydrofluoric acid (BHF) to remove the native oxide and subsequently rinsed in Millipore water and dried with nitrogen gas. Immediately following this preparation, a 400 nm layer of ITO was sputtered (48 W, 3 mTorr, 20:0.75 sccm Ar:10% $O_2$ in Ar) by DC magnetron sputtering under 10 W of substrate bias to facilitate conformal deposition on the microwire sidewalls). Then, n-$WO_3$ was electrodeposited from a tungstic peroxy-acid solution.[38] Briefly, 4.6 g of tungsten powder (0.6-1μm, 99.99%, Sigma Aldrich) was dissolved in molar excess (60 mL) of $H_2O_2$ (30% in $H_2O$). Excess $H_2O_2$ was dissolved by addition of a trace amount of Pt black (99.9%, Sigma Aldrich) for 24 h. The $H_2O_2$ concentration was monitored by peroxide test strips (EM Quant) until final peroxide concentration was <30 ppm. A concentrated stock solution was made by addition of 80 mL of $H_2O$ and 60 mL of isopropyl alcohol (IPA) to the as made solution. To increase its lifetime, the stock solution was protected from light and stored at 2°C in a refrigerator. A 3:7 IPA:$H_2O$ mixture was used to dilute the stock solution (3:2 IPA:$H_2O$ mix:stock solution) to generate the deposition solution. Stock solutions were used for one week before and thereafter were freshly prepared. All ITO-coated samples were used as prepared for deposition of $WO_3$, and were contacted directly to the ITO layer using a flat alligator clip. Deposition of $WO_3$ on n|$p^+$-Si and p-Si microwire arrays was performed potentiostatically at -0.5 V vs Ag|AgCl for 60 min. After

deposition, all samples were annealed in air at 400 °C for 2 h. This process formed monoclinic $WO_3$, as confirmed by X-ray diffraction data.

Figure 17 summarizes a simplified fabrication process for the most complex structure, the tandem microwire Si|$WO_3$ device, and Figure 18 displays scanning electron microscopy (SEM) images of the resulting arrays.

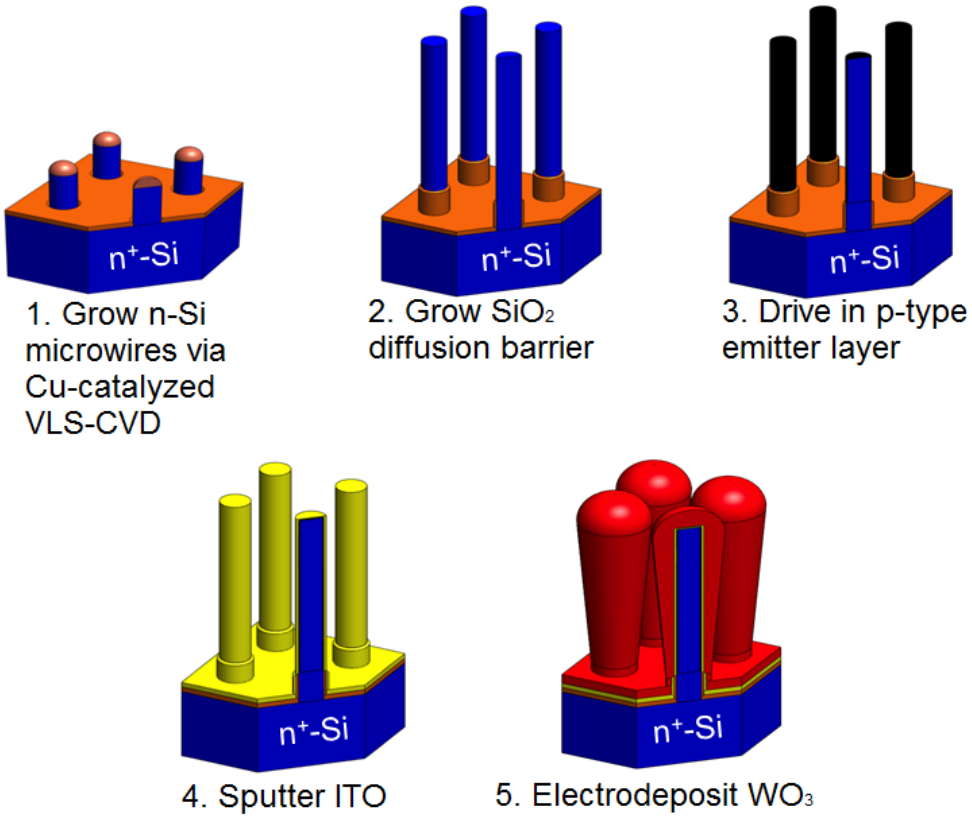


**Figure 17: Simplified fabrication process flow for the tandem microwire Si|$WO_3$ device.**

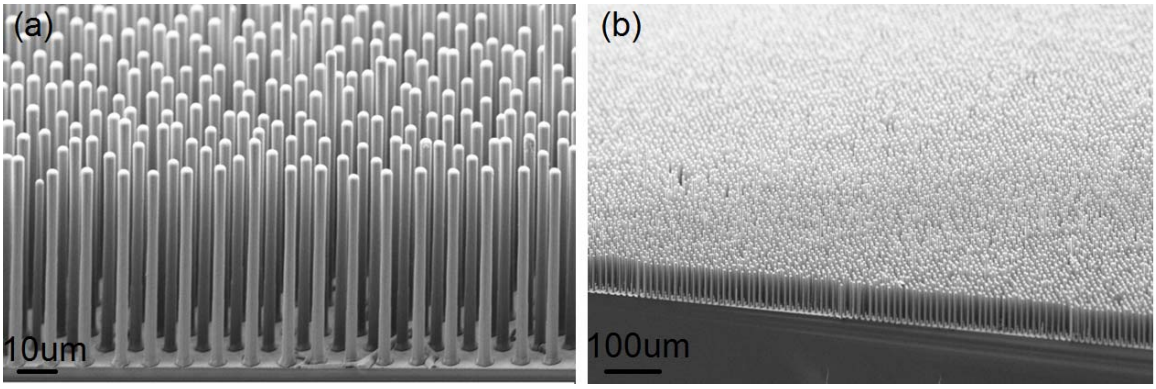


**Figure 18: SEM images of the tandem microwire Si|$WO_3$ structures at two different magnifications.**

To establish an electrode from these structures, ohmic contact was made to the silicon substrate by scratching the back-side of the sample and contacting with an In-Ga eutectic mixture (99.99%, Alfa-Aesar). Exposed In-Ga (Si electrodes) was affixed to a coiled Cu-Sn wire with Ag paint (SPI 05001-AB). The active area was defined with epoxy (Loctite Hysol 9460) and the entire electrode was sealed with epoxy to the bottom of a glass tube (6mm O.D.). The electrode orientation, down- or side-facing, was determined by the orientation of the coiled wire that protruded from the glass tube. Geometric areas were measured by scanning the active area, and using software (ImageJ) to calculate the area.

The photoelectrodes were tested in a three electrode potentiostatic configuration, immersed in 1 M $H_2SO_4$(aq) (trace metal grade, Fischer Scientific) saturated with $H_2$(g) (research grade, Air Liquide), and using a Biologic (SP-200) potentiostat in a two-compartment cell (compartments are referred to as the anode compartment and the cathode compartment) that contained an epoxied (Loctite Hysol 1C) quartz window on the anode side and a Nafion® (0.05 mm thick, Alfa Aesar) membrane separator between the compartments. Illumination was produced by a Xe lamp (Oriel 67005, Newport Instruments) with an AM 1.5G filter (Newport Instruments 81094) that produced

light intensities of either 1 (100 mW-cm$^{-2}$) or 11 (1080 mW-cm$^{-2}$) suns on a calibrated Si photodiode. The concentration value (11x) was determined using the AM1.5G spectrum; however, based on the AM1.5D spectrum, it was a 12x concentration. Calibration was performed such that the highest light intensity anywhere in the cell was at the cited light intensity and the position of the photodiode at this light intensity was marked to assure sample positions were equivalent. Optical concentration was achieved using a plano-convex lens (Thorlabs LA4984). The spot size (~1 cm$^2$) overfilled all samples tested (~0.1 cm$^2$). Three-electrode measurements were conducted with the working electrode in the anode compartment open to air, a SCE reference electrode (CH Instruments, CHI150) in the anode compartment, and a Pt mesh counter electrode in the cathode compartment at scan rates of 20 mV-s$^{-1}$. Pt disc (0.0314 cm$^2$) three-electrode measurements were performed with the Pt disc in the cathode compartment and with the SCE reference and the Pt mesh counter electrodes in the anode compartment. For Pt disc measurements, the cathode compartment was saturated with either Ar(g) (research grade, Air Liquide) or $H_2$(g) (research grade, Air Liquide) by bubbling for 15 min before testing. All the measurements were referenced to the potential of the RHE ($E(H^+|H_2)$), obtained empirically using the Pt disc electrode under 1 atm of $H_2$(g), -0.247 V vs. SCE.

### 3.1.2 Simulation of Planar and Microwire-Based $WO_3$|Liquid Junctions and Tandem Planar and Microwire-Based Si|$WO_3$ Devices

Figure 19 displays the renderings of the experimentally fabricated structures (planar and microwire), as they were constructed in the coupled optoelectronic simulations described in this section. The material coloring scheme is consistent between (a) and (b), thickness labels on the right side of (b) are a constant conformal coating around the wire, and the n$^+$-Si substrate has an unspecified thickness because it was modeled as infinitely thick in optical simulations and was neglected in the carrier transport simulations.

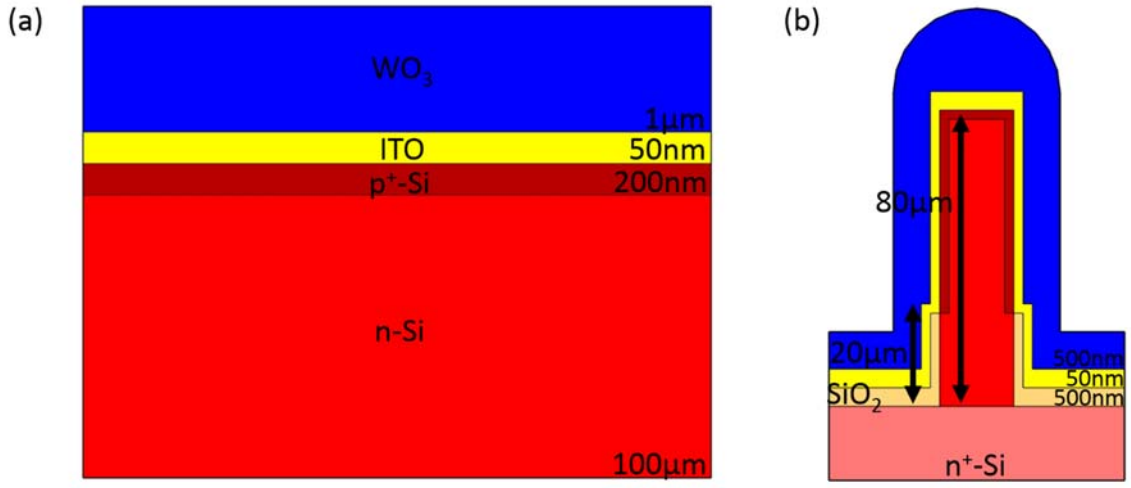


**Figure 19: (a) Planar and (b) microwire schematics of the simulation rendering of the experimentally fabricated structures; materials coloring scheme is consistent between (a) and (b); thickness labels on the right side of (b) are for conformal coatings; the $n^+$-Si substrate in (b) has unspecified thickness and was rendered as infinite in optical simulations and neglected in carrier transport simulations.**

Light absorption simulations in Lumerical FDTD used complex refractive indices that were experimentally measured, via ellipsometry for $WO_3$ (A. Leenheer) and ITO (D. Turner-Evans), and in the integrating sphere for silicon (M. Kelzenberg). The void space between microstructures was modeled as air in the results presented below, but immersing the structures in water, which has a low refractive index and does not significantly absorb in the UV-Vis-NIR, resulted in insignificant changes in absorbed current density (~1-2%). Investigation of light propagation and absorption in these microstructures used single wavelength, full field (*E*, *H*) 2D electromagnetic simulations, ranging from 350 to 1100 nm in 50 nm intervals.[31] The structures were meshed with 20 mesh boxes per wavelength. Section 2.2 discusses the optical modeling methods in more detail.

The carrier transport simulations in Synopsys TCAD Sentaurus modeled a single n-$p^+$ Si homojunction and an n-$WO_3$|$E^0(O_2|H_2O)$ liquid junction separately. The silicon simulations used the built-in material parameter file for Si with modified time constants ($\tau_n(N_A=10^{20}\,cm^{-3})=3x10^{-6}$ s; $\tau_p(N_D=10^{17}\,cm^{-3})=1x10^{-3}$ s). The planar silicon $p^+|n$ junction was constructed with a 100 μm thick n-region with $N_D=10^{17}cm^{-3}$ and a 0.2 um thick $p^+$-region with $N_A=10^{20}$ $cm^{-3}$. The $p^+|n$ junction microwire array consisted of an 80 μm long wire with a 200 nm radial junction, with a 15 μm $SiO_2$ boot to emulate the experimentally fabricated structure. The quasi-neutral bulk of the planar n-Si had standard mesh sizes of 500 nm transverse and 5 μm parallel to the junction. Near the ohmic contact with n-Si, the mesh was refined to 500 nm and 100 nm, and near the junction, the mesh was refined to 500 nm and 20 nm, to accurately model band bending in these regions. The *j-V* characteristics of this structure were obtained by first solving for the *V*=0 case in the dark. Subsequently, the voltage was stepped at 0.01 V intervals in both the positive and negative directions, to obtain the dark *j-V* behavior. The carrier generation rate from Lumerical was then applied to extract the *j-V* characteristics in the presence of illumination. Similarly, the *V*=0 case in the light was solved first, and then the voltage was stepped at 0.01 V intervals, to obtain the light *j-V* performance. Shockley–Reed–Hall (SRH) recombination was used for these simulations.

The $WO_3$ layer used the built-in "oxide as semiconductor" material parameter file with the following parameters modified and their values in parentheses: bandgap ($E_g$=2.6 eV), work function ($\chi$=4.4 eV), relative permittivity ($\epsilon_r$=5.76), conduction- and valence-band density of states ($N_C=1.8 \times 10^{19}\,cm^{-3}$, $N_V=7.1x10^{19}\,cm^{-3}$), time constant ($\tau_n=\tau_p=10^{-8}$ s) and mobility ($\mu_n=\mu_p=40\ cm^2 \cdot V^{-1} \cdot s^{-1}$). The bandgap was experimentally determined from absorption measurements using an integrating sphere and a Tauc plot with *r*=2 for indirect, allowed transitions by A. Leenheer. The relative permittivity was calculated from ellipsometric measurements of the complex refractive

index. The work function was chosen based on reports found in the literature.[25] The density of states, *N*, were calculated from *m**, the effective mass of holes in the valence band and of electrons in the conduction band, shown for electrons in the conduction band in Equation (35).

$$N_C = 2\left(\frac{2\pi m_e^* k_B T}{h^2}\right)^{3/2} \tag{35}$$

Effective masses in the conduction band have been reported to be ~$0.8m_{0,}$[26] where $m_0$ is the mass of a free electron. Reported density functional theory calculations of the $WO_3$ band structure predicted that the valence band has less curvature than the conduction band, indicating heavier holes and leading to an estimate of 2 $m_0$ for the hole effective mass.[27] The mobility values were also taken from the literature.[26] Preliminary experimental measurements indicated a diffusion length of 1 μm, thereby determining the time constant.

The $WO_3$|liquid junction was modeled as a Schottky junction, with the metal work function equal to the water oxidation redox potential, $\chi$=5.68 eV, which was in contact with a 1 μm thick slab of $WO_3$ in the planar structure and a 1 μm conformal coating in the microwire structure. A value of $N_D$=$10^{15}$ $cm^{-3}$ was chosen to match the experimentally observed short-circuit current density and open-circuit voltage. Mesh sizes of 10 nm and 250 nm were used perpendicular and parallel to the junction, respectively. The method used to obtain the dark and light *j-V* behavior was identical to that used for modeling the Si junction. These simulations used Shockley-Reed-Hall recombination and thermionic emission physics.

Load line, or power curve, analysis was used, as described in Section 1.2.5, to determine the operating current density (if any) of the tandem devices based on their separate *j-V* performances.

The two photoelectrode curves are measured separately and then overlaid. The maximum attainable operating current density, assuming a perfect contact interface between the two photoelectrodes, is the point at which their *j-V* curves overlap. Figure 22 displays this type of analysis.

Chapter 2 provides further details on coupled optoelectronic simulation methods with Lumerical FDTD and Synopsys TCAD Sentaurus.

### 3.1.3 Comparison of Experimental and Theoretical Results for Planar and Microwire-Based $WO_3$|Liquid Junctions

The planar and microwire $WO_3$|liquid junctions were fabricated and their *j-V* performance was measured and simulated as described above. Figure 20 displays their theoretical (green) and experimental (blue) *j-V* curves, where (a) shows the planar behavior and (b) shows the microwire-based behavior.

In Figure 20, the open circuit voltages of experiment and theory achieve a reasonable fit, while the fill factors and short circuit current densities are not well-matched. The light-limited current density, at much more positive voltages (not shown), matches between experiment and theory, indicating that the light absorption simulations are quite accurate, but that the carrier transport simulations are not capturing all of the relevant processes. The low fill factor indicates that these processes are due to non-idealities such as series and/or shunt resistance and depletion region recombination. These processes could be incorporated into the model, but without significant experimental effort, the parameter values used to capture these processes would be fairly uneducated guesses. Therefore, these results demonstrate that this model can capture open circuit voltage accurately and, consequently, can serve as a predictive tool for which structures and operating conditions will have sufficient voltage to split water.

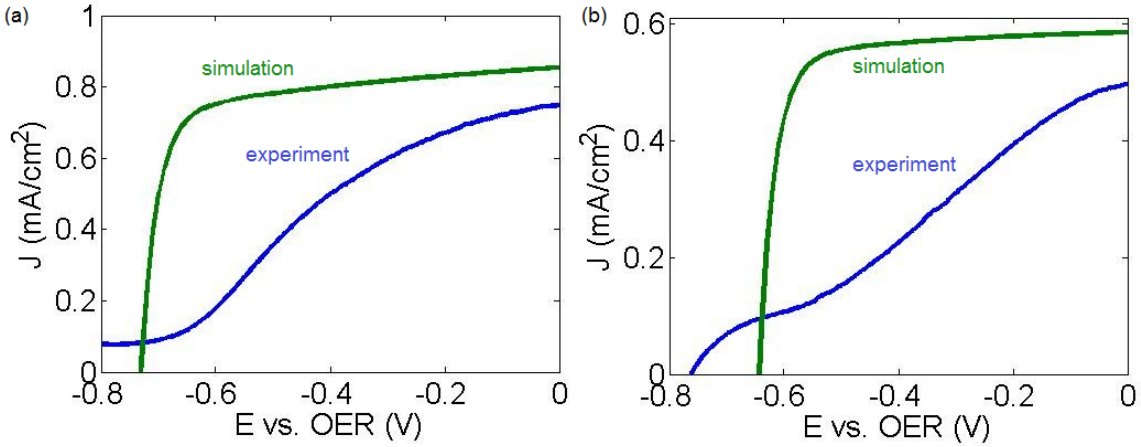


**Figure 20: Comparison of the *j-V* performance from experiment and simulation of a $WO_3$|liquid junction in (a) a planar configuration and (b) a microwire configuration.**

### 3.1.4 Comparison of Experimental and Theoretical Results for Tandem Planar and Microwire-Based Si|$WO_3$ Devices

This results in this section demonstrate the model's predictive ability for voltage, as discussed above, for the planar tandem structure at 1 sun and the microwire tandem structure at 1 sun and 11 suns. Figure 21 displays the experimentally-measured *j-V* curves for the tandem structures. Figure 21(a) displays the *j-V* curves for the planar (green) and microwire-based (blue) devices at 1 sun illumination, revealing that the planar device can split water but the microwire-based device does not have sufficient voltage to split water because it does not pass positive current at the $H^+|H_2$ redox potential (0 V). Figure 21(b) shows the microwire-based device at 1 (green) and 11 (blue) suns illumination, demonstrating that while the microwire-based design does not have sufficient voltage at 1 sun illumination, it is capable of driving water-splitting under concentrated 11 sun illumination. This photovoltage increase arises from the logarithmic dependence of voltage on photocurrent density, shown in the ideal diode equation, Equation (3).

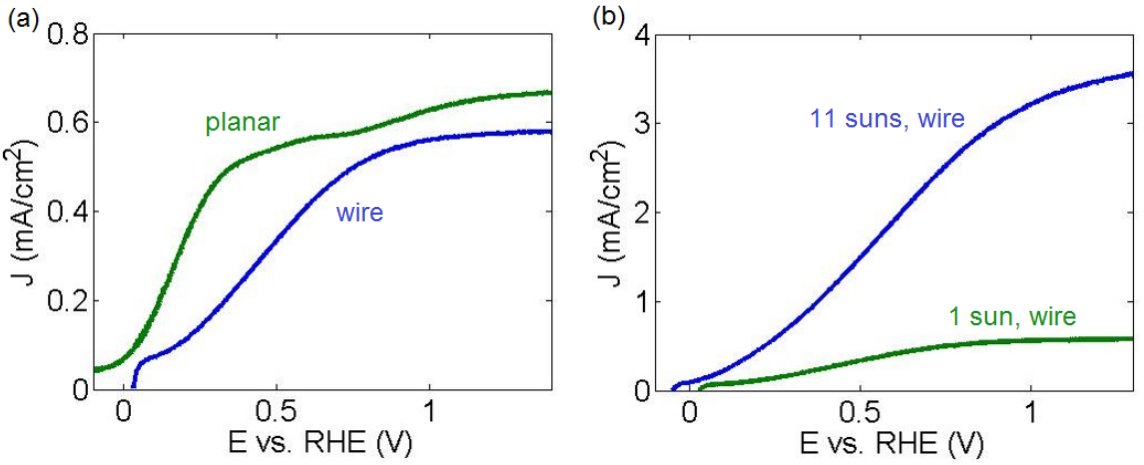


**Figure 21: *j-V* curves for the tandem Si|$WO_3$ devices under different conditions; (a) planar (green) and microwire (blue) structures under 1 sun illumination, (b) microwire structures under 1 (green) and 11 (blue) suns illumination.**

Figure 22 shows load line analyses of simulation data for the same structures and under the same conditions as the experimental data shown in Figure 21. In each plot, the green line is the *j-V* performance of the silicon p|n junction, the red line incorporates the Butler-Volmer kinetics of a platinum catalyst with the Si p|n junction, and the blue line is the *j-V* performance of the $WO_3$|liquid junction. The point at which the red and blue line cross is the predicted operating current density of the device. The first plot (a) represents the planar tandem device under 1 sun illumination, and the second (b) and third (c) plots represent the microwire-based device under 1 and 11 suns illumination, respectively. These results demonstrate that the model predicts the planar tandem under 1 sun and the microwire tandem under 11 suns to have sufficient voltage to split water, while the microwire tandem under just 1 sun illumination falls short of the water-splitting voltage. This simulation result agrees with the experimentally-observed results and demonstrates the predictive ability of the model.

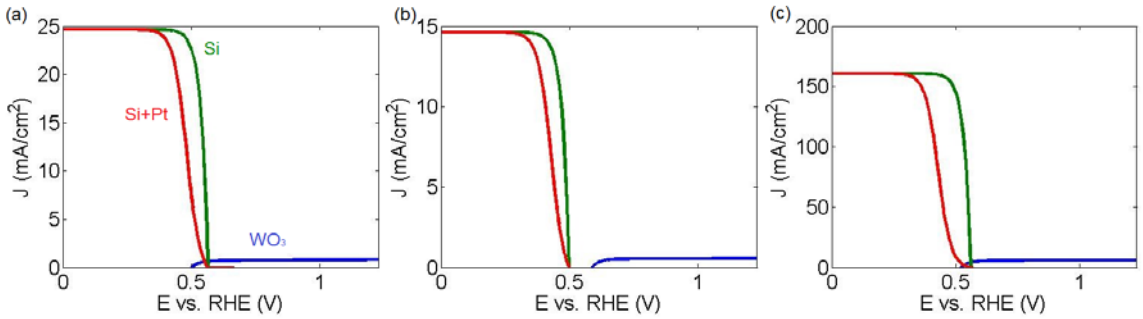


**Figure 22: Load-line analyses for the structures and conditions corresponding to experiments shown in Figure 21; green line is silicon, red is silicon with platinum catalysis, blue is $WO_3$; the operating point is where the red line crosses the blue line; (a) planar tandem under 1 sun, (b) microwire tandem under 1 sun, (c) microwire tandem under 11 suns.**

## 3.2 Optoelectronic Design of the Microwire-Based Si|$WO_3$ Device

This section addresses design optimization using the validated model. Two primary optoelectronic variations of microwire tandem absorbers (illustrated in Figure 23) are initially explored and design features that increase light absorption without compromising carrier collection are investigated. The main difference between the two variations is the optical opacity or transparency of the contact material interconnecting the two photoelectrodes. An opaque contact design increases the photon path length, and thus absorption, in the photoanode ($WO_3$), which is crucial for wide bandgap materials, while the transparent contact design reduces absorption losses in the contact layer. Opaque aluminum and transparent indium tin oxide (ITO) contacts are investigated because their electron affinities facilitate formation of an ohmic contact to $WO_3$.[13,39,40] The optical characteristics of these contact materials and of the Si photocathode and $WO_3$ photoanode motivates the different doping schemes shown. A buried p|n Si junction enables a larger open circuit voltage ($V_{OC}$) and more ideal behavior than the feasible alternative, i.e., a liquid junction between p-Si and the $H^+|H_2$ redox couple.[41] In both optoelectronic designs,

the solution interface consists of degenerately doped n-type Si to facilitate tunneling for nearly lossless charge transfer. Similarly, the contact interface with degenerately doped p-Si creates a tunneling ohmic contact. However it is desirable to position the p|n junction in close proximity to the areas of greatest light absorption, viz., the bottom half of the wire in the opaque contact design and the top half of the wire in the transparent contact design. Returning to the beginning of the chapter, Figure 16 shows an exemplary band diagram in the dark and under illumination for the structure in Figure 23(b) with the omission of the $n^+$-Si layer at the Si|liquid interface.

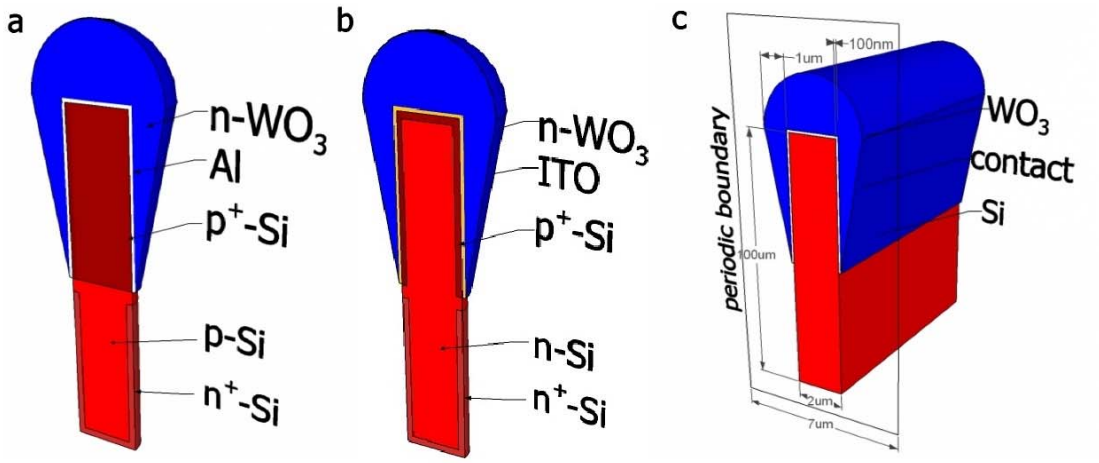


**Figure 23: Schematics for two proposed optoelectronic designs; (a) an opaque contact with the p|n junction in the bottom half of the Si microwire (b) a transparent contact design with the p|n junction in the top half of the Si microwire.**

### 3.2.1 Design-Specific Methods

The nominal design is a 7 μm period square lattice array consisting of 100 μm tall silicon microwires with 1 μm radii; the top 50 μm of the wires are conformally coated with 100 nm of either Al or ITO contact material and 1 μm of $WO_3$. The nominal photoanode geometry mimicked the shape of experimental $WO_3$ photoanodes (Figure 23). Material parameters and simulation

methods were identical to those used for model validation (Section 3.1.2). Charge carrier transport simulations were performed only for the $WO_3$|liquid junction because the $WO_3$ limits device performance. Solution of the coupled Poisson and charge carrier equations under illumination and no applied bias determined the short circuit, bulk recombination and surface recombination current densities for each structure. Absorbed current density, short circuit current density at normal incidence, and day-integrated hydrogen production per unit area are used as figures of merit for the designs considered. The absorbed current densities reported for the contact ($j_{Contact}$), reflection ($j_{Ref}$), and transmission ($j_{Trans}$) are integrated up to the band edge of silicon ($\lambda$=1100 nm).

### 3.2.2 Performance of the Original Microwire-Based Si|$WO_3$ Designs

Figure 24(a) and (b) exhibit plots of normal incidence absorption vs. wavelength for Si, $WO_3$, and the contact material in the two original designs (Figure 23) with comparison to a planar device with thicknesses corresponding to equal material volume ($w_{Si}$=6.4 µm, $w_{WO3}$=5 µm, $w_{ITO}$=0.7 µm). Solid lines represent the microwire-based designs and dashed lines represent the planar equivalent design. ITO was used as the contact material in these planar comparisons because aluminum ($w$=0.7 µm) would block all light from the silicon. Table 2 displays the normal incidence ideal short circuit current densities, ideal day-integrated hydrogen production densities, normal incidence internal quantum efficiencies, normal incidence short circuit current densities, and current density losses due to bulk and surface recombination for each design and its planar equivalent.

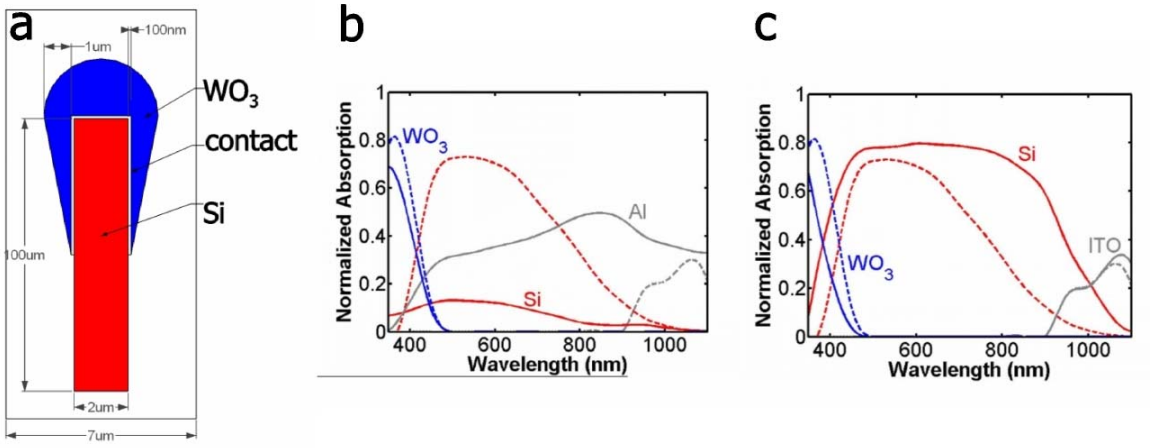


**Figure 24: (a) Schematic of simulation unit cell, simulated as a 2D infinite array using TE polarized illumination at normal incidence; (b) absorption vs. wavelength for the photoanode, photocathode, and contact for the structure in (a) with an opaque, aluminum contact; (c) absorption vs. wavelength for the photoanode, photocathode, and contact for the structure in (a) with a transparent, indium tin oxide (ITO) contact. Solid lines represent microwire-based designs and dashed lines are their planar equivalents.**

**Table 2: Ideal short circuit current densities ($mA \cdot cm^{-2}$), day-integrated hydrogen production ($mmol \cdot day^{-1} \cdot cm^{-2}$), internal quantum efficiencies and short circuit current densities ($mA \cdot cm^{-2}$) for the opaque and transparent contact models and their planar equivalence**

| Model | $j_{Si}$ | $j_{WO3}$ | $j_{Contact}$ | $j_{Ref}$ | $j_{Trans}$ | $F_{H2}$ | IQE | $j_{SC}$ | $j_{BR}$ | $j_{SR}$ |
|---|---|---|---|---|---|---|---|---|---|---|
| Opaque | 3.21 | 1.46 | 16.72 | 18.07 | 5.52 | 0.09 | 0.86 | 1.26 | 0.03 | 0.17 |
| Transparent | 28.31 | 1.02 | 2.11 | 5.69 | 7.86 | 0.17 | 0.88 | 0.90 | 0.02 | 0.20 |
| Planar | 16.53 | 1.75 | 0.20 | 16.19 | 8.86 | 0.26 | 0.57 | 1.00 | 0.54 | 0.21 |

The significantly lower absorbed current density of $WO_3$ in comparison to Si in all designs illustrates that $WO_3$, due to its wide bandgap, absorbs far less light than Si and limits device current density and hydrogen production in both cases. Because of aluminum's reflective properties, the opaque contact design outperforms the transparent contact design at normal incidence due to an increased photon path length and, hence, greater absorption in $WO_3$. However, the transparent contact design outperforms the opaque contact design in day-integrated hydrogen production because aluminum absorption in the opaque contact design increases and transmission in the transparent contact design decreases with increasing incidence angle. Absorption in the $WO_3$ is limited by contact absorption in the opaque contact design and silicon absorption in the transparent contact design, which has significant ramifications for light absorption optimization and is discussed later in this section.

Neither of the microstructured designs outperforms the equivalent planar device optically ($j_{WO3}$), mainly due to a longer, uninterrupted photon path length through the $WO_3$ in the planar case. However, when complete optoelectronic performance is taken into account ($j_{SC}$), the transparent model approaches and the opaque contact model outperforms the planar equivalent device at normal incidence. Both of the microstructured devices have higher internal quantum efficiencies than the planar device because they have shorter carrier diffusion pathways, thereby minimizing bulk recombination. In fact, the dominant loss in the microstructured designs is surface recombination at the ohmic contact rather than the bulk recombination which dominates losses in the planar case. The higher internal quantum efficiencies of the two microstructured devices underscore the advantage of orthogonalizing the directions of light absorption and carrier collection for materials like $WO_3$ (reported $L_D$=200 nm-1 um)[42,43,44] that have indirect optical bandgaps and relatively low material quality.

### 3.2.3 Surface Plasmon Polariton Modes in Microwire-Based Si|$WO_3$ Designs

In the opaque contact design, significant absorption losses result from contact absorption (16.72 $mA \cdot cm^{-2}$), reflection (18.07 $mA \cdot cm^{-2}$) and transmission (5.52 $mA \cdot cm^{-2}$). While an appropriate antireflective (AR) coating, a back reflector, and smaller pitch size can minimize reflection and transmission losses, the losses to parasitic contact absorption, 0.78 $mA \cdot cm^{-2}$ of which lie within the $WO_3$ band edge, present a more complex optimization problem. Experimental measurements of optically-thick planar aluminum indicate 93% reflection and 7% absorption; therefore, a simple ray optics framework cannot explain the absorption results for aluminum in the microwire structure. Observation of the electric field propagation in time reveals that light couples strongly into a lossy surface plasmon-polariton (SPP) mode at the $WO_3$|aluminum interface. For ease of visual demonstration, Figure 5 displays snapshots of the SPP mode propagating at 200 and 800 nm wavelengths along an aluminum|air interface, eliminating any convolution with the complex structure geometry and the absorption constant of $WO_3$. At $\lambda$=800 nm (Figure 25a), the evanescent decay of the electric field away from the interface, a signature of an SPP mode,[45] is readily evident. At $\lambda$=200 nm (Figure 25b), as the wavelength of light approaches the Al|air SPP resonance of 113 nm (see Appendix A.1), the decay length decreases and the speed of light that is trapped in the SPP mode slows notably in comparison to the plane wave, another signature of an SPP mode.[45] The surface wave disappears at wavelengths shorter than the resonant wavelength. The $WO_3$|Al interface within the complete microstructure exhibits similar behavior.

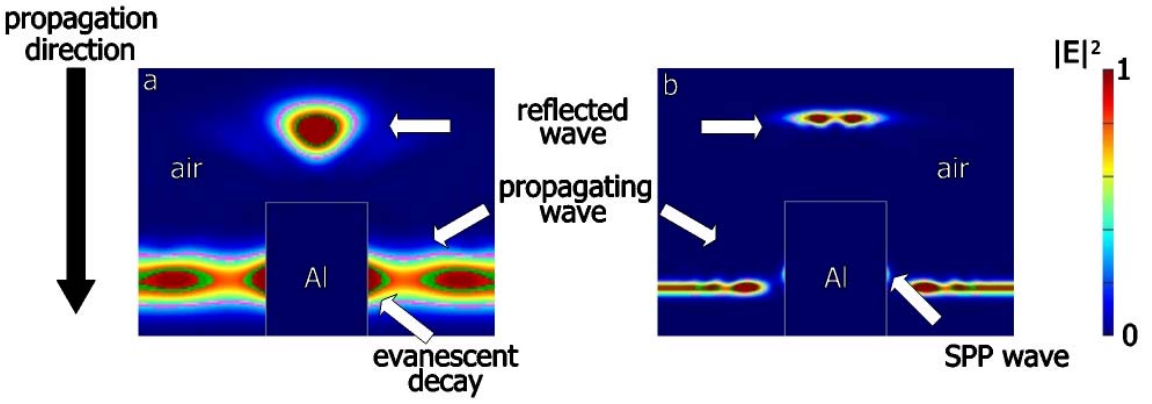


**Figure 25: Snapshots of the propagation of the electric field along an aluminum|air interface within an infinite 2D array of wires indicating the coupling into a surface plasmon-polariton mode (a) at $\lambda$=800 nm, illustrating the evanescent decay of the electric field away from the interface; (b) at $\lambda$=200 nm, illustrating the slower propagation of light at the interface.**

Given that the lossy SPP mode at the $WO_3$|Al interface is the source of parasitic absorption in the aluminum, optimization of the opaque contact structure requires eliminating or, at a minimum, greatly reducing the amount of light that couples into this mode. A plethora of approaches were explored including reduction of aluminum, both in coverage area and thickness, alteration of the shape of the $WO_3$ and the Al, and replacement of Al with Ag (silver). Detailed results for these structures can be found in Appendix A.2. None of these approaches eliminate coupling into the SPP mode; this robust coupling capability of the microwire structure is attributed to the scattering properties of the wires. The most successful approach was the replacement of Al with Ag, resulting in a ~40% reduction in the contact absorption (see Appendix A.2 for details). Silver's red-shifted plasmon resonance and lower absorption coefficient throughout the visible in comparison to aluminum contribute to its lower absorption. Nevertheless, the Ag absorption loss (9.68 $mA \cdot cm^{-2}$) is large and places an inherent limit on the overall device performance. Despite the seemingly promising initial performance of the opaque contact design, these results motivate a

more detailed analysis and optimization of the transparent contact design due to its greater potential for light absorption optimization.

### 3.2.4 Optimization of Microwire-Based Si|$WO_3$ Designs

In the transparent contact design, the contact absorption is insignificant in the UV-Vis region and minimal in the infrared region. Silicon absorbs over an order of magnitude more light than $WO_3$; thus, the following optimization focuses solely on improving $WO_3$ optoelectronic performance, even at the expense of silicon absorption. As previously mentioned, the main sources of absorption loss for $WO_3$ within its band edge are from reflection, transmission and absorption in the silicon. Increasing the $WO_3$ thickness is the simplest approach to increase its absorption, but this method is constrained by the electronic performance of the material. Based on preliminary experimental measurements, the diffusion length of $WO_3$ is ~1 μm,[42] which suggests that increasing the thickness of $WO_3$ beyond its current 1 μm thick coverage would have diminishing returns. Thus, other alterations to the original design are made iteratively in order to find an optimized structure for light absorption that has comparable electrical performance with the original design. The most logical alterations include the reduction of the array pitch (7 μm to 5 μm for the optimized structure) to increase the amount of light that first interacts with the $WO_3$, the addition of an antireflective (AR) coating (100 nm of $SiO_2$ coating the upward-facing portion of the $WO_3$|air interface) to reduce reflection, and the addition of a back reflector (smooth metal surface) to eliminate transmission. Another alteration towards improving $WO_3$ absorption is the flattening of the top of the $WO_3$ in order to (i) reduce reflection at the $WO_3$|air interface and (ii) decrease silicon absorption within the $WO_3$ band edge by directing light downwards into the $WO_3$ as opposed to focusing light towards the silicon wire with the rounded top. The shape of the top

half of the silicon wire is etched into a cone shape in order to promote scattering back into the $WO_3$ at the ITO|$WO_3$ interface.

Figure 26 and Table 3 show schematics, absorption characteristics, and optoelectronic performance metrics for the original transparent model, a partially optimized structure, and the optimized structure (solid lines) along with their planar equivalent thickness structures (dashed lines). The partially-optimized structure includes the conically-shaped silicon and an AR coating; its planar equivalent ($w_{Si}$=4.3 μm, $w_{WO3}$=7.6 μm, $w_{ITO}$=0.2 μm) also includes an AR coating. The optimized structure includes all modifications discussed above; its planar equivalent ($w_{Si}$=8.4 μm, $w_{WO3}$=14.6 μm, $w_{ITO}$=0.4 μm) includes an AR coating and back reflector. Additional steps in the iterative optimization process, including design and absorption results, can be found in Appendix A.3. At normal incidence, the $WO_3$ in the optimized structure absorbs 230% more light and collects 240% more current density than in the original transparent contact model and 130% more light and 140% more current density than the opaque contact model. Despite an increase in bulk recombination due to the addition of oxide material per structure as well as per aerial area, the internal quantum efficiency of the optimized design is also slightly higher than that of the original because a smaller fraction of the minority carriers are recombining at the ohmic contact. The absorption enhancements of the optimized design extend over all angles of incidence, resulting in a 140% increase in hydrogen production over the original transparent contact model and a striking 350% increase over the opaque contact model. Additionally, the optimized model outperforms its planar equivalent device in both optical and optoelectronic efficiency, highlighting the advantages of light guiding and scattering properties of the optimized microstructured devices.

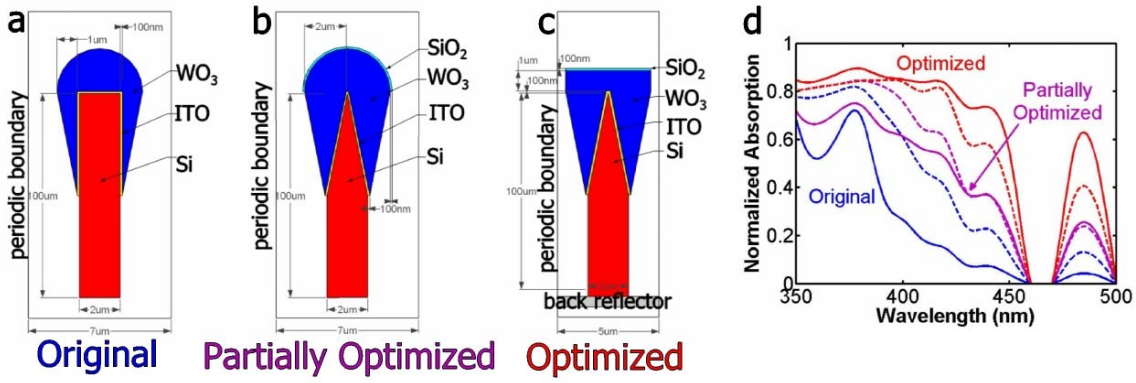


**Figure 26: Schematic of (a) the original, (b) the partially optimized, and (c) the optimized microwire array designs with the transparent, indium tin oxide contact; (d) plot of $WO_3$ absorption vs. wavelength, demonstrating the absorption enhancement, where solid lines are the microwire-based designs and dashed lines are their planar equivalents.**

**Table 3: Ideal short circuit current densities ($mA \cdot cm^{-2}$), day-integrated hydrogen production ($mmol \cdot day^{-1} \cdot cm^{-2}$), internal quantum efficiencies and short circuit current densities ($mA \cdot cm^{-2}$) for the original, partially-optimized and optimized transparent contact designs and their planar equivalences.**

| Model | $j_{Si}$ | $j_{WO3}$ | $j_{Contact}$ | $j_{Ref}$ | $j_{Trans}$ | $F_{H2}$ | IQE | $j_{SC}$ | $j_{BR}$ | $j_{SR}$ |
|---|---|---|---|---|---|---|---|---|---|---|
| Original | 28.31 | 1.02 | 2.11 | 5.69 | 7.86 | 0.17 | 0.88 | 0.90 | 0.02 | 0.20 |
| Planar | 16.53 | 1.75 | 0.20 | 16.19 | 8.86 | 0.26 | 0.57 | 1.00 | 0.54 | 0.21 |
| Partial Opt. | 28.10 | 2.10 | 5.12 | 1.04 | 8.70 | 0.34 | 0.85 | 1.79 | 0.11 | 0.20 |
| Planar | 14.79 | 2.03 | 0.58 | 16.57 | 9.59 | -- | 0.49 | 1.00 | 0.88 | 0.15 |
| Optimized | 33.50 | 3.39 | 6.06 | 2.09 | 0.00 | 0.40 | 0.90 | 3.05 | 0.12 | 0.22 |
| Planar | 17.31 | 2.43 | 1.46 | 14.55 | 7.83 | -- | 0.41 | 0.99 | 1.39 | 0.05 |

### 3.2.5 Conclusions from the Microwire-Based Si|$WO_3$ Designs

This coupled electromagnetic simulation/carrier transport investigation of the optoelectronic performance of tandem Si|$WO_3$ microwire arrays reveals that geometric design and the contact material selection can significantly influence light absorption properties. Furthermore, opaque contacts are not a realistic choice for the interface between the two semiconductors because they absorb a substantial amount of light, thereby reducing the overall device efficiency. Also, antireflective coatings, back reflectors and reduction of array period are powerful handles for increasing efficiency. While the Si|$WO_3$ system is not an ideal material combination for tandem devices due to the excessively wide bandgap of $WO_3$, the optoelectronic results from this system are instructive for any system where the photoanode current density is limiting.

Additionally, this study reveals the value of full wave electromagnetic simulations coupled to charge carrier transport simulations for mesoscale design of photoelectrochemical devices. Simulation tools can quantitatively predict optoelectronic performance for realistic geometries and identify absorption-limiting phenomena, such as the lossy SPP mode in the opaque contact design, more quickly and efficiently than via a large number of experiments. These observations would be difficult, if not impossible, to make experimentally. Device models were developed and optoelectronic performance analyzed for roughly 50 design variations over the span of approximately six months, demonstrating the speed at which model-based device optimization can occur.

# Chapter IV: Optical Design of Nanowire-Based Photovoltaic and Photoelectrochemical Devices

In recent years, photonic phenomena in semiconductor nanowires have been the subject of great interest and intensive research effort, motivated by fundamental interest owing to their remarkable optical properties, including reduced reflectance,[46,47,48] increased absorption,[49,50,51,52] and spectral selectivity,[53,54,55] and are also of considerable interest in applications to optoelectronic and photovoltaic devices. For next generation photovoltaics and advanced photoelectrochemical devices, arrays of semiconducting nanowires present an opportunity to reduce material usage and cost, while maintaining or improving optoelectronic performance relative to thin film or bulk materials. In particular nanowires can exhibit light trapping features not seen in thin films and also have the potential to orthogonalize the directions of light absorption and carrier collection, which enhances carrier collection in materials with short carrier diffusion lengths.[21,23,24,56,57,58] Nanowire arrays with a wide range of materials, wire diameters and array densities have been investigated experimentally and theoretically. High fidelity arrays of III-V nanowires with varying geometry can be fabricated via molecular beam epitaxy (MBE)[59] or metalorganic chemical vapor deposition (MOCVD), using either the selective-area growth (SAG, catalyst-free)[60,61] or vapor-liquid-solid (VLS, typically Au catalyst) methods.[62] The array pitch and wire diameter are easily tunable due to the use of patterned masks, created by electron-beam lithography[60] or nanoimprint lithography.[62] Reported light trapping mechanisms include coupling into photonic crystal modes,[49,63,64,65,66] coupling into leaky radial waveguide modes,[53,24,57,67,68,69] and absorption in media considered using effective index models.[70,71]

The subject of this chapter is the light absorption properties of individual and sparse arrays of semiconductor nanowires. The main focus is on III-V nanowires, but silicon nanowires are also studied. The chapter starts out with some initial experimental results on the optical and optoelectronic properties of sparse GaAs nanowire arrays. These initial results are used to develop an accurate model. Subsequently, an in-depth understanding of the mechanism for light absorption enhancement in sparse nanowire arrays is developed and then employed to optimize light absorption in sparse nanowire arrays via geometric and morphological optimization. Finally, the chapter concludes with some initial efforts towards experimental fabrication and characterization of optimized array geometries.

## 4.1 Fabrication, Characterization and Simulation of Sparse GaAs Nanowire Arrays

Again, the development of an accurate model with predictive capabilities begins with matching simulation results to experiment. In this case, the test system is sparse arrays of GaAs nanowires. This chapter begins with the fabrication procedure, optical and optoelectronic characterization of the GaAs nanowire arrays. Second, the experimental results are matched to optical simulation results to validate the model. Finally, simulation results identify the mechanism responsible for the observed absorption enhancements.

### 4.1.1 Fabrication and Characterization of GaAs Nanowire Arrays

This section summarizes the experimental fabrication and characterization of GaAs nanowire arrays, which were conducted by Dr. Shu Hu.

#### *4.1.1.1 Fabrication*

The sparse arrays of GaAs nanowires were grown via selective-area metalorganic vapor deposition; this method and other MOCVD-based nanowire growth methods are discussed in more detail in Section 4.4.1. Fabrication began with the creation of a growth mask on top of either GaAs <111>B or Si <111> substrates by depositing a thin, approximately 30 nm layer of $SiN_x$ via plasma-enhanced chemical vapor deposition (PECVD), writing the desired pattern via electron beam (e-beam) lithography, and etching the pattern into the nitride layer using a pseudo-Bosch etch. Figure 27(e) displays a simplified version of the overall process. Figure 27(a) illustrates the gas flow and temperature profiles as a function of time for growth of n-GaAs nanowires on an $n^+$-Si substrate. Initially, the patterned Si substrate was annealed at 965 ˚C for 5 min in $H_{2(g)}$ to remove residual silicon oxide in the openings of the mask. The Si substrate was then annealed at 440˚C for 2 min in $AsH_3$, to create an As-passivated Si surface, which resembled a GaAs <111>B surface and was crucial to attaining high-fidelity growth. A low-temperature nucleation step at 440 ˚C for 8 min in the presence of trimethylgallium (TMGa) and arsine ($As_2H_6$) was then followed by a high-temperature step for nanowire growth at 790˚C for 30−60 min with disliane ($Si_2H_6$) as the n-dopant source. Figure 27(b) illustrates the gas flow and temperature profiles as a function of time for the growth of GaAs nanowires on an $n^+$-GaAs <111>B substrate (Si doped, doping concentration $3\times10^{18}$ $cm^{-3}$). High-temperature annealing and low-temperature nucleation steps were not necessary in this process flow to produce GaAs nanowires. Figure 27(c) displays a typical SEM image of arrays of GaAs nanowires that were grown on a Si substrate, with this image also representative of arrays of GaAs nanowires that were grown on a GaAs substrate. The measured diameter of the GaAs nanowires on Si or GaAs substrates was approximately 135 nm, and the pitch was 600 nm. The GaAs nanowires on Si substrates were 2.5 μm long from a 30 min growth, and the GaAs nanowires on GaAs substrates were 3 μm long from a 1 h growth. Longer growth

times did not significantly improve the optical absorption of the resulting nanowire arrays. The resulting dimensions correspond to 4% fill fraction arrays. High-resolution transmission-electron microscopy, Figure 27(d), indicates that the GaAs nanowires had a zincblende crystal structure, with a high density of twin defects along the <111>B growth direction.

To measure the optical properties of the nanowire arrays without substrate contribution, the nanowire arrays were embedded in poly-dimethyl-siloxane (PDMS) and peeled off from the substrate. The PDMS was prepared at a 5:1 ratio of base to curing agent and was subsequently spin-coated onto the wire arrays at 1000 rpm for 1 min. The embedded arrays were degassed for 30 min, cured overnight at 80°C, and then mechanically removed from the substrate with tweezers.

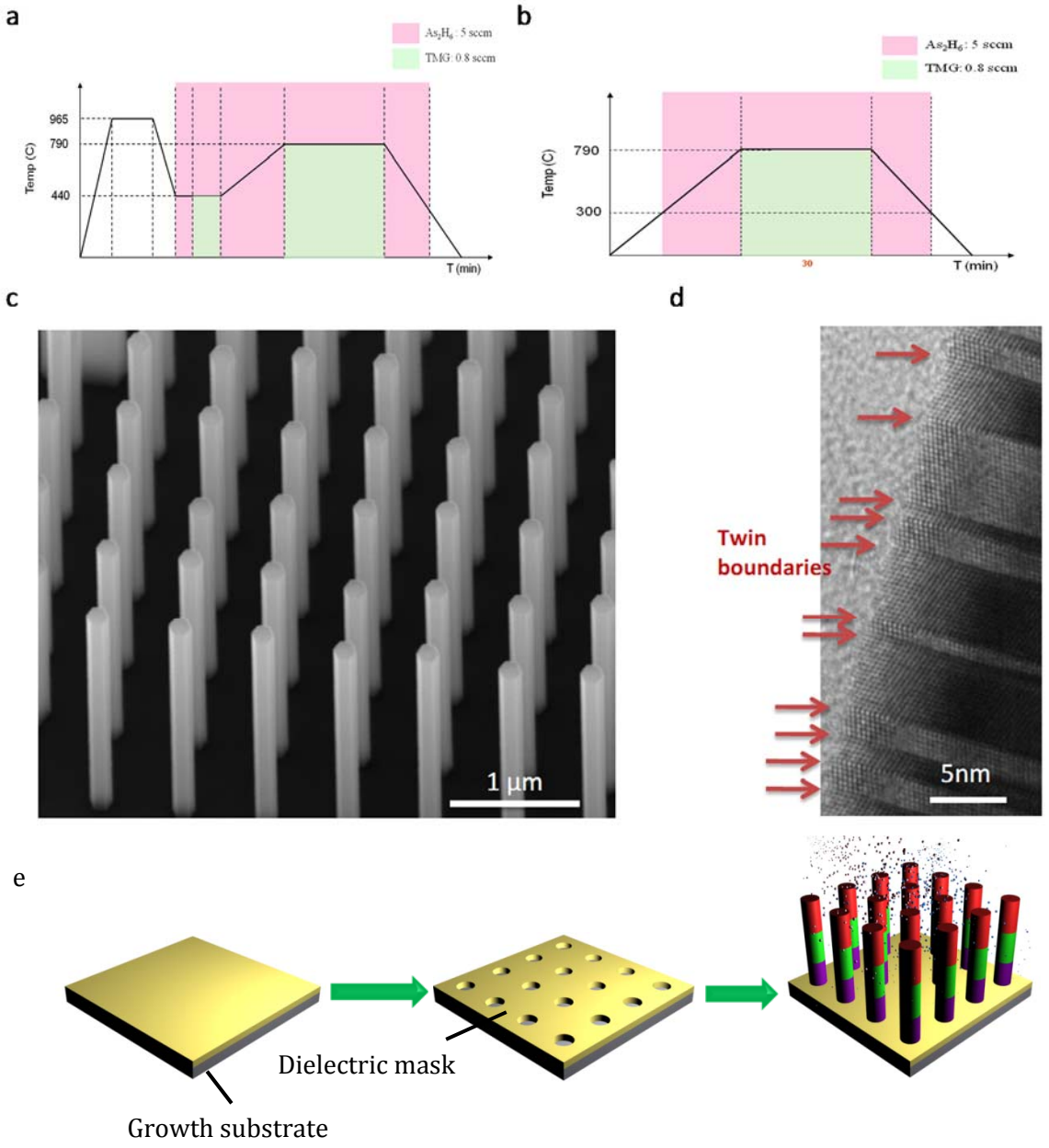


**Figure 27: MOCVD growth process for GaAs nanowire arrays on (a) silicon and (b) GaAs substrates; (c) SEM image of as-grown nanowire arrays at 30°tilt; (d) TEM of a single GaAs nanowire, with red arrows indicating twin boundaries; (e) process flow for GaAs nanowire arrays fabrication.**

#### *4.1.1.2 Optical Characterization*

Wavelength- and angle-dependent absorption spectra of the arrays were obtained using a UV-Vis spectrometer (Varian Cary 5000) that was equipped with an integrating sphere. A small-spot kit was used to produce a beam size of less than 1 mm (FWHM) for focused illumination. The divergence angle of the incident beam was 9˚. The internal surfaces of the sphere, baffles, port blocks and port apertures were coated with a barium sulfate coating to achieve nearly ideal Lambertian reflectivity. In a center-mount mode for absorption measurements of non-opaque samples (e.g. GaAs nanowire arrays embedded in peeled-off PDMS), each sample was supported on a quartz slide that was placed at the center of the sphere. In a rear-mount mode for reflection measurements of opaque samples (e.g. as-grown GaAs nanowire arrays on GaAs or Si substrates, GaAs nanowire arrays embedded in PDMS placed on a Ag back reflector), each sample was mounted behind a 2 mm-diameter port aperture at the rear port of the sphere, with light at normal incidence.

Figure 28 in the next section (Section 4.1.3) shows the optical absorption results alongside the corresponding simulation results. By comparison to bulk or planar thin films, the nanowire arrays exhibited enhanced optical absorption across the UV-Vis-NIR portion of the solar spectrum, via scattering events and light trapping effects that minimized reflection losses. The optical absorption properties of the nanowire arrays are highly wavelength-dependent and approach near-unity absorption at certain wavelengths. A ray optics picture is not sufficient to explain this phenomenon in 4% fill fraction arrays, which correspond to a 125 nm thick planar equivalent layer for the 3 μm tall GaAs nanowire arrays; it is this result that drove the detailed theoretical study and simulation-based optimization that is discussed in Section 4.2.

### *4.1.1.3 Optoelectronic Characterization*

The first step in converting a GaAs nanowire array on substrate into an electrode is sequential evaporation of metal films on the backside of the array to create an electrical contact; this metal sequence is a 100 nm Au-Ge eutectic alloys (12%-wt Ge) |30 nm nickel | 100 nm gold layered stack, which is rapidly thermally annealed in forming gas (4% $H_2$ in $N_2$) at 400 °C for 1 min. The array was then attached to a coiled, Sn-plated Cu wire using conductive Ag paint, and epoxy (Hysol 9460F) was used to seal the assembly face-down at the end of a segment of glass tubing. The active area of each electrode was defined by the epoxy, with a typical value of 0.009 $cm^2$. Only the GaAs nanowire array was exposed to the electrolyte, while the remaining area of the substrate was covered by sputtered $SiN_x$ and then by epoxy.

Prior to photoelectrochemical measurements, the n-GaAs nanowire array and planar n-GaAs photoelectrodes were etched in a solution of 0.04% (v/v) $Br_2$ in methanol ($CH_3OH$, low water, J.T.Baker) for 15 s, followed by immersion in 1.0 M KOH(*aq*) for 15 s. The KOH solution was then replaced with 2.0 M $NH_3$ in $CH_3OH$, after which the electrode was dried in a flow of $N_2$(g) and quickly transferred into a glove box that was continually purged with ultra-high purity (UHP) argon.

For the non-aqueous PEC experiments, acetonitrile ($CH_3CN$, anhydrous, 99.8%, Sigma Aldrich) was dried by flowing through a solvent column and storing the solvent over 3Å activated, molecular sieves. $LiClO_4$ (battery grade, 99.99%, Sigma Aldrich) was dried by fusing the salt under $<1\times10^{-3}$ Torr at 300 °C, and the resulting material was stored under UHP Ar (g) that contained <0.2 ppm $O_2$(g). Bis(cyclopentadienyl) iron(II) (ferrocene, $FeCp_2^0$) was purchased from Sigma Aldrich and was purified by sublimation in vacuum. Bis(cyclopentadienyl) iron(III) terafluroborate

(ferrocenium, $FeCp_2^+ \cdot BF_4^-$) was purchased from Sigma Aldrich, recrystallized in a mixture of diethyl ether and acetonitrile, and dried in vacuum before use.

A standard three-electrode potentiostatic setup, with ferrocenium|ferrocene ($FeCp_2^+|FeCp_2^0$) as the redox couple and dry acetonitrile ($CH_3CN$) as the solvent, was used for all of the photoelectrochemical experiments. The reference electrode was a Pt wire poised at the solution potential, and the counter electrode was a Pt mesh with an area more than 10 times larger than the working electrode. The working photoelectrodes were oriented vertically downward and were illuminated by an ELH-type tungsten-halogen bulb that was adjusted in intensity using neutral density filters. To obtain the photoelectrochemical data, all three electrodes were immersed in a dry $CH_3CN$ solution that contained 0.5 mM ferrocenium, 90 mM ferrocene, and 1M $LiClO_4$ as the supporting electrolyte. The solution was vigorously stirred to minimize mass transport effects on the current density.

The enhanced optical absorption of GaAs nanowire arrays, in conjunction with radial carrier-collection, resulted in high external quantum yields (EQYs) when these GaAs nanowire arrays were used as energy-conversion devices. To investigate the carrier-collection efficiency of GaAs nanowire arrays, the EQY ($\Phi_{ext}$) vs. wavelength was measured at normal incidence by forming a semiconductor|liquid junction between the as-grown, n-GaAs nanowire array and the ferrocenium|ferrocene redox couple ($FeCp_2^{+/0}$) in dry acetonitrile ($CH_3CN$) that contained lithium perchlorate as the supporting electrolyte. This method revealed the fundamental properties of the as-grown, three-dimensional GaAs nanowire arrays without the need for additional process steps to create metallurgical junctions and conformal solid-state contacts. The fast, reversible redox system was chosen to ensure that the electron-transfer kinetics at the

semiconductor|liquid interface were not rate-limiting.[72,73,74] A rectifying junction was formed surrounding each of the nanowires, facilitating radial separation of light-generated carriers.

In the next section (Section 4.1.3), Figure 29 shows the external quantum yield results from the non-aqueous photoelectrochemistry measurements alongside the corresponding simulation results. Similar to the absorption results, near-unity external quantum yields are observed, indicating near unity carrier collection efficiencies. This result indicates that the nanowires have sufficiently high electronic quality that carrier transport modeling of this system is unnecessary, and only optical simulations are necessary to evaluate nanowire efficiency potential.

### 4.1.2 Simulation of GaAs Nanowire Arrays

Optical simulations were conducted in Lumerical FDTD, using methods described in Chapter 2. For the GaAs nanowires grown on GaAs substrates, the nanowires were rendered in the software with lengths of 3.24 μm, diameters of 135 nm, and inter-wire spacings of 600 nm. The GaAs nanowires grown on silicon were identical, with lengths modified to 2.5 μm. These dimensions were used to most closely match the fabricated arrays. As justified in the previous section, no carrier transport simulations were done because optoelectronic characterization indicated near unity quantum yield.

### 4.1.3 Comparison of Experiment and Simulation of GaAs Nanowire Arrays

Figure 28 displays both the experimental (a and b) and simulation (c and d) results for light absorption in the GaAs nanowire arrays grown on GaAs substrates under different conditions. Specifically, Figure 28 a and c shows the normal incidence absorption spectra for the GaAs nanowire arrays on substrate (black), peeled off and mounted on a quartz substrate (green), and peeled off with a silver back reflector. The nanowires on substrate spectrum reveals that the nanowires have very low reflection. The green and blue spectra represent one and two pass

absorption, respectively. The nanowire arrays exhibit remarkably high absorption given that their fill fraction is only 4%. Additionally, Figure 28 (c) includes a simulated spectrum for the planar equivalent GaAs layer with a double layer antireflective coating, consisting of 100 nm of $TiO_2$ and $SiO_2$ (pink). A comparison of the planar spectrum to the nanowire spectra underscores the absorption enhancements observed in the nanowire arrays. Figure 28 (b) and (d) show the angle-dependent absorption spectra for the peeled-off nanowire arrays. These results demonstrate that the nanowire arrays exhibit high absorption and low reflection at all angles.

The simulation and experimental results show similar trends in all cases. In general, the spectral features are sharper in the simulated results than the experimental results. Potential sources for this peak broadening effect include a narrow distribution of wire diameters due to processing variations, deviations from completely vertically-aligned nanowires due to disturbances in the peel-off procedure, and the beam divergence caused by the focusing optic in the integrating sphere measurements.

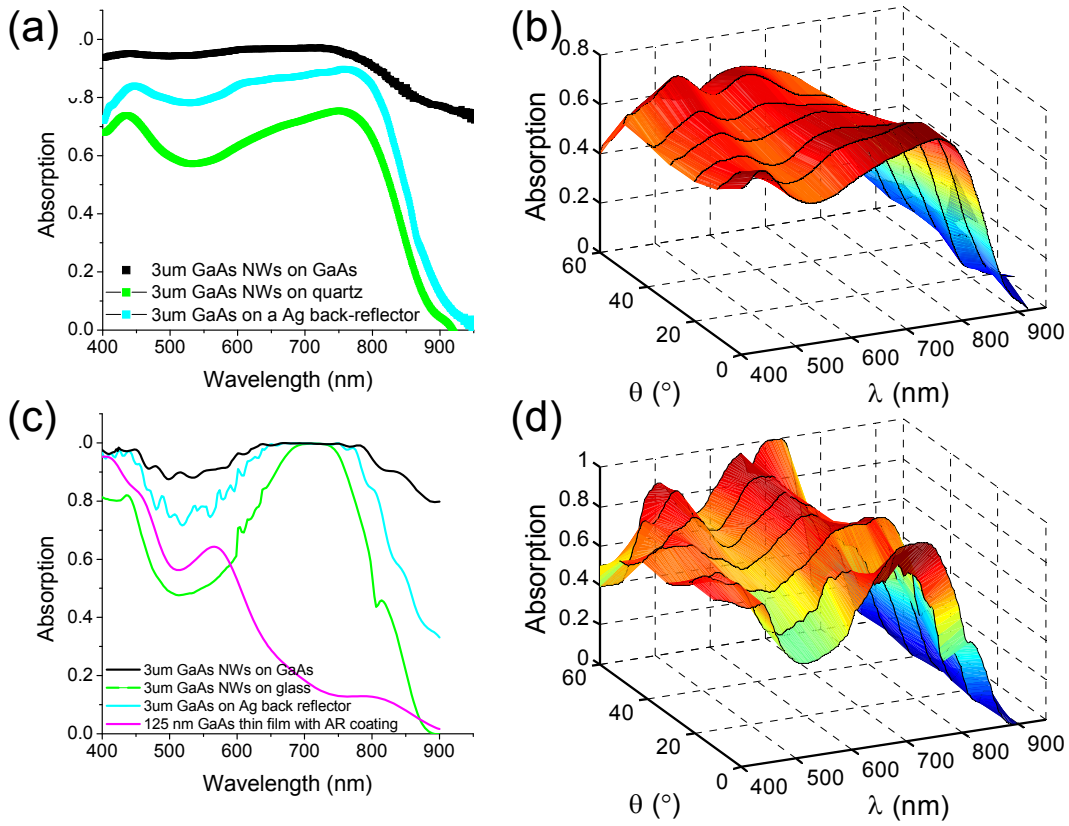


**Figure 28: Experimental (a,b) and simulated (c,d) optical absorption of GaAs nanowire arrays; (a,c) normal incidence for GaAs nanowires grown on GaAs (black), GaAs nanowires on quartz (green), GaAs nanowires on silver, and planar equivalent GaAs layer (125 nm) with double layer AR coating; (b,d) angle-dependent absorption of GaAs nanowires on quartz**

Figure 29 overlays the raw data and the solution-corrected data of the external quantum yields (EQY) of GaAs nanowire arrays on a GaAs substrate (a) and a Si substrate (b) in contact with $CH_3CN\text{-}FeCp_2^{+/0}$, with the simulated absorption in the GaAs nanowire arrays. The solution-corrected data accounts for absorption by the solution in the UV. The external quantum yield data is useful for comparison to the light absorption because (i) the EQY data is taken on the nanowire arrays prior to peel off, when the array fidelity is still high, (ii) the EQY data represents the

response of only the nanowires, not of the underlying substrate, and (iii) the internal quantum yield is near unity, indicating that the external quantum yields are a measure of absorption in the nanowires. An examination of Figure 29 reveals a much closer quantitative match between experiment and simulation. These results indicate that the developed model is accurate and has predictive power.

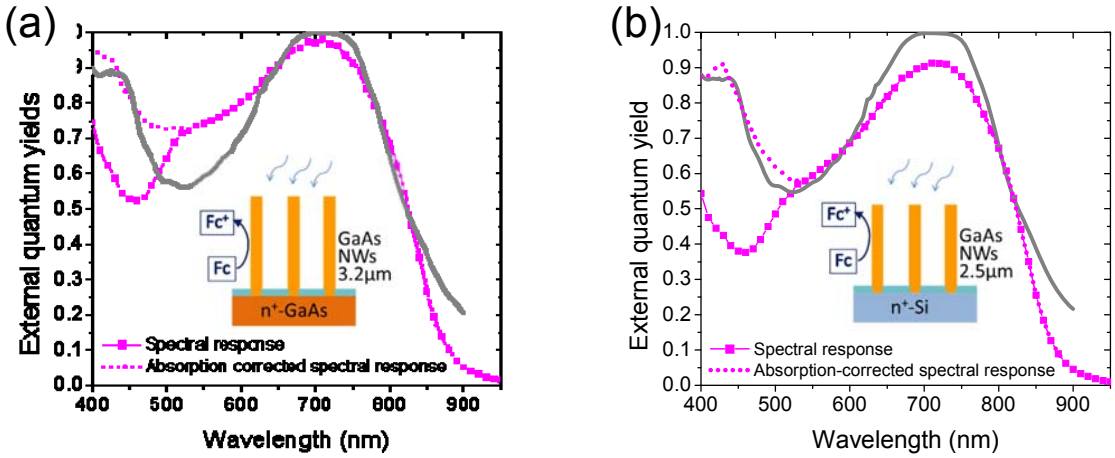


**Figure 29: Experimentally measured external quantum yields, raw data and solution-corrected (pink) overlaid with simulated optical absorption in GaAs nanowire arrays (grey) on (a) a GaAs substrate and (b) a Si substrate.**

Following its validation, the model is used to understand the strong, yet spectrally-dependent absorption in the nanowire arrays. The strong absorption in nanowire arrays can be attributed to optical waveguide modes, photonic crystal modes, and longitudinal modes, depending on the array characteristics. The bimodal behavior observed in these spectra immediately rules out longitudinal modes. Longitudinal modes depend on wire length, and within the analyzed spectral range of 400–900 nm, only modes of 20$^{th}$ order or greater exist in these arrays (L ≈ 3 µm), indicating that the modes would be spaced very close together spectrally. To examine whether

the nanowire arrays are resonantly absorbing into photonic crystal modes or waveguide modes, the absorption spectra dependence on nanowire radii and array pitch was simulated and analyzed. The spectral positions of both types of modes depend on nanowire radius, but only photonic crystal modes have a dependence on the periodicity of the array. The results of these simulations, displayed in Figure 30, reveal that the spectral peaks dramatically red-shift with increasing nanowire radius, whereas the arrays with varying pitch show no shift in peak position, but only an increase in off-resonance absorption with decreasing pitch due to the increase in fill factor. Therefore, these observations indicate that strong coupling into leaky waveguide modes is responsible for the absorption enhancements in sparse GaAs nanowire arrays. Additionally, the solutions to the eigenvalue equation for the leaky waveguide $HE_{11}$ and $HE_{12}$ modes in dielectric cylinders correspond spectrally with the peak positions observed experimentally and in simulation. The next section covers the details of leaky waveguide theory and its application to nanowire arrays in more detail and in the context of silicon.

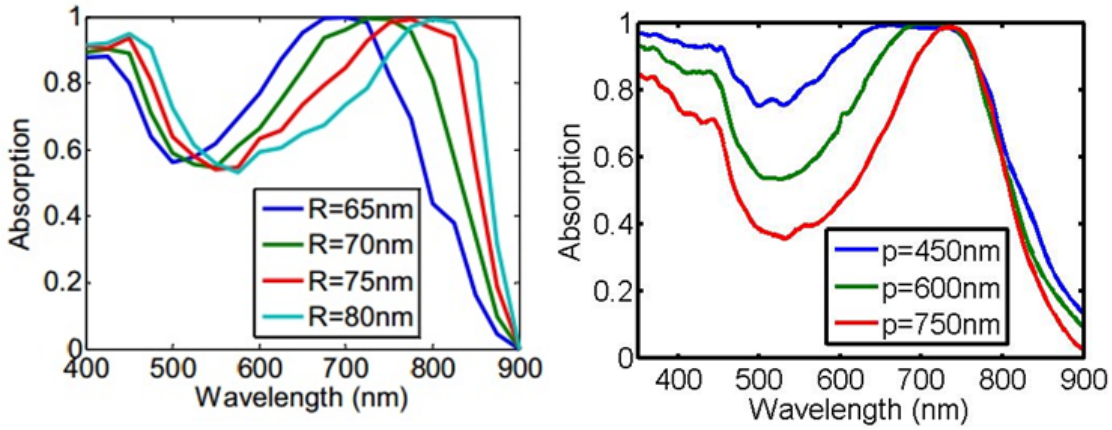


**Figure 30: Simulated absorption spectra of GaAs nanowire arrays for (a) varying nanowire radius and (b) varying array pitch.**

## 4.2 Theoretical Study of Light Absorption in Nanowires

This section presents a unified framework for resonant absorption in periodic arrays of high index semiconductor nanowires that combines a leaky waveguide theory perspective and that of photonic crystals supporting Bloch modes, as array density transitions from sparse to dense. Full dispersion relations are calculated for each leaky waveguide mode at varying illumination angles using the eigenvalue equation for leaky waveguide modes of an infinite dielectric cylinder. The dispersion relations, along with symmetry arguments, explain the selectivity of mode excitation and spectral red-shifting of absorption for illumination parallel to the nanowire axis in comparison to perpendicular illumination. Analysis of photonic crystal band dispersion for varying array density illustrates that the modes responsible for resonant nanowire absorption emerge from the leaky waveguide modes. The following analysis is performed on silicon nanowires ($r$=75 nm, $L$=2 μm). The lower absorption arising from the indirect bandgap of silicon facilitates easier distinction between modes closely spaced in frequency in comparison to the direct gap GaAs studied in the previous section, but the conclusions are relevant for any high aspect ratio semiconductor nanowires, including direct bandgap materials.

### 4.2.1 Study Specific Methods

For simulations with illumination perpendicular to the nanowire axis, 2D simulations were used and the nanowires were modeled as infinitely long cylinders. Single wavelength simulations were carried out for wavelengths between 400 and 900 nm, every 5 nm. Absorption efficiencies for individual nanowires were calculated by normalizing absorption to the geometric cross section of the nanowire.

Will Whitney performed the photonic crystal calculations discussed within this section, using 2D simulations with Bloch boundary conditions to simulate infinite periodic arrays of nanowire

structures in two dimensions. The band structure was calculated by determining the resonant frequencies present at each point in a parameter sweep of the photonic crystal wavevector, *k*. At each *k*-point, an individual, broadband simulation was performed for 0 to 750 THz. The mode excitation source was randomly-positioned and randomly-oriented dipoles with TM polarization were used to extract the TM mode band structure. Time monitors collected the fields. Fast Fourier transform methods were used to compute the modal frequencies from the time domain field data. Mode profiles were calculated separately by exciting the system with a specific *k*-vector and frequency from a single TM-dipole source. A single frequency-domain field monitor captured the electric field profile across the unit cell. A modified silicon material with an imaginary index of zero was used to mitigate rapid material absorption loss in the silicon and enable clearer Fourier transforms in the band structure calculation. The real index was unperturbed. For consistency, this material was also used for the mode profiles.

Section 2.1 discusses all other pertinent details of methods.

### 4.2.2 Individual Nanowires

A single semiconductor nanowire is a cylindrical dielectric waveguide with loss at frequencies above the band edge due to material absorption. From free space, the leaky modes of a cylindrical waveguide are accessible and result in resonant absorption due to field confinement in the high index wire. These leaky mode resonances are defined by Equation (31), the eigenvalue equation for an infinitely long dielectric cylinder surrounded by air, derived from Maxwell's equations,[75,76,77]

$$\pm\left(\frac{1}{k_{cyl}^2}-\frac{1}{k_{air}^2}\right)^2\left(\frac{k_z m}{k_0 a}\right)^2 = \left(\frac{\varepsilon_{cyl}}{k_{cyl}}\frac{J_m^{'}\left(k_{cyl}a\right)}{J_m\left(k_{cyl}a\right)}-\frac{1}{k_{air}}\frac{H_m^{'}\left(k_{air}a\right)}{H_m\left(k_{air}a\right)}\right)\left(\frac{1}{k_{cyl}}\frac{J_m^{'}\left(k_{cyl}a\right)}{J_m\left(k_{cyl}a\right)}-\frac{1}{k_{air}}\frac{H_m^{'}\left(k_{air}a\right)}{H_m\left(k_{air}a\right)}\right) \quad (36)$$

where $m$ is the azimuthal mode order, $a$ is the cylinder radius, $\varepsilon_{cyl}$ is the complex permittivity of the cylinder, $k_0$ is the free space wavevector, $k_{cyl}$ and $k_{air}$ are the transverse components of the wavevector inside and outside of the cylinder, respectively, $k_z$ is the wavevector along the cylinder axis, and $J_m$ and $H_m$ are the $m$th order Bessel and Hankel functions of the first kind, respectively. Appendix B shows this derivation. Basic substitutions frame this equation in terms of $k_0$ and $k_z$, which describe the dispersion of each mode. Leaky waveguide modes are classified based on their azimuthal mode number, $m$, their radial mode number, $n$, which arises from the oscillatory behavior of the Bessel functions, and their polarization. Their polarization can be either TM (transverse magnetic, $H_z$=0), TE (transverse electric, $E_z$=0), HE (magnetoelectric, TM-like), or EH (electromagnetic, TE-like). The only modes that are strictly TE or TM for arbitrary wavevector are the $0^{th}$ order azimuthal modes, $TM_{0n}$ and $TE_{0n}$, and their solutions are found by setting the first and second term of the right hand side of Equation (36) equal to zero, respectively. For $m$>0, the HE and EH mode solutions can be found by selecting the (+) and (-) on the left hand side of the equation, respectively. The solutions to the eigenvalue equation ($k_0(k_z)$ ) are complex, where the real parts are indicative of the resonant wavelength and propagation constant and the imaginary part is indicative of the radiative loss of the mode, which for a lossless dielectric is a measure of the accessibility of a mode from free space and approaches zero (becoming inaccessible) as the mode transitions from leaky to guided ($k_z \rightarrow 0$ *as* $k_{air} \rightarrow 0$).[78] For a lossy dielectric, $k_z$ is also a measure of the absorptive loss.

#### *4.2.2.1 Illumination Perpendicular to Wire Axis*

The simplest case for analysis of this eigenvalue equation is illumination perpendicular to the nanowire axis. In this case, $k_z$ is zero, the left hand side of the equation becomes zero, and all

modes become either completely TM or TE for any azimuthal order, *m*. As for the case of *m*=0, described above, setting the 1st term (2nd term) of the right hand side of Equation (31) equal to zero gives the TM (TE) modes. Table 4 summarizes the normalized eigenvalues, $k_0 r$, for a dielectric cylinder with a constant and real index, $n_{cyl}$=4. It is instructive to schematically analyze the mode eigenvalues for a real and constant index rather than a complex varying index of a real material such as silicon in order to make a fair comparison between two eigenmodes, specifically between their imaginary parts which become a convolution of radiative loss from the mode and absorption loss in the material when a complex index is used.

**Table 4: Leaky waveguide mode eigenvalues, $k_0 r$, for a dielectric cylinder with *n*=4.**

| | n=1 | | n=2 | |
|---|---|---|---|---|
| M | TE | TM | TE | TM |
| 0 | 0.58-0.041i | 0.20-0.089i | 1.36-0.056i | 0.99-0.068i |
| 1 | 0.91-0.044i | 0.58-0.041i | 1.73-0.063i | 1.36-0.056i |
| 2 | 1.23-0.016i | 0.93-0.013i | 2.05-0.069i | 1.72-0.036i |

In general, the real part of the eigenvalue increases and the imaginary part of the eigenvalue decreases with increasing mode number, which indicates that higher order modes occur at higher frequencies (shorter wavelengths) and have less radiative loss, or in another light, are more difficult to couple to from free space, which implies smaller total absorption and smaller spectral width.[78]

Simulated absorption results for a 75 nm radius silicon nanowire, illuminated perpendicular to its wire axis, demonstrate the validity of the above analytic analysis. Figure 31 shows absorption efficiency, $Q_{abs}$, of the silicon nanowire (defined as its absorption cross section normalized to its physical cross section) as a function of wavelength for both TE and TM polarized incident light, with the spectral positions of leaky waveguide mode resonances within the 400 to 900 nm range indicated above along with profiles of the electric field intensity, $|E|^2$, for the nanowire cross section at the resonant wavelengths for the $TM_{11}$, $TM_{21}$, $TM_{12}$, $TE_{01}$, and $TE_{11}$ modes. The inset of Figure 31 illustrates the orientation for TE polarization. In their displayed orientation, the light is first incident on the left side of the field profiles, causing slight distortions in the mode profiles due to material absorption. The distortion is more prominent at shorter wavelengths where silicon absorbs more strongly. The peak spectral positions in Figure 31 indicate that the incoming plane wave excites each of the modes predicted from Equation (31); Figure 31 also displays a subset of their field profiles at the top for visual verification of coupling into the predicted modes. The field profiles of these modes, as determined from analytic theory, can be found in references 53, 75-77. Peak spectral widths are smaller for higher order modes, as expected from the imaginary parts of the eigenvalues, which decrease with increasing mode order. The overall absorption efficiency into each mode is influenced more strongly by the rapidly changing absorption coefficient of silicon, than by its eigenvalue.

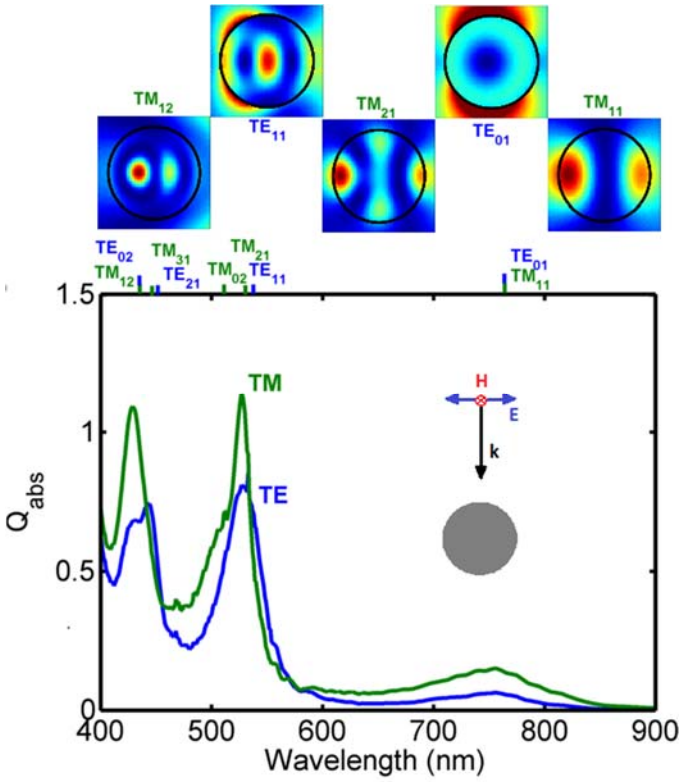


**Figure 31: Simulated absorption efficiency vs. wavelength for a silicon nanowire (*r*=75 nm) illuminated perpendicular to its axis for both TE (blue) and TM polarized (green) light, with the inset showing the orientation for the TE polarization; spectral positions of leaky mode resonances within the 400-900 nm wavelength range are indicated above, accompanied by the observed electric field intensity profiles at the resonant wavelengths for the $TM_{11}$, $TM_{21}$, $TM_{12}$, $TE_{01}$ and $TE_{11}$ modes.**

### *4.2.2.2 Illumination Parallel to the Wire Axis*

For photovoltaic applications, vertically-oriented nanowires are of primary interest, motivating analysis of illumination parallel to the nanowire axis. Figure 32 displays a plot of absorption efficiency vs. wavelength for a silicon nanowire (*r*=75 nm, *L*=2 μm) illuminated parallel to its axis, with insets of the electric field intensity profiles for the nanowire cross section at the wavelengths of the two dominant absorption peaks at 445 nm and 800 nm. The closely spaced oscillations that

become prominent when the absorption coefficient of silicon decreases dramatically beyond 550 nm are due to Fabry-Perot resonances, which are a product of the finite length of the wire. From the field profiles, it is clear that the peaks at the 445 nm and 800 nm can be attributed to the $HE_{12}$ and $HE_{11}$ leaky waveguide modes, respectively. The field profiles of these modes, as determined from analytic theory, can be found in references 75-77. Note that these modes are related to the $TM_{12}$ and $TM_{11}$ modes from the previous section, but the introduction of a finite $k_z$ results in the mode no longer being completely transverse magnetic.

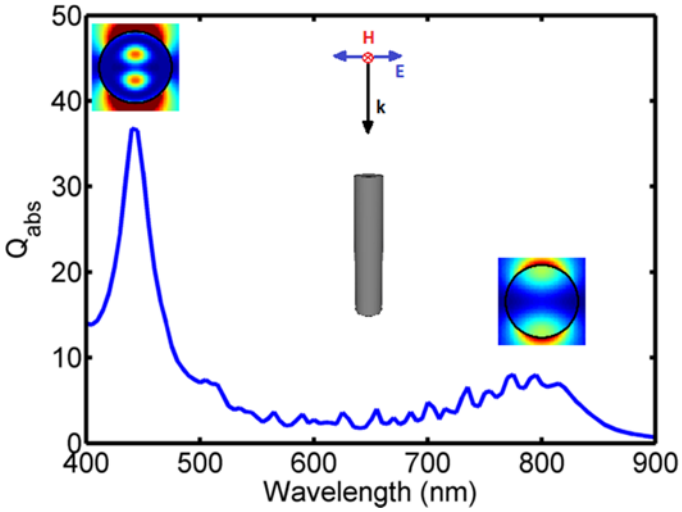


**Figure 32: Simulated absorption efficiency vs. wavelength for a silicon nanowire (*r*=75 nm, *L*=2 µm) illuminated parallel to its axis (TEM polarization), with the inset showing the orientation and the electric field intensity profiles at the two main absorption peaks displayed above.**

For the case of an incoming wavevector aligned perfectly parallel to the nanowire axis ($k_z=k_0$), the transverse wavevector in air, $k_{air}$, becomes zero and the eigenvalue equation is ill-defined as the leaky modes transition into guided modes and are no longer accessible from free space. However, near the nanowire, the wave front of the free space plane wave is perturbed by the high index nanowire, introducing transverse components to the wavevector and enabling coupling into leaky

waveguide modes. The overlap between the initial symmetry of the electric field of the incoming plane wave and that of the in-plane electric field of the $HE_{1m}$ modes explains the preferential coupling into the $HE_{11}$ and $HE_{12}$ modes at normal incidence.[79,80] At other angles of incidence, this symmetry is broken and resonant absorption peaks for other leaky waveguide modes appear.

It is also interesting to note that the peak position of both the $HE_{11}$ (800 nm) and the $HE_{12}$ (445 nm) modes at parallel incidence are slightly red-shifted from those of the $TM_{11}$ (765 nm) and $TM_{12}$ (430 nm) modes at perpendicular incidence. The full dispersion relations for the leaky waveguide modes, $k_0(k_z)$, explain this phenomenon. Figure 33 displays the real parts of the dispersion relation for the TM-polarized modes, overlaid with the light line ($k_0 r = k_z r$) beyond which leaky modes transition to guided modes and are inaccessible from free space. The calculations were performed for a silicon nanowire with a radius of 75 nm, using the full complex refractive index of silicon. These dispersion curves illustrate the dependence of resonant wavelength, $k_0 = 2\pi/\lambda$, on angle of incidence, $\vartheta$, which we can relate to $k_z$ with a simple cosine relation: $k_z = k_0 \cos(\vartheta)$, so that $k_z = 0$ is illumination perpendicular to the wire axis and $k_z = k_0$ is illumination parallel to the wire axis. The TM-polarized modes with $m > 1$ are fairly flat, indicating minimal dependence of the spectral resonance on angle of illumination. The TM modes with $m \leq 1$ are fairly flat for small values of $k_z$, but become significantly perturbed as $k_z$ approaches $k_0$. Specifically, the resonant positions of the $HE_{11}$ and $HE_{12}$ modes shift to lower frequencies or, equivalently, longer wavelengths. This case of $k_z$ near $k_0$ is relevant for illumination parallel to the nanowire axis and explains the red-shift in peak positions of the $HE_{11}$ and $HE_{12}$ relative to those for illumination perpendicular to the nanowire axis.

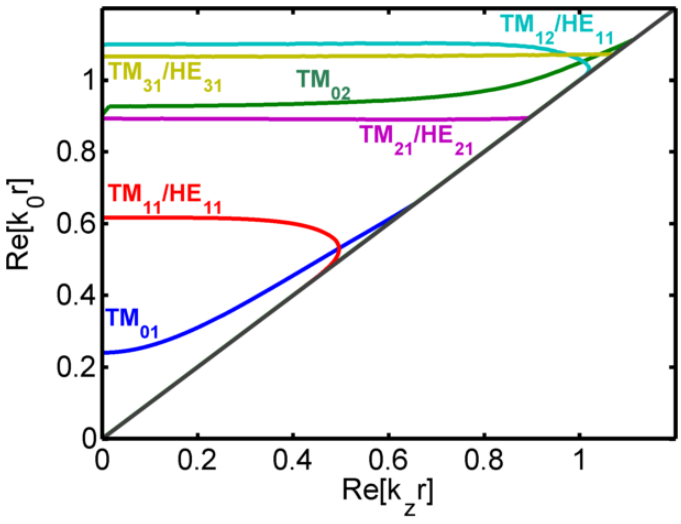


**Figure 33: Dispersion relation, $k_0r$ $(k_zr)$ for the TM-polarized eigenmodes of a silicon nanowire with radius of 75 nm.**

### 4.2.3 Nanowire Arrays

Vertically-oriented nanowire arrays are the most relevant arrangement of nanowires for photovoltaic and photoelectrochemical applications. Therefore, the next step in the analysis is to introduce periodicity. Figure 34 displays simulated absorption vs. wavelength for a square-lattice array of silicon nanowires ($r$=75 nm, $L$=2 μm) with 1000 nm spacing illuminated parallel to the nanowire axes, accompanied by the electric field intensity of the nanowire cross section at the two absorption peaks (440 nm and 775 nm). The absorption curve is qualitatively similar to the absorption efficiency curve of the individual nanowire (Figure 33), with two dominant absorption peaks and closely spaced sharp oscillations beyond 550 nm. The electric field intensity profiles reveal that the absorption peaks correspond to resonant absorption into the $HE_{11}$ and $HE_{12}$ modes, as before, and the sharp oscillations are again attributed to Fabry-Perot resonances of the nanowire. These results indicate that leaky waveguide mode theory of individual wires is sufficient to describe sparse nanowire arrays.

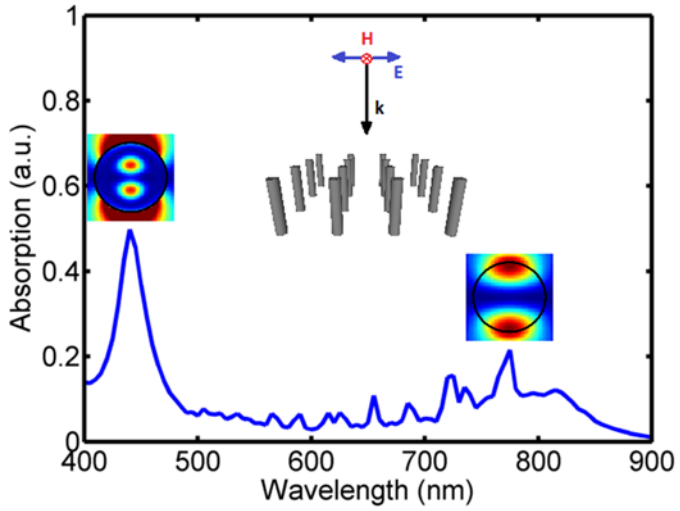


**Figure 34: Absorption vs. wavelength for a square-lattice array of silicon nanowires (*r*=75 nm, *L*=2 μm) with 1000 nm spacing illuminated parallel to the nanowire axis, with inset for orientation and electric field intensity profiles at the absorption peaks displayed above.**

Conceptually, the existence of leaky waveguide modes of single nanowires within an array is not obvious. A periodic array of nanowires is a 2D photonic crystal and thus any mode that propagates in the periodic plane is by definition a photonic crystal mode. To unify these two concepts, an extension of the analogy of the electronic crystal to the photonic crystal is proposed.[81] As isolated atoms move together to form a crystal, the isolated electronic energy levels of a single atom transition to electronic bands of a crystal. At large inter-atomic spacings, the crystal lattice only slightly perturbs the isolated energy levels of the individual atoms. Similarly, when inter-nanowire spacing is large, the nanowire lattice only slightly perturbs the isolated photonic modes of the individual nanowires.[79,82,83]

To demonstrate this analogy, Figure 35 displays the photonic crystal band diagrams for silicon nanowire arrays (*r*=75 nm) with lattice spacings of 150 nm (close-packed) and 250 nm. At larger spacings, the density of air mode bands becomes too high to distinguish them from the leaky

waveguide modes that are localized around the nanowire. These band structures are overlaid with the frequency positions of the $TM_{11}$, $TM_{21}$, and $TM_{12}$ leaky waveguide modes at $k_z$=0 (black, flat lines), and the electric field intensity profiles for the photonic crystal bands nearest the leaky waveguide mode resonances are displayed to the side. Independent of nanowire spacing, the mode profiles of the bands nearest the leaky waveguide mode resonances correspond to the expected field profiles for the leaky waveguide modes. This observation indicates that the nanowire array resonant modes do in fact arise from the leaky waveguide modes of individual nanowires. Additionally, for the larger nanowire spacing, 250 nm, the photonic crystal bands corresponding to the leaky waveguide modes are nearly flat, indicating very weak dependence on the periodicity of the lattice. As the nanowire spacing decreases, these bands curve, indicating perturbation of the modes by the lattice. This perturbation is expressed in the mode profiles, which are more confined for close-packed nanowire arrays.

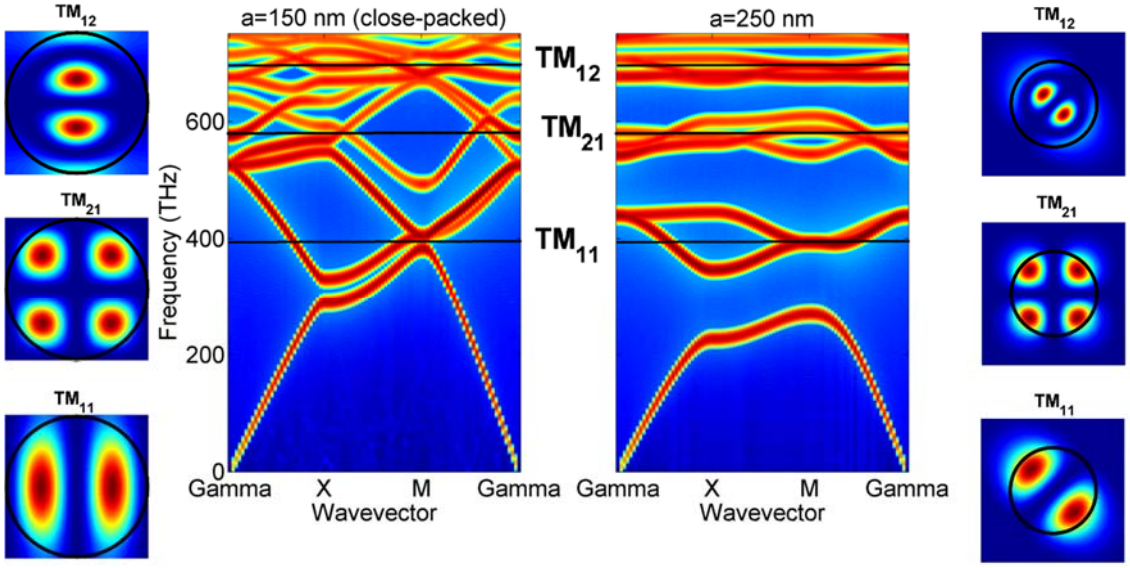


**Figure 35: Photonic crystal band diagrams for silicon nanowire arrays (*r*=75 nm) for lattice spacings, *a*=150 nm (close-packed) and *a*=250 nm, overlaid with the positions of the $TM_{11}$, $TM_{21}$,**

**and $TM_{12}$ leaky waveguide modes (black, flat lines); electric field intensity profiles for the photonic crystal bands nearest the leaky waveguide mode resonances are displayed to the side.**

A recent publication from Sturmberg et al. provides a more rigorous mathematical treatment of the connection between leaky waveguide modes and Bloch modes, which corroborates the above analysis.[83] They derive a modified version, Equation (38), of the leaky waveguide eigenvalue equation for the first order ($m$=1) modes that accounts for nearest neighbor interactions in infinitely periodic nanowire arrays. This eigenvalue equation is reproduced here, generalized for all mode orders, where $S_0$ is the first coefficient of the Rayleigh identity for an infinite lattice, representing the nearest neighbor interactions within the lattice.

$$\left(\frac{\varepsilon_{cyl}}{k_{cyl}}\frac{J_m^{'}\left(k_{cyl}a\right)}{J_m\left(k_{cyl}a\right)}-\frac{1}{k_{air}}\frac{H_m^{'}\left(k_{air}a\right)+S_0J_m^{'}\left(k_{air}a\right)}{H_m\left(k_{air}a\right)+S_0J_m\left(k_{air}a\right)}\right)$$
$$\left(\frac{1}{k_{cyl}}\frac{J_m^{'}\left(k_{cyl}a\right)}{J_m\left(k_{cyl}a\right)}-\frac{1}{k_{air}}\frac{H_m^{'}\left(k_{air}a\right)+S_0J_m^{'}\left(k_{air}a\right)}{H_m\left(k_{air}a\right)+S_0J_m\left(k_{air}a\right)}\right)=\pm\left(\frac{1}{k_{cyl}^2-k_{air}^2}\right)^2\left(\frac{k_zm}{k_0a}\right)^2 \quad (37)$$

For sparse arrays of nanowires, coupling between nanowires is weak and, thus, $S_0$ is small; in the infinitely dilute limit, $S_0$ approaches zero and the modified eigenvalue equation for a nanowire array, Equation (37), reduces to the original waveguide eigenvalue equation for an individual nanowire, Equation (36). A positive value for $S_0$ indicates constructive interference of the fields of neighboring nanowires at their interfaces, and, conversely, a negative value indicates destructive interference. For $S_0$=0.5 (constructive interference), $k_z$=0 and a constant, real index material ($n$=4), the eigenvalue of the $TM_{11}$ mode shifts from 0.58-0.041$i$ (Table 4) to 0.57-0.058$i$, revealing a red-shift in the resonant wavelength (~10 nm for a 75 nm radius nanowire) and an increase in the

radiative loss of the mode, indicating a decrease in mode confinement. Larger, positive values of $S_0$ result in larger shifts in the same directions.

Conceptually, the red-shift and reduction in mode confinement emulates the effects of an increase in the refractive index of the surrounding medium; this apparent increase in refractive index of the surrounding medium is a localized effect at the nanowire interface due to the constructive interference of the fields. The opposite trend (blue-shifting and increased confinement) is observed for negative values of $S_0$, stemming from the destructive interference of fields and a localized effective decrease in the refractive index of the medium. For a given structure, $S_0$ varies with *k*-vector, and therefore, the photonic crystal Bloch mode band can be blue- and red-shifted with respect to the leaky waveguide mode to which it corresponds (Figure 35). As array density increases, the magnitude of $S_0$ increases due to stronger inter-nanowire coupling and, consequently, the photonic crystal Bloch mode band becomes more dispersive. The close-packed nanowire array in Figure 35 illustrates this effect through the increased band bending and confined field profiles.

Ultimately, the leaky waveguide modes of individual nanowires relate to the resonantly absorbing modes of a 2D photonic crystal nanowire array. The spectral positions of the leaky waveguide mode resonances were predicted using an eigenvalue equation derived from Maxwell's equations using analytic waveguide theory. The full dispersion relations derived from this equation explained the red-shifting of the $HE_{11}$ and $HE_{12}$ modes when illumination changed from perpendicular to parallel to the nanowire axis, and symmetry arguments explained the selective coupling of a plane wave incident parallel to the nanowire axis into only the $HE_{11}$ and $HE_{12}$ modes. The addition of a sparse lattice only weakly perturbs the leaky waveguide modes of individual

nanowires, and thus, leaky waveguide mode theory effectively describes the absorption behavior of sparse nanowire arrays.

## 4.3 Optimization of Light Absorption in Semiconductor Nanowire Arrays

This section presents design methods for achieving near-unity broadband light absorption in sparse nanowire arrays, illustrated by results for visible absorption in GaAs nanowires on Si substrates. Sparse (<5% fill fraction) nanowire arrays achieve near-unity absorption at wire resonant wavelengths due to coupling into 'leaky' radial waveguide modes of individual wires, as explained in detail in the previous section. However, an ideal solar cell would exhibit near-unity absorption across the entire UV-Vis-NIR spectrum up to its bandgap. State-of-the-art GaAs solar cells with thicknesses exceeding several microns can achieve near-unity broadband absorption in the visible wavelength range, but exhibit incomplete light absorption for the near-IR wavelengths close to the semiconductor bandgap. In principle, resonant absorption in nanostructures via sub-wavelength light trapping phenomena, such as leaky radial waveguide mode absorption, can exceed the Lambertian absorption limit over a narrow wavelength range near resonance.[55,84,85,86] However, owing to the discrete nature of resonant modes in nanowires, achieving near-unity broadband absorption is challenging and is not possible in sparse wire arrays with uniform diameter. Therefore, in order for nanostructured devices to compete with current state-of-the-art planar devices in photovoltaic conversion efficiency, optical design methods can be employed to increase the number of resonances and the wavelength range for resonant mode excitation, given the inherently spectrally-dependent resonant characteristics of nanowire radial modes. Previous reports on nanowire arrays have demonstrated the ability to alter nanowire array light absorption with geometric modification of nanowire diameter, shape and order.[52,59,63,64,66,87,88,89,90,91,92,93,94,95] Specifically, the anti-reflective properties of tapering silicon

nanowires have been discussed theoretically[94] and demonstrated experimentally.[95] This work extends the scope of these studies by developing an analysis of the absorption enhancement in tapered nanowires in the context of resonant modal absorption. The strategy adopted herein takes a directed approach to geometric optimization of nanowire arrays, guided by the theory of localized mode excitation in nanowires, to achieve near-unity broadband absorption in sparse arrays. This section proposes two simple pathways to achieving a broadband enhancement in nanowire array light absorption: (i) introducing multiple wire radii within a small unit cell array to increase the number of resonant wavelengths and (ii) tapering nanowires to introduce a continuum of diameters and resonant wavelengths within a single wire.

The design principles and methods are discussed in the context of GaAs nanowires on a Si substrate, but are generally applicable to any sparse array of semiconducting nanowires in which radial leaky waveguide modes are the primary mechanism responsible for resonant absorption. Because a primary concern for GaAs- and other III-V material-based photovoltaics is material cost, an equal material usage constraint is applied to the array optimizations. Additionally, this equal material usage comparison highlights differences in absorption/volume, and thus, underscores the effects of the modal resonances for varying geometries. Consequently, all designs discussed have a 5% fill fraction and a constant nanostructure height of 3 μm, corresponding to a 150 nm planar equivalent thickness. These dimensions correspond closely to those of the experimentally fabricated nanowire arrays discussed in Section 4.1.

### 4.3.1 Multi-Radii Nanowire Arrays

Conceptually, the simplest extension of the electromagnetic principles observed in the uniform nanowire arrays in order to achieve broadband absorption is to introduce multiple nanowire radii in a single small unit cell array. Because the leaky mode resonances depend only on nanowire

radius and not on array period, the inclusion of multiple nanowire radii in one array leads to an increase in the number of leaky mode resonances available without altering or eliminating the already existing resonances. The large extinction cross sections of the individual nanowires near resonance enables incident light of a given wavelength to be captured by the nanowire with the appropriate spectral resonance, as illustrated in Figure 37. Notably, this mechanism becomes less efficient as the distance between identical radii nanowires approaches and exceeds the nanowire scattering cross section. Figure 36 displays the scattering and absorption cross section enhancement factors for a 3 µm long GaAs nanowire with an 80 nm radius, calculated using the 3D Mie scattering setup in Lumerical FDTD. These cross section enhancement factors provide guidance for maximum spacing between wires of equal radii. The peaks in the enhancement factors are 165 and 62 for scattering ($\lambda$=910 nm) and absorption ($\lambda$=890 nm), corresponding to 1027 and 629 nm radii. These radii indicate that at 5% fill fraction, a 2 x 2 unit cell of nanowires with disparate radii is appropriate.

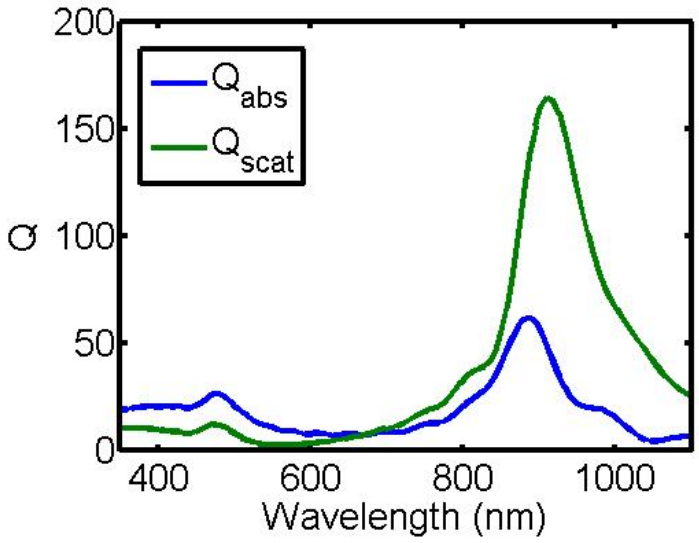


**Figure 36: Scattering and absorption cross section enhancement factors, $Q_{scat}$ and $Q_{abs}$, as a function of wavelength for a 3 µm long GaAs nanowire with an 80 nm radius.**

Figure 37(a) and (b) illustrate the general setup considered - an array containing four different nanowire radii (45, 55, 65, and 75 nm), arranged in a repeating 2 x 2 unit cell to create an infinite array. Each of these nanowires supports leaky modes at different resonant wavelengths, depending on its radius. To demonstrate this, simulations of the light absorption in the multi-radii array recorded the absorption in each wire individually. Figure 37(c) shows a plot of the fraction of incident power absorbed in each nanowire as a function of wavelength. The four dominant peaks correspond to the $HE_{11}$ modes of the nanowires, which red-shift with increasing radius, as predicted by the eigenvalue equation, Equation (36). The predicted resonant wavelength for the $HE_{11}$ modes of the 45, 55, 65, and 75 nm radii nanowires are 515, 590, 675, and 760 nm, respectively, as indicated in Figure 37(b) and (c). In this case, the peaks in the absorption curve are slightly red-shifted with respect to the predicted resonant wavelengths. This red-shifting is due to the dispersion curve of the $HE_{11}$ resonance, which shifts to longer wavelengths as the propagation angle shifts from perpendicular to parallel to the wire axis, as discussed in detail in the previous section and displayed in Figure 33. Additionally, the absorption curves for the largest radii nanowire ($r$=75 nm) exhibits a second absorption peak in the blue region, which corresponds to the $HE_{12}$ resonance, predicted to occur at 440 nm. Field profiles of nanowire cross sections within this array confirm coupling into the $HE_{11}$ and $HE_{12}$ modes, as discussed above. Therefore, these results confirm that a multi-radii nanowire array increases the number of spectral resonances and results in broader absorption than for a uniform nanowire array.

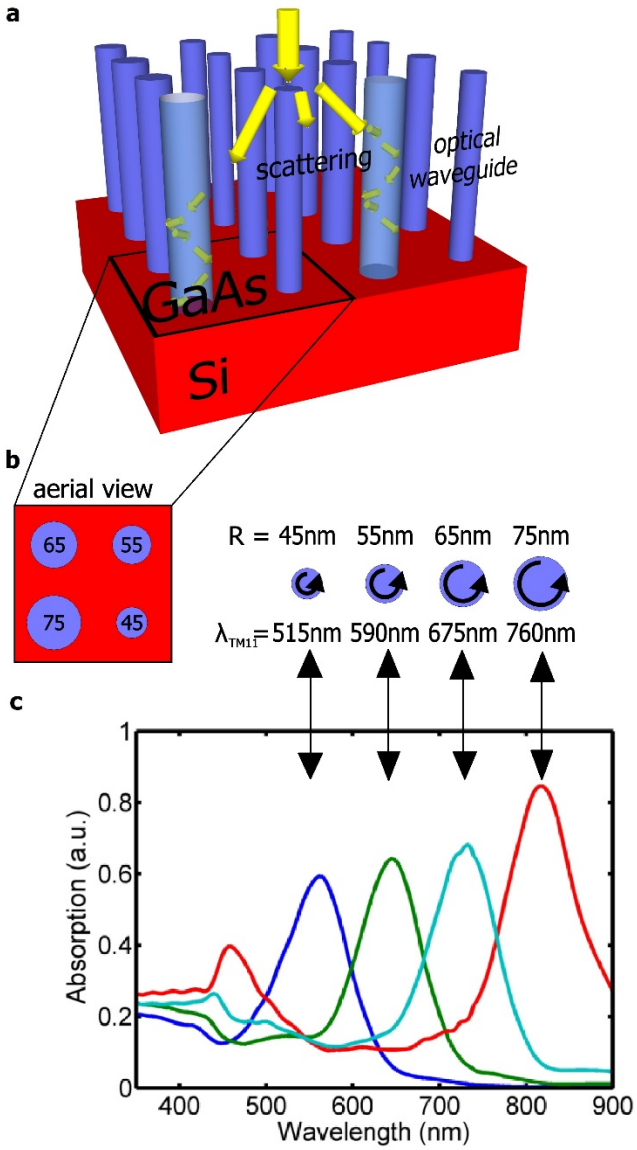


**Figure 37: (a) Schematic of the mechanism of scattering and coupling into resonant leaky radial optical waveguide modes in the nanowire array with multiple radii; (b) aerial view of one unit cell of the array with multiple nanowire radii and schematic of radial modes in nanowires of various radii, labeled with their $HE_{11}$ resonant wavelengths; (c) absorption vs. wavelength for each individual wire in the optimized multi-radii wire array depicted in (a) with arrows indicating corresponding curve/peak and wire radius.**

### 4.3.2 Nanocone Arrays

The second approach taken to achieve near-unity array absorption across the spectrum is to extend the wavelength span of a single mode excited in an array of cylindrical wires by modifying the geometry to consist of an array of nanocones. To extend its resonance wavelength range, a nanowire can be tapered to form a truncated nanocone, which has a continuum of radii and, thus, a spectrum of resonant wavelengths for a single mode.

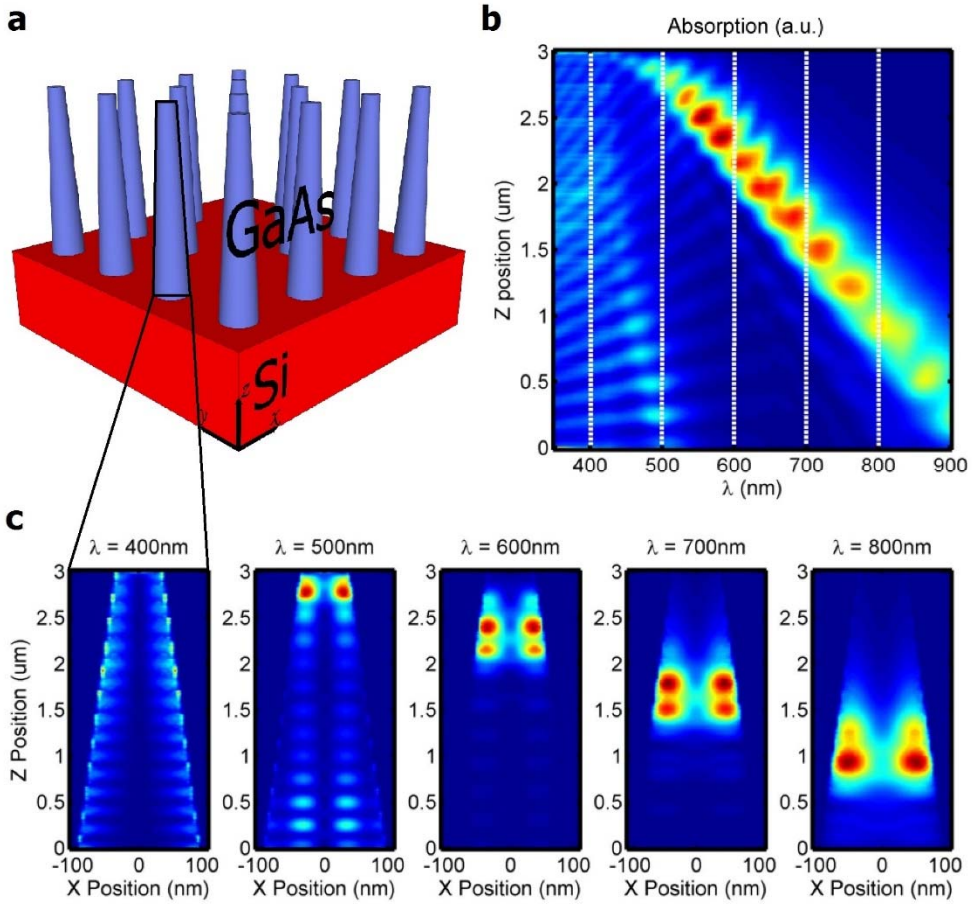


**Figure 38: (a) Array of optimized GaAs truncated nanocones with tip radii of 40 nm, base radii of 100 nm and heights of 3 µm, labeling *x*, *y*, and *z* dimensions and indicating the vertical cross section shown in (c); (b) absorption in a single truncated nanocone integrated over *x* and *y*, its**

**radial cross section, (red indicating strong absorption and blue indicating little to no absorption) as a function of both wavelength and position along the z axis (labeled in a); (c) *xz* (vertical) cross sections of absorption for a single nanocone illuminated at wavelengths of 400, 500, 600, 700 and 800 nm.**

To illustrate that a nanocone array exhibits resonant absorption via the same leaky radial waveguide modes as a nanowire with a uniform radius, simulations recorded three-dimensional maps of the absorbed power as a function of wavelength for a nanocone with a tip radius of 40 nm and base radius of 100 nm. Figure 38(a) shows a schematic of this array. Figure 38(b) displays a plot of power absorbed in the nanocone as a function of wavelength and position along its vertical axis. Because the nanocone is tapered, the vertical coordinate, *z*, is equivalent to a varying radius coordinate, where *z*=3 μm corresponds to a radius of 40 nm and *z*=0 μm corresponds to a radius of 100 nm. The largely red diagonal peak stretching from *z*=0 μm and $\lambda$~900 nm up to *z*=3 μm and $\lambda$~500 nm, the most prominent feature of Figure 38(b), is the absorption into the resonant $HE_{11}$ mode. The radial cross sections of the absorbed power at the resonant wavelength-radius pairs indicated by the prominent diagonal peak in Figure 38(b) confirmed coupling into the $HE_{11}$ mode of the nanocone. Additionally, these wavelength-radius pairs match the eigenvalues predicted by Equation (36). In addition to the strong $HE_{11}$ peak observed in Figure 38(b), a second, fainter diagonal peak is visible, stretching from *z*=0 μm and $\lambda$~500 nm up to *z*~1.5 μm and $\lambda$~450 nm. The $HE_{12}$ mode is responsible for this resonant absorption. The peak slowly fades away for larger *z* as the nanocone radius decreases and ultimately disappears around *r*=70 nm (or *z*=1.5 μm), where the mode is no longer accessible due to the dispersion curve of GaAs. The diagonal character of both the $HE_{11}$ and $HE_{12}$ peaks demonstrates that these modes have a spectrum of resonant wavelengths in a nanocone, as intended.

Another interesting feature of Figure 38(b) is the sinusoidal variation of the absorbed power along the *z* axis. This modulation in absorption is due to longitudinal resonances, and the overall absorbed power intensity profile of Figure 38(b) is explained by a linear combination of longitudinal resonances and radial resonances. This phenomenon is more clearly discernible from *xz* cross sections of the power absorbed in a nanocone, displayed in Figure 38(c) for wavelengths of 400, 500, 600, 700, and 800 nm. All five of these cross sections illustrate the longitudinal modes present in the nanocone which give rise to the characteristic vertical oscillations in absorption intensity. Focusing on the four longer wavelength cross sections, the radial $HE_{11}$ resonance shifts downward to larger radius with increasing wavelength and has multiple lobes in the vertical direction due to its convolution with the longitudinal resonances. No strong radial mode is visible for the 400 nm wavelength cross section because GaAs absorbs strongly in this region and light does not penetrate deep enough into the nanocone to establish a radial mode. Additionally, in the 500 nm wavelength cross section, the character of the $HE_{12}$ mode is visible at the bottom of the nanocone, as an additional radial absorption peak becomes visible at the rim of the nanocone. This detailed analysis of nanocone absorption confirms that arrays of truncated nanocones exhibit spectrally-extended resonances and provide another method for achieving a more broadband optical absorption response in nanowire arrays.

### 4.3.3 Optimization of Light Absorption

Using the conceptual understanding developed above, directed optimization using modest geometric modifications can be employed to realize broadband light absorption in sparse nanowire arrays. Figure 39(a), (b), and (c) show schematics of the optimized structures, along with their power absorption profiles for a 65 nm radii nanowire cross section ($\lambda_{res}$=675 nm) and their

absorption curves. The side-by-side display of the power absorption cross sections, Figure 39(b), in each optimized structure underscores their essentially identical $HE_{11}$ modal characteristic.

As previously mentioned, the optimizations were performed under the constraint of constant fill fraction (5%) and constant nanostructure height (3 μm), corresponding to a 150 nm planar equivalent thin film. For comparison, the planar equivalent thin film absorbs 10.5 $mA \cdot cm^{-2}$ and the uniform array of 65 nm radii nanowires absorbs 25.0 $mA \cdot cm^{-2}$. Figure 39(c) displays the absorption curves for these cases as the black (planar) and red (uniform) lines. Note that simulation of the planar layer used partial spectral averaging to smooth out the Fabry-Perot resonances. All nanostructures are positioned on top of an infinite Si substrate and embedded in a 30 nm layer of $SiO_x$ to emulate SAG-MOCVD as-grown structures.[67]

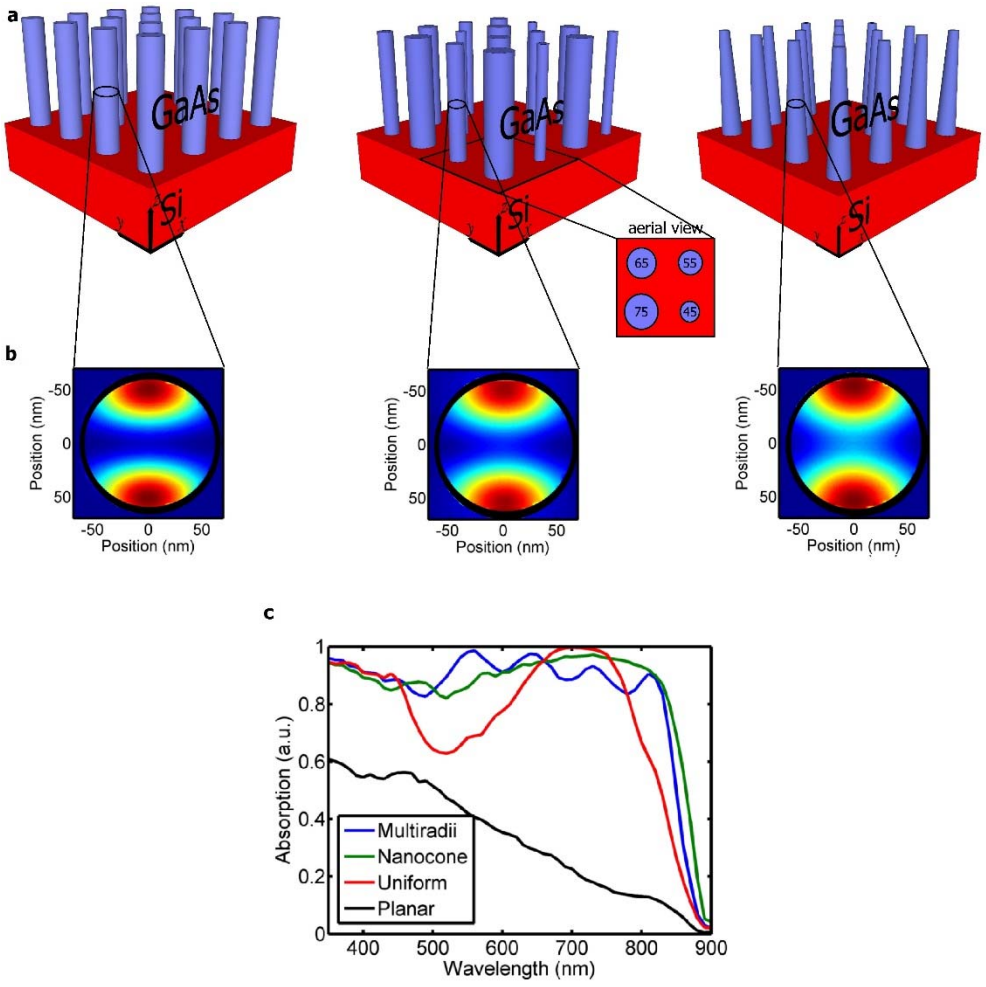


**Figure 39: (a) Diagrams of sparse arrays of (i) uniform nanowires with radii of 65 nm, (ii) nanowires with varying radii (45, 55, 65, 75 nm) with inset of aerial layout, and (iii) truncated nanocones with tip radii of 40 nm and base radii of 100 nm; (b) cross sections of normalized power absorbed at the $HE_{11}$ resonance at 675nm for (i) a 65nm radius nanowire in a uniform array, (ii) a truncated nanocone at *r*=65 nm and (iii) a 65 nm radius nanowire in the multi-radii nanowire array (black circles outline the edges of the wire); (c) simulated absorption vs. wavelength for the geometrically-optimized GaAs arrays of truncated nanocones shown in (a) and the planar equivalent thickness (*t*=150 nm). All nanostructured arrays are 3 μm in height,**

**have a 5% fill fraction, sit on top of an infinite silicon substrate and are embedded in 30 nm of silica (not shown).**

For the multi-radii nanowire array optimization, computational constraints limited the number of different wire radii in a single array to four, which were arranged in a 2 x 2 unit cell, as shown in Figure 37 and Figure 39(a). For the optimization, all unique combinations of nanowires with radii of 50, 60, 70, 80, and 90 nm were simulated, holding height and fill fraction constant at 3 μm and 5%, respectively. These radii were chosen because their $HE_{11}$ and $HE_{12}$ resonances span within the UV-Vis-Near-IR spectrum up to the bandgap of GaAs ($\lambda$~350-900 nm). Broadband simulations determined the optimized case to be a unit cell with wire radii of 50, 60, 70, and 80 nm; however, due to fitting errors in the imaginary part of the refractive index for broadband simulations, single wavelength simulations determined the final optimized case to be an array with radii of 45, 55, 65, and 75 nm. Figure 39(c, blue line) shows the absorption as a function of wavelength for this case, which achieves an absorbed photocurrent density of 28.8 $mA \cdot cm^{-2}$, corresponding to a 15% improvement over the uniform nanowire array. As implied from the individual wire absorption curves in Figure 37(c), the total array absorption curve has four strong peaks distributed relatively evenly across the visible spectrum and an extended shoulder around 450 nm, which correspond to absorption into the $HE_{11}$ modes corresponding to each wire radius and the $HE_{12}$ mode of the 75 nm radius wire, respectively. A previous study by Sturmberg et al. using a Bloch wave expansion to frame the modal analysis found that when multiple wire radii are included within a 30% fill fraction array of silicon nanowires, nearly a 30% increase in absorbance was found for a 2 x 2 unit cell array over a uniform array.[83] Additionally, they extended their study to include 4 x 4 unit cell arrays, and achieved an additional 4% improvement over the optimized 2 x 2 case. The findings of Sturmberg et al. indicate that larger unit cell arrays could yield additional improvement in

absorbed current density. By contrast, this study focuses on lower array fill fractions, such that the scattering cross sections of nearest neighbor wires overlap, but the scattering cross sections of second-nearest neighbors and beyond do not overlap. In this sparse array limit, larger unit cells face diminishing returns because the period of the sub-lattice for each wire radii exceeds the wire scattering cross section, preventing incident light from coupling into the appropriate resonant structure.

The optimization of truncated nanocone dimensions varied the tip radii of the nanocones between 30 and 60 nm and the base radii between 70 and 100 nm, in 10 nm increments, holding height and fill fraction constant at 3 μm and 5%, respectively. Optimum absorption occurred for an array of truncated nanocones with tip radii of 40 nm and base radii of 100 nm, achieving an absorbed photocurrent density of 29.5 $mA \cdot cm^{-2}$ and an 18% improvement over the uniform array absorption (Figure 39(c), green line). At these dimensions, the extended resonance spectrums of the two HE modes overlap by more than 50 nm, enabling the observed near-unity broadband absorption. The truncated nanocone absorption equals or exceeds that of the uniform array except in the region of the $HE_{11}$ resonance of the uniform array (650-750 nm). The higher absorption in the uniform array in this spectral region is due to a difference in vertical distance over which the mode is resonant: the entire length of the uniform wire compared to only a small fraction of the nanocone length.

Using a theoretical understanding of the leaky mode resonant absorption in sparse nanowire arrays, modest geometric modifications were used to achieve near-unity broadband absorption. Simulation of arrays with multiple wire radii and tapering achieve a 15 and 18% improvement, respectively, over a uniform array, by increasing the resonant portion of the AM1.5G spectrum. For selective area growth using metalorganic chemical vapor deposition, the arrays of truncated

nanocones are experimentally achievable by altering the growth conditions[96] and the wire arrays with multiple wire radii are experimentally achievable by altered definition of the patterned substrate. The nanocone structure is also achievable via a crystal facet-selective wet etch, such as KOH for tapered silicon nanowires.[95] While a nanocone array is predicted to achieve marginally higher absorption than a multi-radii array, the effect of modifying the wire growth conditions and introduction of new exposed crystal facets may alter the electronic properties of the array. Given the relatively small difference in their absorption performance (<1 $mA \cdot cm^{-2}$), both nanocone arrays and multi-radii wire arrays are promising routes to improve the optoelectronic performance of sparse semiconductor nanowire arrays as solar cells.

## 4.4 Fabrication and Characterization Efforts toward the Optimized Structures

This section discusses initial experimental efforts designed to verify the simulation optimization results and achieve near-unity absorption in sparse arrays of III-V nanowires. Largely due to equipment and materials availability, these efforts focused on the phosphide family—InP, GaP, and InGaP. Nevertheless, the phosphide family has been reported to have some interesting properties for $CO_2$ reduction. Specifically, GaP in the presence of pyridine has been shown to selectively reduce $CO_2$ to methanol.[97] This property is potentially of great importance for the next phase of JCAP, where the focus is on $CO_2$ reduction and selectivity is a primary challenge.

Two nanowire array fabrication methods were pursued in parallel—MOCVD growth and reactive ion-etching (RIE). The MOCVD growth efforts focused on GaP and achieved nanowire morphology control. RIE efforts focused on fabrication of InP nanowire arrays and achieved control of nanowire morphology. The resulting arrays were optically and electrically characterized.

### 4.4.1 MOCVD of GaP Nanowire Arrays

This section presents a hybrid selective area and self-catalyzed MOCVD growth method for ordered arrays of vertically-oriented gallium phosphide (GaP) nanowires on a silicon (Si) (111) substrate with morphology control. This hybrid growth method is justified by unsuccessful attempts to achieve high aspect ratio GaP structures via a solely selective area growth method. This study examines the effects of temperature (ranging from 400 to 450°C) and *V:III* ratio (ranging from 10 to 250) on the morphology of the GaP nanowires via the hybrid growth method, which arise from changes in growth kinetics and mass flow, respectively. An exploration of the growth regime converged on an ideal growth temperature of 425°C based on the kinetics of this system, and demonstrated that the *V:III* ratio is a powerful handle for controlling the nanowire taper. Morphology control is crucial for the fabrication of the structures with optimized light absorption, predicted in Section 4.3.

#### *4.4.1.1 MOCVD Growth Methods*

A detailed discussion of basic MOCVD is beyond the scope of this thesis; Stringfellow's *Organometallic Vapor-Phase Epitaxy* is a good reference book.[98] Three common metalorganic chemical vapor deposition (MOCVD) growth methods exist for vertically aligned semiconductor nanowires: metal-catalyzed, self-catalyzed, and selective area growth. The first of these, metal-catalyzed growth, has the widest growth regime (*T*, *P*, *V:III* ratio), the greatest variety of growth substrates, and the lowest growth temperatures due to the strong catalytic driving force. Depending on the catalyst deposition method, the resulting arrays are either random or periodic with controlled wire radii. Gold-catalyzed InP, GaP and InGaP nanowire arrays have been demonstrated.[62,99,100] Gold is the most common catalyst for this method and its incorporation into the nanowires during growth forms deep level traps, which degrade the electronic quality of the nanowires, making this a non-ideal growth method for photovoltaic and photoelectrochemical

applications. The second method, self-catalyzed growth, averts the issue of deep level trap states, while still having many of the advantages of the catalytic method (low temperature, large growth regime). The catalyst particles consist of the group III metal of the desired material and are nucleated *in-situ*. This *in-situ* nucleation simplifies the sample preparation, but also results in only random arrays and minimal control on nanowire diameter. Self-catalyzed GaP and InP nanowire arrays have been demonstrated,[101,102] but the ternary compound, GaInP, has only been incorporated as a conformal layer around a GaP core.[103] The third nanowire growth method, selective area growth, which was used to fabricate the GaAs nanowire arrays discussed in Section 4.1, uses a pre-patterned dielectric mask and relies on selective growth only on exposed areas of the substrate. This method enables the greatest degree of control over nanowire dimensions and spacing, but the growth regime is small and the growth temperatures are high. Additionally, this growth method requires an energetically preferred crystal growth direction, which may not exist for all materials. Selective area growth has been demonstrated for GaAs (see Section 4.1) and InP.[104,105]

Based on these aspects of the three growth methods, selective area growth is the most desirable method for the fabrication of the optimized structures due to the precise control over nanowire position and diameter afforded, and the high electronic quality achievable. Nevertheless, as is discussed in the next section, the growth regime for GaP nanowires was not discovered and the nanowire arrays presented used a hybrid self-catalyzed and selective area growth method.

#### *4.4.1.2 Pattern Design*

The ultimate goal for the MOCVD growth efforts on GaP nanowire arrays discussed herein is to obtain $In_{0.61}Ga_{0.39}P$ nanowire arrays. Vergard's law predicts that this is the composition that results in the desired 1.8 eV bandgap for a tandem partner with Si.[106] The patterns used in the GaP

growths discussed in the following sections were designed to maximize light absorption in the $In_{0.61}Ga_{0.39}P$ nanowire arrays. Both analytic calculations from Equation (36) and full-wave electromagnetic simulations in Lumerical FDTD determined the selected pattern dimensions. These calculations required the complex refractive index data, which was generated using a linear interpolation between existing InP (Palik data built in to Lumerical FDTD) and $In_{0.49}Ga_{0.51}P$ (data built in to Sentaurus), and setting the imaginary part of the refractive index to zero beyond the band edge. The justification for a linear interpolation is twofold – (i) the discrepancy between InP and $In_{0.49}Ga_{0.51}P$ and InP refractive index data is small (<10%) and the desired composition is quite close to $In_{049}Ga_{0.51}P$, and (ii) lack of existing experimental or theoretical data for guidance otherwise necessitates it. Therefore, this approximation is sufficient for initial calculations and can later be modified when experimental data is available. Analytic calculations from the leaky mode eigenvalue equation indicated that a nanowire radius between 55 and 65 nm places the $HE_{11}$ mode within 150 nm of the band edge and a nanowire radius between 130 and 155 nm places the $HE_{12}$ mode within 150 nm of the band edge, which is the region in greatest need of an absorption enhancement. To select a specific radius, Lumerical FDTD simulations were run for 5% fill fraction nanowire arrays with radii of 55, 60, and 130 nm and Figure 40 displays the resulting absorption spectra. When weighted with the AM1.5G spectrum, these spectra correspond to 15.4 $mA \cdot cm^{-2}$ ($r$=55 nm), 15.8 $mA \cdot cm^{-2}$ ($r$=60 nm), and 10.2 $mA \cdot cm^{-2}$ ($r$=130 nm). The 130 nm radii nanowire array severely underperforms in comparison to the other two because the coupling efficiency into the higher order mode, $HE_{12}$, is lower than that of the $HE_{11}$ mode, which manifests as a sharper resonance peak and less broadband enhancement. Of the two nanowire radii (55 and 60 nm) designed to achieve absorption enhancements via the lower order $HE_{11}$ mode, the nanowire array with 60 nm radii outperforms that with 55 nm radii because its resonant absorption enhancement occurs closer to the band edge where the AM1.5G power density is

higher and the intrinsic material absorption is lower than at shorter wavelengths. Therefore, the patterned radius dimension was chosen to be 60 nm, with nanowires spaced 500 nm apart.

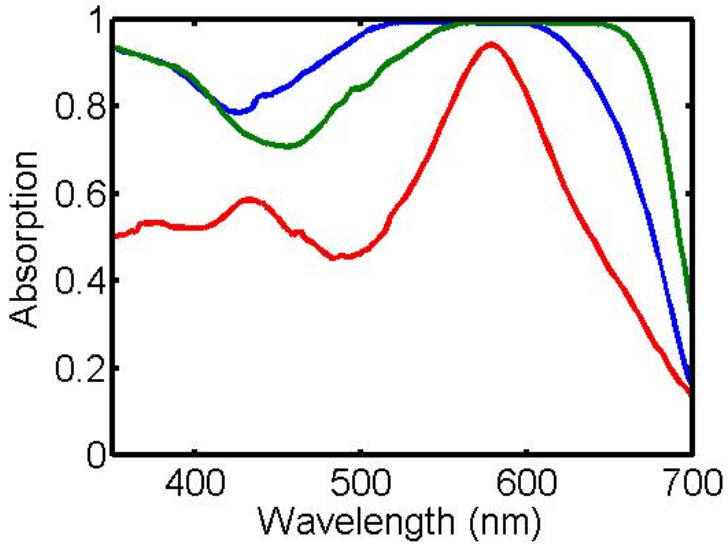


**Figure 40: Absorption vs. wavelength for 5% fill fraction arrays of $In_{0.61}Ga_{0.39}P$ nanowires with radii of 55 nm (blue), 60 nm (green), and 130 nm (red).**

### *4.4.1.2 Sample Preparation*

Mask fabrication was carried out with the help of Dr. James S. Fakonas and Colton R. Bukowsky. Prior to deposition of the nitride mask, the 6" silicon (111) wafer ($\rho$<0.01 Ω-cm, phosphorous doped, single side polished, 0.5°miscut, University Wafers) was dipped in buffered hydrofluoric acid (BHF) for 10 s to strip the native oxide, rinsed in DI water, and dried with a $N_2$ gun. The wafer was then immediately loaded into the plasma-enhanced chemical vapor deposition (PECVD) chamber for nitride deposition. A thin layer, approximately 30 nm, of $SiN_x$ was deposited via PECVD at 350°C with 400 sccm silane/argon mixture, 30 sccm $NH_3$, and 20 W RF power. To prepare the wafer for an electron beam lithography direct write for pattern creation, the wafer was pre-baked for 2 min at 180°C to remove any residual moisture and then 950PMMA A4 was spun on at

3000 rpm. Using a Vistec EBPG 5000+, the 500 x 500 μm square arrays of the specified pattern were written at 100 keV, using a 2 nA beam and a 1600 $\mu C \cdot cm^{-2}$ dose. The patterns were developed in a 1:3 MIBK:IPA solution for 45 s. To transfer the patterns into the nitride mask, the wafer was etched for 30 s in an Oxford ICP 380 ICP-RIE, using a pseudo-Bosch etch (38 sccm $SF_6$, 52 sccm $C_4F_8$, 23 W forward power, 1000 W ICP power, 10 mTorr). The remaining resist was stripped with dichloromethane. The wafer was finally scribed and diced into $1cm^2$ die, each containing a pattern, using a Dynatex scriber-breaker. Immediately prior to growth, the patterned die underwent a 5 second dip in buffered HF to remove the native oxide layer from the Si and was dried with a $N_2$ gun. The first three steps in Figure 41 illustrate the process flow for the sample preparation described above.

#### *4.4.1.3 MOCVD Growth of GaP Nanowire Arrays*

MOCVD growth of GaP was carried out in a Thomas Swann vertical close-coupled showerhead reactor under 8 slm $H_2$ ambient and 76 torr, using tertiarybutylphosphine (TBP) and triethylgallium (TEG) as the group V and group III precursor molecules, respectively. Substrate temperature was monitored via a pyrometer and a thermocouple placed directly below the substrate holder. Samples were rotated at 25 rpm throughout the growth.

For the selective area growths, samples were loaded into the reactor and brought to the desired growth temperature (550-650°C). After the sample and chamber reached thermal equilibrium, TBP and TEG were introduced simultaneously at *V:III* ratios ranging from 20 to 100. Following growth, samples were annealed at the growth temperature for 2 min and then allowed to cool back to room temperature.

For hybrid selective area and self-catalyzed growths, samples were loaded into the reactor and annealed at 700°C for 5 min under $H_2$. The substrate temperature was lowered to 500°C and Ga

droplets were nucleated into the patterned holes by flowing 32 µmol·min$^{-1}$ for 2 min. The substrate temperature was lowered again to either 400, 425 or 450°C for the 20 min growth step. During growth, TBP and TEG were flowed simultaneously; flow rates were adjusted to achieve *V:III* ratios of 10, 50, and 250 and are summarized in Table I. Following the growth step, the samples were annealed under TBP for 2 min at the growth temperature and under identical TBP flow as in the growth step. Figure 41 illustrates the complete nanowire array fabrication process flow.

**Figure 41: Process flow for hybrid selective area and self-catalytic MOCVD growth method for GaP nanowire arrays, starting with a silicon wafer, depositing a $SiN_x$ mask layer via PECVD, patterning the mask layer using e-beam and a pseudo-Bosch RIE etch, nucleating Ga droplets *in situ*, and finally, growing the nanowires.**

**Table 5: TBP and TEG flow rates for a given *V:III* ratio used in the hybrid growth method.**

| V:III Ratio | TBP Flow Rate (µmol-min$^{-1}$) | TEG Flow Rate (µmol-min$^{-1}$) |
|---|---|---|
| 10 | 800 | 32 |
| 50 | 1600 | 32 |
| 250 | 4000 | 16 |

#### *4.4.1.4 Characterization of GaP Nanowire Arrays*

Scanning electron microscopy (SEM) was used to observe the morphology of the resultant GaP nanowire arrays. Transmission electron microscopy (TEM) was used to characterize the crystal structure and quality of the as-grown nanowires. TEM was done by Dr. Shaul Aloni at the Molecular Foundry.

#### *4.4.1.5 Analysis of GaP Nanowire Arrays*

As previously mentioned, the attempts at selective area growth method were unsuccessful for growth of GaP nanowire arrays. Figure 42 shows two exemplary images of selective area growth attempts. Figure 42(a) displays a 30° tilt image of a growth attempt at high temperature (650°C) and high *V:III* ratio (100). This growth is selective, but has no preferred growth direction, as indicated by the low aspect ratio structures and the lack of a dominant cross sectional shape, meaning there is no dominant axial growth direction. Figure 42(b) displays a top-down image of a selective area growth attempt at low temperature (550°C) and low *V:III* ratio (20). These conditions result in no selective growth, and a conformal thin film growth proceeds. These results indicate that a selective area growth regime is either extremely small or non-existent for GaP.

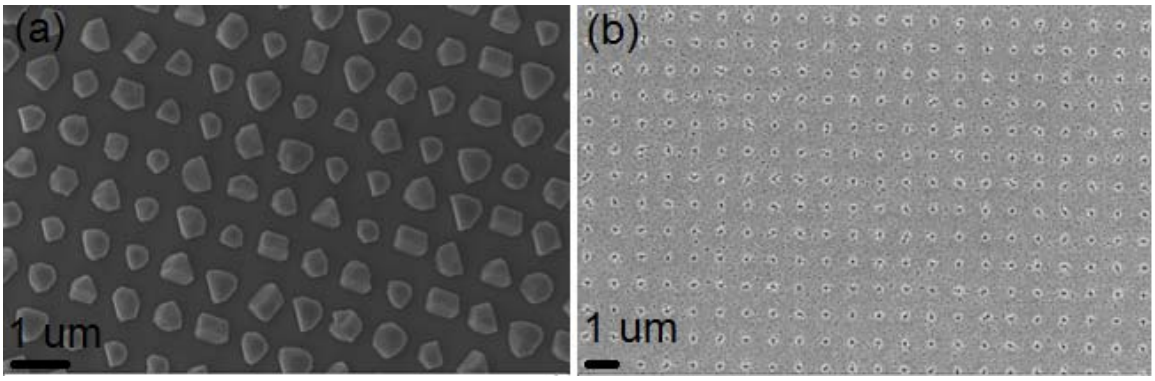


**Figure 42: Scanning electron micrographs of selective area growth attempts; (a) *T*=650°C, *V:III*=100 at a 30° tilt, (b) *T*=550°C, *V:III*=20.**

The hybrid selective area, self-catalyzed growth method resulted in periodic arrays of vertically-oriented GaP nanowires for a wide range of growth conditions. This section studies the effect of varying the growth temperature and *V:III* ratio on nanowire morphology.

Figure 43 displays the effect of varying the growth temperature from 400°C (a) to 425°C (b) to 450°C (c), at a constant *V:III* ratio of 50. The array grown at 400°C (a) consists of strongly tapered nanowires, starting with base radii matching that of the pattern (*d*=120 nm) and tapering essentially to a pointed top, with no trace of the gallium droplet remaining. This shape indicates a gallium-limited growth, in which the nanowire radius decreases upon vertical growth due to the consumption, and subsequent size reduction, of the nucleated gallium droplet. The growth halts upon complete consumption of the gallium droplet. The array grown at 425°C (b) consists of nanowires with only a very slight taper (*d*=120 nm) and an arrowhead-shaped tip. The TEG source molecule is more readily pyrolyzed at 425°C, thereby increasing the gallium supply in comparison to the 400°C growth, and preventing the gallium droplet from being consumed during growth. The arrowhead shaped tip is the result of the post-growth anneal under TBP, which quickly consumes the remainder of the gallium droplet. The array grown at 450°C (c) consists of tapered nanopillars, which are much wider than the patterned radius. This morphology indicates that higher growth temperatures enable un-catalyzed growth on the side facets.

These results indicate that the growth of self-catalyzed vertical GaP nanowires occurs in only a small temperature window around 425°C where it is kinetically favorable. At low temperature, limited pyrolysis of TEG results in the consumption of the gallium droplet during growth. At high temperature, un-catalyzed growth occurs on the side walls.

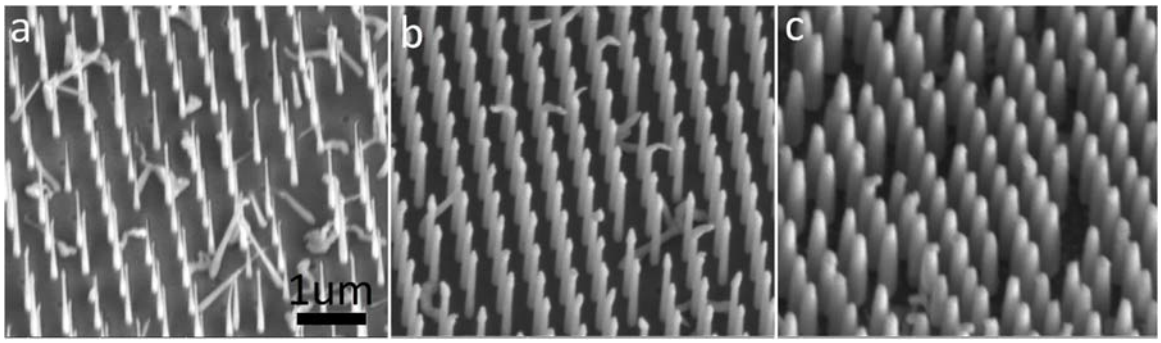


**Figure 43: Scanning electron microscopy images of self-catalyzed GaP nanowire arrays on Si substrates grown at a *V:III* ratio of 50 and a growth temperature of (a) 400°C, (b) 425°C, and (c) 450°C.**

Figure 44 displays the effect of varying the *V:III* ratio from 10 (a) to 50 (b) to 250 (c), at a constant temperature of 425°C. The array grown at a *V:III* ratio of 10 (a) consists of untapered nanowires with a circular tip. The untapered sides of these nanowires and the circular tip both reveal that the gallium droplet was not consumed during the growth step and, therefore, the growth is not gallium-limited. The larger gallium supply is a direct result of the lower *V:III* ratio (10 in comparison to 50). Figure 44(b) is identical to Figure 43(b) and displays the array grown at a *V:III* ratio of 50 (b) and consists of slightly tapered nanowires. This small taper indicates a slight undersupply of gallium during growth due to the higher *V:III* ratio. The gallium droplet is partially consumed during the growth step, which results in the arrowhead shaped tip, as previously discussed. The array grown at a *V:III* ratio of 250 (c) consists of strongly tapered nanowires, which have base radii matching that of the pattern (*d*=120 nm) and taper to a pointed tip. The increase in *V:III* ratio results in a strongly gallium-limited growth, causing the gallium droplet to be consumed during the growth step in a similar fashion to the low temperature growth. However, the proposed mechanism for gallium limitation for the case of low temperature and high *V:III* ratio is different. At low temperature, the undersupply of gallium is most likely due to kinetic limitations, namely

the limited pyrolysis of TEG. At high *V:III* ratios, the undersupply of gallium is due to the mass flow limitations, specifically the dominance of TBP molecules over TEG molecules at the growth site.

These results indicate that the *V:III* ratio is a useful handle for tuning the morphology of self-catalyzed GaP nanowires on Si. Low *V:III* ratios result in untapered nanowires. As *V:III* ratio increases, the degree of tapering also increases due to limited mass flow of TEG molecules to the growth site.

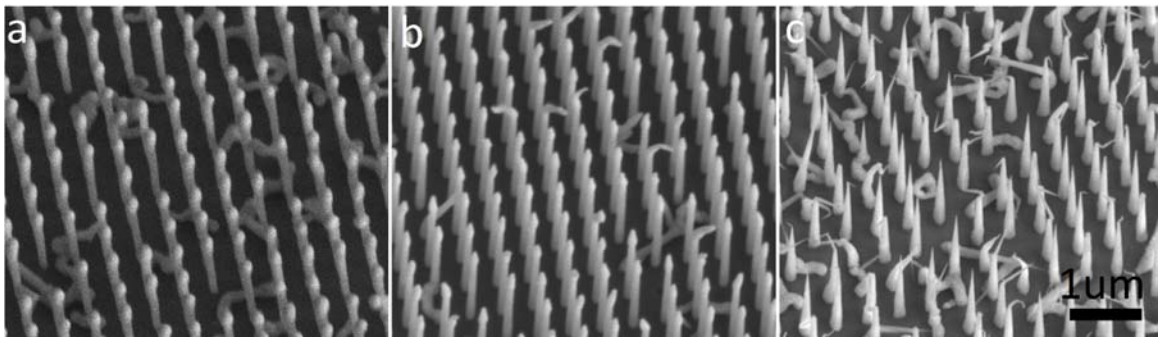


**Figure 44: Scanning electron microcopy images of self-catalyzed GaP nanowire arrays on Si substrates grown at 425°C and *V:III* ratios of (a) 10, (b) 50, and (c) 250.**

Figure 45 shows transmission electron micrographs of the nanowire array grown at 425°C and a *V:III* ratio of 50 (Figure 43b and Figure 44b). The nanowire crystal structure is zincblende, matching that of bulk gallium phosphide. The long cylindrical region of the nanowire is single crystalline, with multiple stacking faults, revealing that nanowire growth during the main growth step is high quality. The nanowire tip, likely the result of the TBP anneal, is polycrystalline. Additionally, a thin conformal surface layer (<1 nm) is visible, which is also likely the result of the TBP anneal.

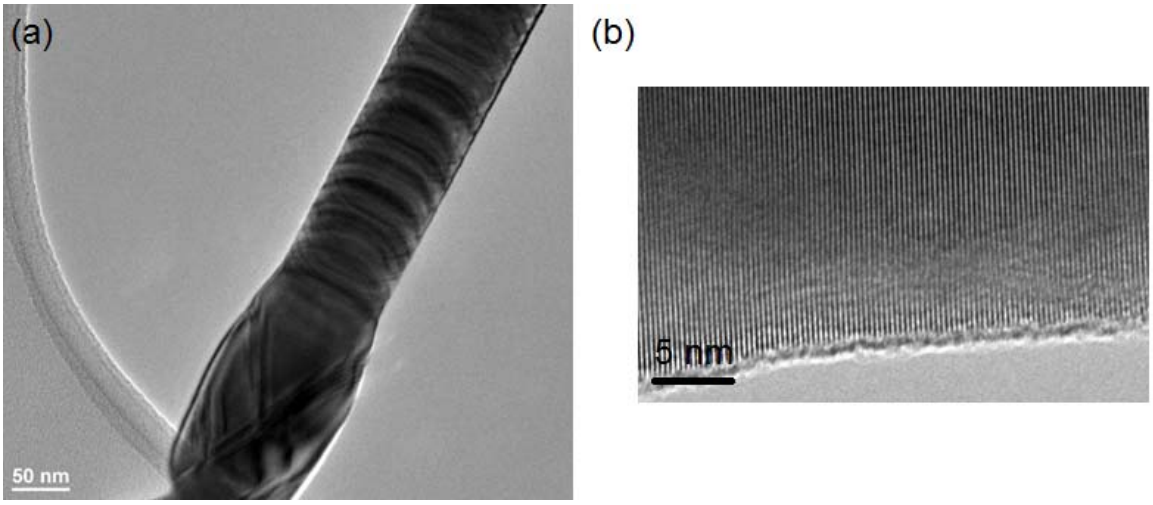


**Figure 45: Transmission electron microscopy images of a GaP nanowire grown at 425°C and a *V:III* ratio of 50.**

In conclusion, a hybrid growth method for vertically-oriented GaP nanowire arrays was developed, using TBP and TEG as precursor molecules. Additionally, the growth regime exploration led to an optimized growth temperature and established morphological control via variance of the *V:III* ratio. This morphological control is critical to fabrication of the optimized structures discussed in Section 4.3. However, as an indirect bandgap material, GaP suffers from low light absorption in comparison to the direct bandgap GaAs studied in Section 4.3. Therefore, further work is needed to obtain sparse nanowire arrays that can achieve near-unity absorption. Chapter 5 suggests further work towards this end.

### 4.4.2 RIE of InP Nanowire Arrays

This section presents a reactive-ion etching method of fabricating InP nanowire arrays from an InP wafer. Modification of the etch recipe and of the mask pattern resulted in arrays of tapered nanowires and multi-radii nanowires, respectively. Optical characterization of these arrays

validates the light absorption optimization discussed in Section 4.3, but electrical characterization shows significant lifetime degradation occurs during the etching process.

#### *4.4.2.1 Pattern Design*

The initial patterns were designed with the intention of demonstrating that tapered nanowires broaden the absorption peak, and that multiple radii in a single array generate multiple absorption peaks. Therefore, the nanowires were patterned to be 750 nm apart in a square lattice. The sparseness of these arrays results in more well-defined peak features, which is especially useful in distinguishing peaks of different radii wires within a single array that might otherwise become one extended peak due to experimental variation in the fabricated dimensions. Based on the leaky mode eigenvalue equation, Equation (36), and the complex refractive index of InP, varying the radii of the InP nanowires between 60 and 90 nm translates to the $HE_{11}$ resonant wavelength spanning from 500 to 900 nm. Fabricated patterns included uniform arrays of 60, 70, 80, and 90 nm and a multi-radii array consisting of 60 and 90 nm radii.

#### *4.4.2.2 Sample Fabrication*

The general process described in this section was adapted from a similar procedure for fabrication of InP grating structures developed by Dr. Ryan Briggs. Based on his observations, an e-beam resist is an insufficient mask for etching multiple microns into InP at elevated temperatures, and therefore, this process requires a two-step etching process, involving a thick $SiO_x$ hard mask. This two-step etch process is detailed below.

A 2'' InP wafer (AXT, n-type, Sulfur doped, (100) orientation) was sonicated for 10 min in water, IPA, acetone, and water. The typical piranha clean step for InP was omitted because the existence of the native $InP_xO_Y$ facilitated adhesion of the $SiO_x$ mask layer. For deposition of the hard mask, a 440 nm layer of $SiO_x$ was sputtered onto the InP wafer from a $SiO_2$ target at 200 W forward

power, and in an Ar atmosphere (20 sccm) at 3 mTorr for 460 min. The $SiO_x$ thickness was determined using a Filmetrics F40, a thin film measurement tool. To prepare the wafer for an electron beam lithography direct write for pattern creation, the wafer was pre-baked for 2 min at 180°C to remove any residual moisture and then MaN-2403, a negative tone resist, was spun on at 4000 rpm. The resist was then baked on a hot plate at 90°C for 1 min. Using a Vistec EBPG 5000+, the 2 x 2 mm square arrays of the patterns specified in the previous section were written at 100 keV, using a 5 nA beam and a 285 $\mu C \cdot cm^{-2}$ dose. This pattern size was chosen based on the spot size of the integrating sphere used for optical characterization (see Section 4.4.2.5). Following the e-beam write, the patterns were developed in MF-319 for 45 s, rinsed in DI water for 1 min, and dried under $N_2$. To enable the fabrication of arrays with morphologically different nanowires, the wafer was scribed and diced into 7.5 x 7.5 mm chips, using a Dynatex scriber-breaker. A pseudo-Bosch etch (5 mTorr, 1000 W ICP forward power, 25 W RF forward power, 10°C, 26 sccm $SF_6$, 35 sccm $C_4F_8$) was used to transfer the patterns into the oxide mask, using an Oxford ICP 100 ICP-RIE. Due to an observed high degree of etch rate fluctuation, the etch rate was always calibrated immediately before etching the wafer because precision on this etch step was critical. Necessary etch times ranged from 10 to 15 min. Additionally, due to the small size of the chips, particular care was taken to add only a minute amount of Fomblin oil when attaching the chips to the sacrificial wafer in the etch chamber to prevent its interference with the etch chemistry. Following the pseudo-Bosch etch, any remaining resist was stripped in a 30 s $O_2$ etch (80 sccm $O_2$, 15°C, 2000 ICP forward power, 40 RF forward power, 12 mTorr).

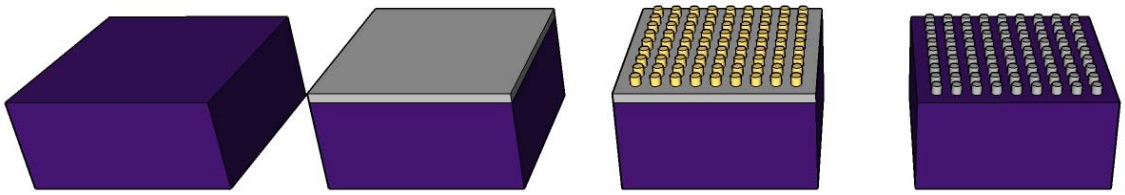

**Figure 46: Sample preparation for RIE of InP nanowire arrays, starting with an InP wafer (purple); sputtering a hard mask layer of $SiO_x$; spinning on MaN-2403 resist (yellow), doing a direct e-beam write, and developing the pattern; transferring the pattern into the hard mask with a pseudo-Bosch etch.**

A detailed discussion of RIE is beyond the scope of this thesis; a detailed explanation and discussion of RIE, specifically for silicon, is covered in Michael David Henry's thesis *ICP Etching of Silicon for Micro and Nanoscale Devices*.[107] A $Cl_2/H_2/CH_4$ etch was used for the InP nanowire etch step.[108,109,110] In this etch, $Cl_2$ is the primary chemical etchant, forming $InCl_3$, and $H_2$ serves a ballistic etchant. $InCl_3$ is non-volatile at room temperature; therefore, this etch is carried out at high temperature (200-300°C). The $CH_4$ is the sidewall passivation species, similar to the $C_4F_8$ species in a pseudo-Bosch etch. Etch parameter sweeps identified the $CH_4$ flow as the critical parameter for control of the sidewall taper, with low $CH_4$ flow resulting in taper and high $CH_4$ flow resulting in inverse taper. The etch was carried out at 4 mTorr chamber pressure, 2200 W ICP forward power, 200 W RF forward power, 28 sccm $H_2$, and 32 sccm $Cl_2$, and the $CH_4$ flow was varied between 24 and 30 sccm. The table temperature was set to 60°C and no Fomblin oil was used to contact the chips to reduce thermal contact and establish a high temperature etch.

For absorption measurements, it is necessary to exfoliate the nanowire arrays from the substrate. To achieve this, a 10:1 polymer base:curing agent PDMS solution was made and dropped onto the InP chips, which were placed in a Petri dish covered in aluminum foil. The chips coated in PDMS

were degassed for 10 min in a vacuum chamber, and then the remainder of the PDMS solution was poured into the Petri dish and degassed again for 20 min. Pouring the PDMS into the Petri dish resulted in a nice flat PDMS surface, which is critical for the optical measurements. The Petri dish with chips and PDMS was then placed in an oven at 80°C and cured overnight. After removing the Petri dish from the oven, the PDMS disk was removed from the Petri dish and the aluminum foil was peeled away. The PDMS disk was allowed to cool to room temperature (~5 min) and then the chips were mechanically removed from the PDMS using tweezers, leaving the wire arrays embedded in the PDMS. Figure 47 displays a simplified process flow for the fabrication procedure described above.

**Figure 47: Fabrication process for InP nanowire arrays, starting with an InP wafer (purple); sputtering a hard mask layer of $SiO_x$; spinning on MaN-2403 resist (yellow), doing a direct e-beam write, and developing the pattern; transferring the pattern into the hard mask with a pseudo-Bosch etch; performing a $Cl_2/H_2/CH_4$ etch to get InP nanowires; embedding the nanowire arrays in PDMS and removing them from the InP substrate.**

Figure 48 shows images of the peeled-off arrays embedded in PDMS, where (a) is a normal photograph of the arrays and (b) and (c) are 5X microscope images. These images illustrate the large scale uniformity of the peeled-off arrays. The off-centered cross in the microscope images is an artifact from the e-beam write, where the patterned sizes are slightly larger than the rest of the patterned area, which manifest as color variations. The next section presents scanning electron micrographs (SEM images) of the arrays prior to peel off.

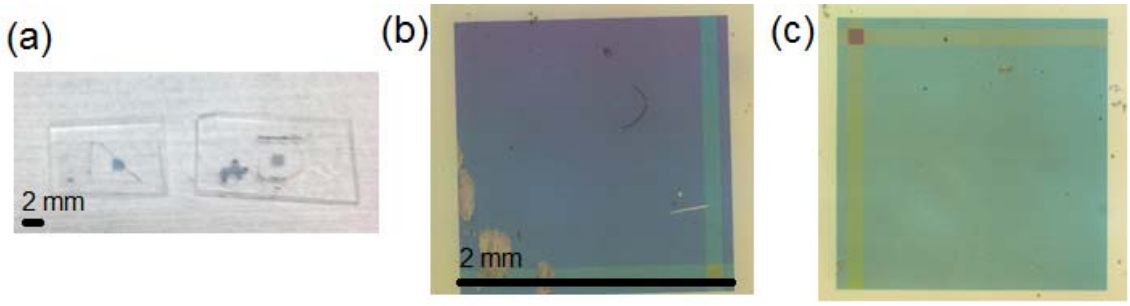


**Figure 48: Peeled-off arrays; (a) photograph of two arrays embedded in PDMS; (b,c) 5X microscope images of the patterned area of the same two arrays.**

### *4.4.2.5 Characterization of InP Nanowire Arrays*

Arrays of InP nanowires with varying morphology were fabricated and optically characterized using a homemade integrating sphere setup, which measures wavelength-dependent transmission and reflection. Details on this setup can be found in M. Kelzenberg's thesis.[31] Figure 49 displays a complete set of optical data, including experimental measurements and simulation results, for a nearly uniform array of InP nanowire arrays. This array was patterned to have 90 nm radii nanowires spaced 750 nm apart and was etched with 26 sccm of $CH_4$. An SEM image of this array is shown in Figure 50(a); the wires are approximately 1.7 μm tall, including the remnants of the $SiO_x$ mask, and have 90 nm radii, corresponding to an equivalent planar thickness of approximately 75 nm. SEM images determined the nanowire dimensions used in the simulations. Analysis of the SEM images consisted of extracting three representative wire shapes to simulate, each of which was broken up into two sections with different degrees of taper and a $SiO_x$ cap. Figure 49(c) and (d) display the absorption results, with the three representative shapes represented by the thin, dashed, and dotted lines and their average represented by the thick line. Figure 49(b) and (d) show the reflection spectra for this array on substrate (blue), embedded in PDMS and on substrate (green), and peeled-off (red) from experiment and simulation,

respectively. All three of these configurations exhibit low reflection (<20%), despite having a fill fraction below 5%. This low reflection is a product of the strong coupling into leaky waveguide modes of the nanowires. Figure 49(a) and (c) display the absorption, transmission, and reflection spectra for the peeled-off array from experiment and simulation, respectively. The absorption spectrum reveals a strong resonant absorption peak at approximately 850 nm, corresponding to the $HE_{11}$ mode of the nanowires. The majority of the absorption losses are in transmission, due to the short wire length and large spacing between wires.

Additionally, it is important to note that all curves exhibit fairly close matching between experiment and simulation. The good agreement between experiment and simulation establishes confidence in both the experimental and simulation techniques, which is a crucial step before tackling the more complex tapered and multi-radii cases.

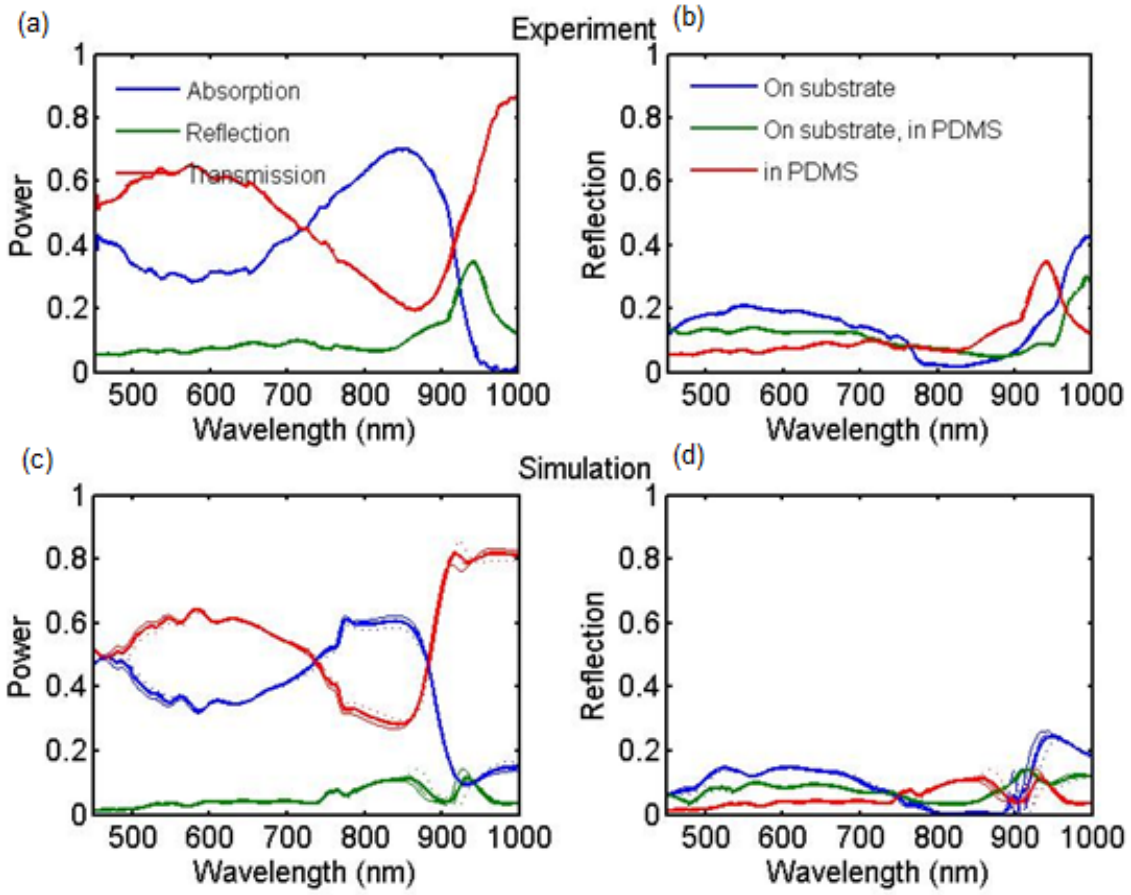


**Figure 49: Experimental (a,b) and simulation (c,d) optical data for an InP nanowire array patterned to have 90 nm radii wires and etched with 26 sccm $CH_4$, pictured in Figure 50(a); (a,c) reflection spectra for the wire array on substrate (blue), on substrate and embedded in PDMS (green), and peeled off the substrate (red); (b,d) absorption (blue), transmission (green), and reflection (red) spectra of the peeled-off array.**

In addition to uniform arrays, tapered nanowire arrays and multi-radii nanowire arrays were fabricated. The multi-radii nanowire arrays resulted from modified pattern dimensions; Figure 50(c) shows an array fabricated from a mask of alternating 60 and 90 nm radii, spaced 750 nm apart and etched with 26 sccm of $CH_4$. Tapered nanowire arrays were attained by modifying the

$CH_4$ flow during the InP RIE step. Figure 50(b) displays an inverse tapered nanowire array; the inverse taper was achieved by increasing the $CH_4$ flow from 26 to 30 sccm.

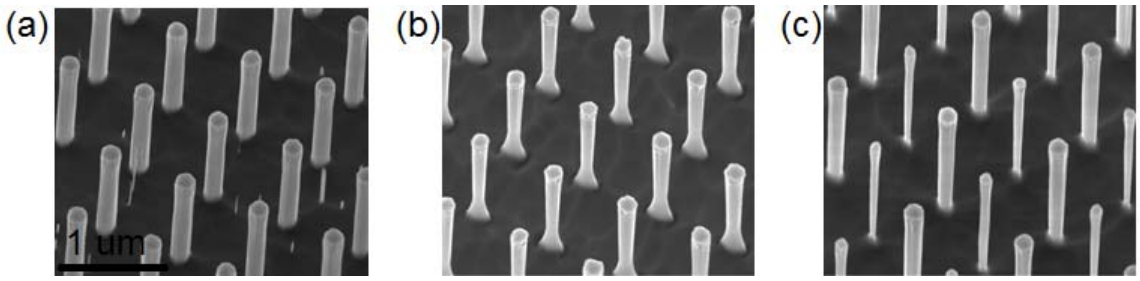


**Figure 50: SEM images at 30° tilt of (a) uniform radii array with 90 nm radii, etched at 26 sccm $CH_4$, (b) inverse taper array with 90 nm top radii, etched at 30 sccm $CH_4$, (c) multi-radii array with 60 nm and 90 nm radii, etched at 26 sccm $CH_4$.**

Figure 51 displays the experimental and simulated absorption spectra for these arrays embedded in PDMS and peeled off from the substrate; experimental data was measured using the integrating sphere and simulated data was determined using the same methods as were used for the uniform array discussed above. Simulation of the inverse tapered array assumed that the peel off resulted in a fracture of the wire at the small point in the radius. The spectrum for the tapered nanowire array (green line) exhibits a broadened absorption peak in comparison to that of the uniform nanowire array (blue line). The spectrum for the multi-radii nanowire array (red line) exhibits two peaks, corresponding to the $HE_{11}$ resonances of the different nanowire radii. Simulated and experimental results qualitatively match. By design, these arrays do not achieve near-unity absorption. The uniform, tapered and multi-radii nanowire arrays have fill fractions (planar equivalent thicknesses) of 4.5% (71 nm), 2.7% (29 nm), and 2.1% (33 nm). Image analysis specified the fill fractions and equivalent thicknesses, using the same three representative wire shapes as described above for the uniform array simulation results. The fill fractions and, in particular, the

planar equivalent thicknesses for these arrays are significantly less than those of the optimized arrays in Section 4.3—5% and 150 nm. This discrepancy, which is particularly large for the multi-radii nanowire array, explains the lower absorption fractions observed in these arrays.

Due to experimentally introduced variability in array dimensions from the etching procedure, the multiple peaks in multi-radii nanowire arrays and peak broadening in tapered nanowire arrays designed to achieve near-unity absorption could be difficult to distinguish. By fabricating extremely sparse arrays, these features are easy to identify, which motivates the use of sparse arrays herein for proof of principle. The minimal amount of InP material used in these arrays translates to easily identifiable features, as seen in Figure 51. Most importantly, these results confirm the principles governing the simulation-based optimization of Section 4.3 and indicate that sparse arrays of tapered nanowires or sparse multi-radii nanowire arrays can achieve near-unity absorption. Chapter 5 discusses further fabrication efforts needed to demonstrate near-unity absorption in sparse arrays.

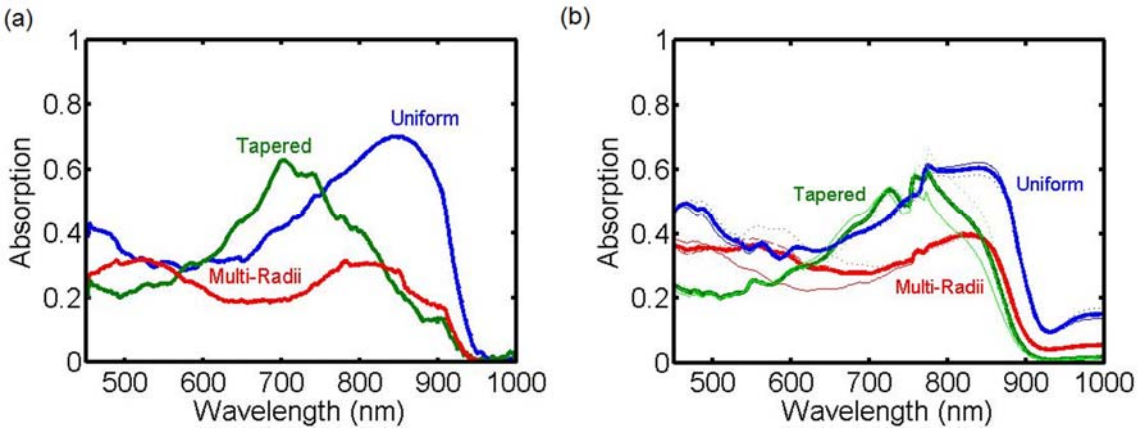


**Figure 51: Experimental (a) and simulated (b) absorption spectra for the three nanowire arrays shown in Figure 50, where the uniform array (a) is in blue, the tapered array (b) is in green, and the multi-radii array (c) is in red.**

Electrical characterization in the form of time-resolved photoluminescence (trPL) measurements was also conducted to study the lifetime properties of the etched nanowire arrays. The trPL measurements were conducted by Dr. Dennis Friedrich. The trPL measurements used the arrays embedded in PDMS and peeled off from the substrate to ensure that all measured PL signal was from the wire arrays and not from the substrate. For comparison, transient PL measurements were also done on a clean InP wafer and an InP wafer that went through the entire etch process. TrPL spectra were collected by illuminating the samples with the second harmonic of the signal (SHS) output at 660 nm of an optical parametric amplifier (Coherent OPerA Solo) pumped by a Ti-sapphire based regenerative amplifier (Coherent Libra) at a wavelength of 800 nm and pump power of 4.5 W at 10 kHz with pulselengths of 100 fs. The OPA excitation output was attenuated by neutral density filters to a typical power of 50 µW at 660 nm. The luminescence from the samples was collimated and focused onto the entrance slit of a spectrometer (Princeton Instruments Acton SP2300) set to a center wavelength of 850 nm and further detected by a streak camera (Hamamatsu C10910-01). For trPL measurements on InP wafers and InP nanowires, a long-pass filter with a cut-off wavelength of 750 nm and 700 nm, respectively, was placed before the spectrometer to eliminate scattered laser radiation. A temporal resolution of approximately 1 ps was achieved while sweep ranges were adjusted to match the observed decay times and set to 50 ns and 200 ps for InP wafers and InP nanowires, respectively.

Figure 52 displays the transient photoluminescence data from a clean InP wafer (a), an InP wafer that underwent the etching process (b), and two representative nanowire arrays (c,d). Note that the wavelength range is identical for all plots, but that the time range for the nanowire arrays is much shorter than that of the wafers. These images show that the clean wafer has the most intense photoluminescence, as expected, and that the nanowire arrays have the least intense

photoluminescence. The photoluminescence intensity from the nanowire array in (d) is lower than that of the nanowire array in (c) likely because the filling fraction of the array was much less. The peak intensity wavelength also blue-shifts from 910 nm for the clean wafer to 900 nm for the etched wafer to 850 and 860 nm for the two representative nanowire array samples. It is clear that it arises from the etching process and is more prominent in wire samples than planar samples. The Bohr radius in InP is around 20 nm, therefore bandgap widening due to quantum confinement is insignificant at nanowire radii of 60 nm and greater;[111,112] therefore, these nanowires are too large for the blue-shift in photoluminescence to be attributed to quantum confinement. Previous reports on photoluminescence of InP nanowires grown via MOCVD have shown similar blue-shifts in nanowire photoluminescence and have demonstrated that the nanowires are in the wurtzite crystal phase, which has a bandgap of 1.42 eV, rather than the bulk zincblende crystal phase, which has a bandgap of 1.34 eV.[68,112] The formation of the wurtzite crystal phase over the zincblende crystal phase in InP nanowire growth has been shown to be dependent on nanowire diameter, growth temperature, among other parameters.[113] A phase transformation during reactive ion etching is unprecedented, but not out of the realm of possibility. Based on the absorption results which show absorption through 925 nm (the typical band edge of InP), any phase change is likely only a surface phenomenon. An alternative explanation is that the InP is becoming degenerately doped during the etching procedure, resulting in a blue-shift in the photoluminescence due to the Burstein-Moss shift. This phenomenon was previously reported in InP nanowires coated with aluminum oxide, establishing an interface charge that repelled free charge into the nanowire core.[114] Similar effects could be present in the etched nanowire arrays discussed herein, due to the formation of an indium, indium oxide, or indium phosphate surface layer during the etch process. Chapter 5 addresses further investigations towards understanding this phenomenon.

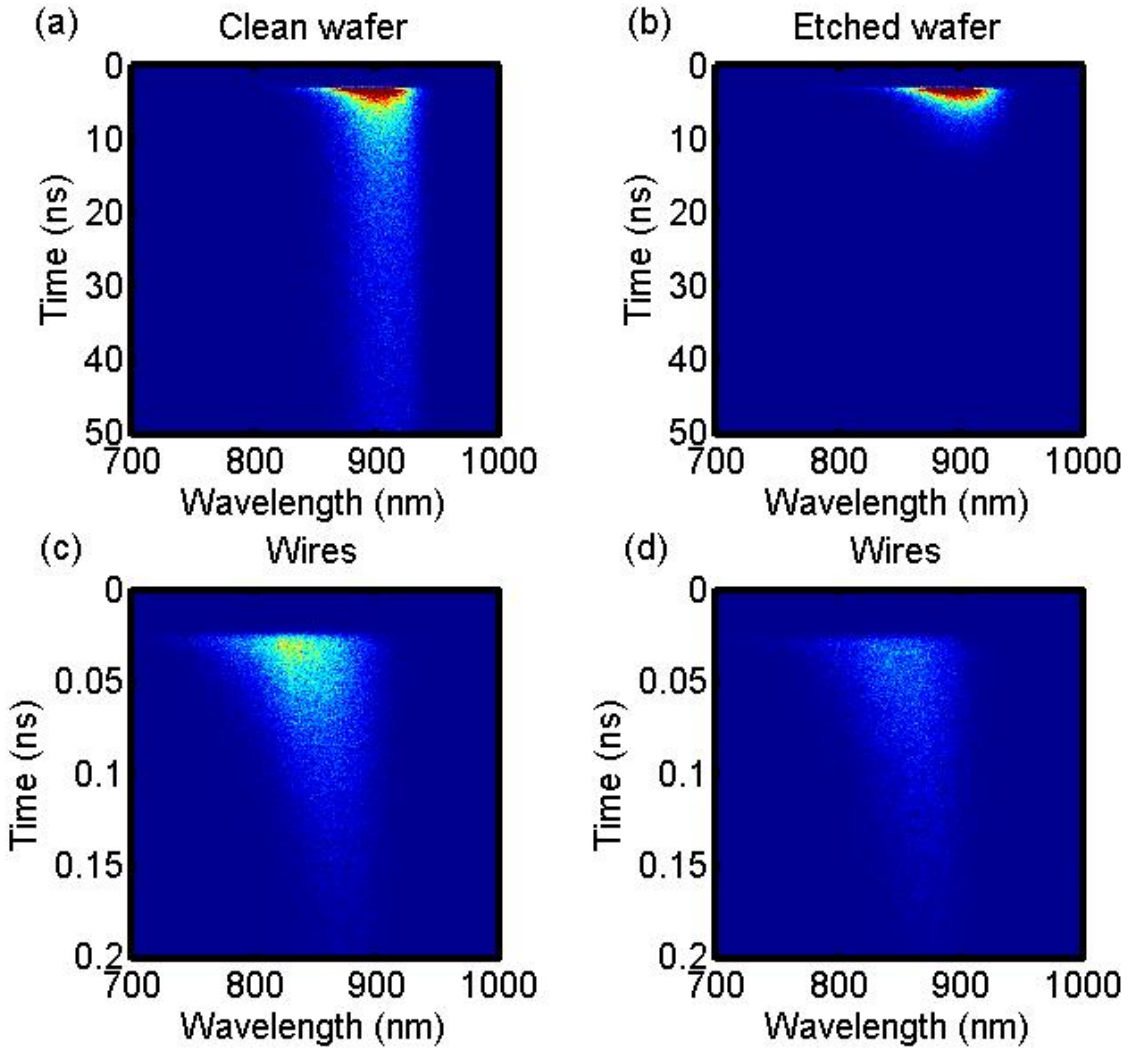


**Figure 52: Photoluminescence intensities as a function of wavelength and time for (a) a clean InP wafer, (b) an InP wafer that underwent the wire etching procedure, and (c,d) two representative InP nanowire arrays.**

The lifetimes of each sample were extracted from the transient photoluminescence data at the peak intensity wavelength. For the clean wafer, a two term exponential was used to fit the data, and indicated two lifetimes of 27 and 2 ns, presumably for the bulk and surface recombination lifetimes. Single term exponentials were used to fit the three other samples, and gave lifetimes of

2 ns for the etched wafer and 0.03 ns for the nanowire arrays. As evidenced by the two order of magnitude drop in the lifetime, the etch process does significant damage to the optoelectronic quality of the InP, indicating that these arrays are not suitable for photovoltaic or photoelectrochemical applications as is. Again, Chapter 5 addresses future research directions on passivation of the InP nanowires to potentially reverse the damage.

# Chapter V: Conclusions and Future Work

This thesis focused on the mesoscale optical and optoelectronic design of photovoltaic and photoelectrochemical devices. The work discussed herein demonstrated that simulation-based optical and optoelectronic modeling and optimizations of these devices can have strong predictive power for device efficiency and device efficiency improvements, and serve as a useful understanding tool and guide for experimental fabrication efforts. Specifically, an optoelectronic study of a tandem Si|$WO_3$ microwire photoelectrochemical device and an optical study of III-V nanowire arrays were conducted. The following sections present a summary of the key findings of each of these studies and suggest interesting future directions for this work.

## 5.1 Tandem Microwire-Based Photoelectrochemical Devices

Initial efforts focused on development and validation of an optoelectronic model for microwire-based tandem photoelectrochemical devices, using Si|$WO_3$ as a model system for a water-splitting device. Because the optoelectronic properties of $WO_3$ are not well-established in literature, the first step was validation of experimental and theoretical results for a planar $WO_3$|liquid junction. Coupling of Lumerical FDTD for optical simulations and Synopsys TCAD Sentaurus for charge carrier transport simulations led to the development of a coupled optoelectronic model with a good match between open circuit voltage and light-limited current density. The application of this model to a microwire-based $WO_3$|liquid junction achieved a good match between experiment and theory, validating the model. Extension of this model to the complete tandem Si|$WO_3$ system in planar and microwire configurations exhibited predictive power concerning which configurations and illumination conditions would produce enough voltage to split water.

Because the initial designs had low efficiency (<1%) both experimentally and theoretically, significant effort was invested in an optimization of the optoelectronic performance of this design. This optimization revealed that geometric design and contact material selection can significantly influence light absorption properties without compromising device IQE. Results demonstrated that opaque contacts between the silicon microwire and the $WO_3$ layer are not a realistic choice because they are a significant source of parasitic absorption due to strong coupling into surface plasmon-polariton modes along the metallic interface. The incorporation of a transparent contact layer, the use of a back reflector and an antireflective coating, and certain geometric modifications to the microwire structure shape were all shown to improve overall device efficiency. The predicted short circuit current density of the optimized microwire-based system was over 200% greater than both the planar equivalent tandem system and the original tandem microwire design. This result demonstrated two important points: (i) mesostructured designs can significantly outperform planar designs, and (ii) simulation-driven mesoscale design can play a critical role in efficient device design.

### 5.1.1 Future Work on Tandem Microwire-Based Photoelectrochemical Devices

Experimental fabrication of the optimized tandem microwire-based Si|$WO_3$ device designs would be of interest as further validation of the model and as a demonstration of the power of simulation-based mesoscale design. Incorporation of both cathodic and anodic catalysts into the design is also a critical next step for a free-standing, completely monolithic device. $IrO_x$ has been shown to improve the Faradaic efficiency of $WO_3$ from essentially 0% up to 100% for an opaque catalyst layer,[115] and cathodic catalysts such as Pt or NiMo will lower the overpotential for hydrogen production at the silicon interface, but these catalysts are a source of parasitic

absorption. Simulation-driven mesoscale design for catalyst placement has the potential to play a crucial role in maximizing devices integrated with catalysts.

The Si|$WO_3$ system itself may be of limited interest for future work because of inherent limits on its water-splitting efficiency due to the low Faradaic efficiency and wide bandgap of $WO_3$. That said, the model developed herein can be extended and applied to many related systems. For continued studies of water-splitting systems, the developed model could be applied to Si|$TiO_2$ and Si|$BiVO_4$ systems, or Si microwires combined with other photoanode materials as they are discovered. This developed model could also be extended to the study of $CO_2$ reduction devices. A microwire-based Si|GaP device structure would be of particular interest due to the reported selective production of methanol at the surface of GaP in the presence of pyridine.[97] The silicon microwires would provide additional voltage as well as serve as a scaffold for a high surface area GaP layer, which would improve the catalytic performance.

## 5.2 Nanowire-Based Photovoltaic and Photoelectrochemical Devices

Sparse arrays (<5% fill fraction) of vertically-oriented GaAs nanowire arrays were fabricated via selective area growth MOCVD. Their optical absorption and photoelectrochemical external quantum yields indicated high, yet strongly spectrally dependent light absorption, approaching near-unity absorption at certain resonant wavelengths. Optical simulations of these arrays, performed in Lumerical FDTD, resulted in good agreement with experimental results. Simulation tools and analytic calculations identified the source of these absorption enhancements as strong coupling into leaky waveguide modes, specifically the $HE_{11}$ and $HE_{12}$ modes at normal incidence.

A detailed understanding of the role of leaky waveguide modes in nanowire arrays and their connection to photonic crystal modes was developed in the context of silicon nanowires. Analogous to the tight-binding model for an electronic crystal, the leaky waveguide modes were

only slightly perturbed by the periodicity of the array in sparse arrays; therefore, these leaky waveguide modes were indeed photonic crystal modes, but closely resembled the leaky waveguide modes of individual wires. Additionally, mode symmetry explained the selective coupling, and the mode dispersions explained the slight red-shift of the $HE_{11}$ and $HE_{12}$ modes at normal incidence.

Knowledge of the leaky waveguide mode properties was employed to devise two strategies to achieve near-unity broadband absorption in sparse nanowire arrays: (i) introducing multiple wire radii within a small unit cell array to increase the number of resonant wavelengths, and (ii) tapering of nanowires to introduce a continuum of radii, thereby creating a corresponding continuum of resonant wavelengths. Both approaches resulted in improved broadband absorption, and the optimized arrays for both strategies achieved a greater than 15% absorption enhancement over the uniform array.

Experimental efforts towards fabrication of these optimized nanowire array structures were twofold: (i) bottom-up: MOCVD growth of GaP nanowires, and (ii) top-down: ICP-RIE of InP nanowire arrays. Selective area MOCVD growth of GaP nanowire arrays was unsuccessful, leading to the use of a hybrid growth method combining selective area growth and self-catalyzed growth. A parameter sweep using this hybrid growth method resulted in convergence on a growth temperature optimized to favor axial growth and a *V:III* ratio range that controlled nanowire morphology. High *V:III* ratios resulted in tapered nanowires, low *V:III* ratios resulted in inverse tapered nanowires, and a moderate *V:III* ratio of 50 gave rise to untapered nanowires. Using a $SiO_x$ mask, InP nanowire arrays were etched with a $H_2/Cl_2/CH_4$ chemistry using ICP-RIE. The $CH_4$ flow controlled the taper of the nanowires. Sparse arrays of uniform, tapered and multi-radii nanowire arrays were fabricated and their absorption spectra measured. The absorption spectra

validated the simulation-based optimization results that multiple radii in an array results in multiple absorption peaks and tapered arrays result in peak broadening. Electrical characterization of these arrays demonstrated that the etching process does significant damage to the InP and potentially induced a crystal phase change.

### 5.2.1 Future Work on Nanowire-Based Photovoltaic and Photoelectrochemical Devices

The theoretical work on nanowire arrays discussed herein addressed only the optical properties of bare nanowire arrays. In a complete photoelectrochemical device, the optical picture is likely to be much more complex. Because III-V materials are unstable under photoelectrochemical conditions and have poor catalytic properties, they will need a protective coating and a catalyst. Therefore, additional theoretical optical studies of interest include optical simulation of III-V nanowires with protective coatings and catalysts because both components could significantly alter the nanowire array optical properties. A study of III-V nanowires with $TiO_2$ protective coatings that examines the effect of the protective coating thickness would be of particular interest. At small thicknesses ($t$>>λ), the optical effect would likely be small, but significant thicknesses will likely result in significant alterations to the spectral position of the modes and the coupling efficiency into the modes. To illustrate the effect of changing background index on leaky mode properties, Figure 53 displays the absorption spectra for a 60 nm radius GaAs nanowire illuminated perpendicular to its wire axis in varying backgrounds ($n$=1, 1.6, 2.2, and $TiO_2$), along with the electric field intensity profile at the resonant wavelength of the $TM_{11}$ mode for each background ($\lambda$=638, 654, 669, and 686 nm, respectively). The shift in resonant wavelength is not dramatic, moving just 50 nm from a background of air, $n$=1, to a background of $TiO_2$, $n(\lambda_{res})$=2.8. The change in background index most significantly affects the mode confinement, which drops significantly as the background index increases. The reduction in mode confinement manifests as

the disappearance of the $TM_{11}$ mode resonant absorption peak and a drop in both field intensity and field confinement.

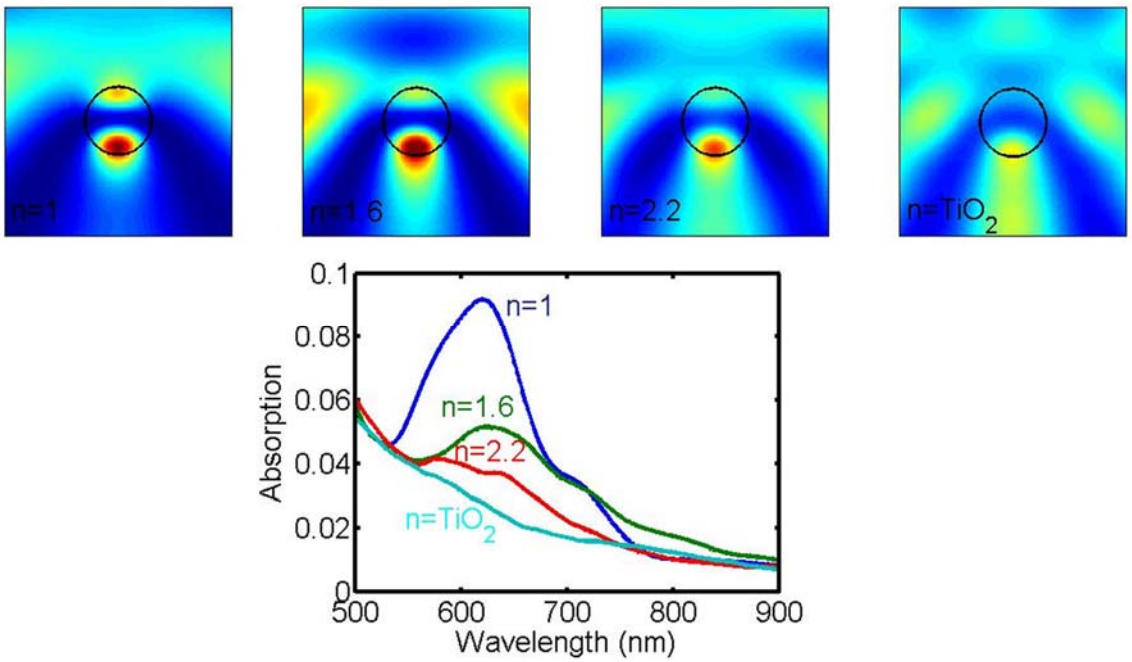


**Figure 53: Absorption vs. wavelength for a 60 nm radius GaAs nanowire with various backgrounds (*n*=1, 1.6, 2.2, $TiO_2$) illuminated side-on with TM polarized light, with electric field intensity profiles displayed at the resonant wavelength of the $TM_{11}$ mode for each background index.**

A collaboration with experimentalists would be advantageous for this study of protective coating incorporation to ensure that the simulations consider reasonable minimal coating thicknesses despite potential optical disadvantages. A similar study of III-V nanowires with catalyst would also be of interest. From the analytic study of the optoelectronic effects of the catalyst layer (Section 1.2.6.1), it is evident that the catalyst component can have substantial detrimental effects on photoelectrochemical device performance. Complex catalyst arrangements that go beyond thin, nearly transparent layers of catalyst should be considered, including catalyst nanoparticles and

their placement. This theoretical study would also benefit from collaboration with experimentalists, who can provide input on optimal catalyst material selections and fabrication capabilities. Initial studies of the effects of protective coatings and catalysts could be isolated, but ultimately the combination of the two on nanowire arrays should be considered.

Beyond optical studies, incorporation of device physics for a complete optoelectronic model of nanowire arrays would also be of interest for both photovoltaic and photoelectrochemical devices. Device physics modeling of nanowires was neglected in this work because optical and electrical characterization of the MOCVD-grown GaAs nanowire arrays indicated that the internal quantum efficiency was near unity. In other nanowire arrays, most notably the etched InP nanowire arrays, inferior electronic material quality is observed. Coupled optoelectronic modeling of nanowire arrays would be useful to determine the necessary electronic properties for high efficiency devices. The role of surfaces and their desired degree of passivation is of particular interest because the greater surface area of nanowire arrays with respect to planar devices is the primary electronic disadvantage of wire arrays.

Continued work on MOCVD growth of GaP nanowire arrays is of interest for $CO_2$ reduction photoelectrochemical devices because GaP in the presence of pyridine has been shown to selectively reduce $CO_2$ to methanol.[97] The high surface area in nanowire arrays would be advantageous for catalysis. Toward this end, growth efforts should focus on the fabrication of p-type GaP nanowires. Additionally, the Bakkers group recently reported growth of wurtzite GaP nanowires with a direct bandgap of 2.08 eV.[116] While the optical efficiency of zincblende, indirect gap GaP nanowires is limited due to long absorption lengths, direct gap GaP nanowire arrays could achieve near-unity broadband absorption, as was predicted for the optimized GaAs nanowire arrays. The catalytic properties of wurtzite GaP in comparison to zincblende GaP for $CO_2$ reduction

requires investigation. Further work is also needed to extend the MOCVD growth of GaP nanowires to InGaP nanowires. InGaP is an ideal tandem partner with Si for both photovoltaic and photoelectrochemical applications.

Further fabrication efforts on the InP nanowire arrays should begin with developing an understanding of the blue-shift in photoluminescence. Towards this end, X-ray diffraction and cross-sectional TEM can be used to probe the crystal structure and visualize any surface layer formation. The next clear direction is the design, fabrication and optical characterization of InP nanowire arrays that are predicted to achieve near-unity absorption. A two-fold simulation-based optimization should be conducted—(1) an optimization based on current etch depths of about 1.5 μm and (2) an optimization using nanowires with lengths of 3 μm. If simulation results indicate that longer wire lengths are necessary for near-unity broadband absorption, improvement of the InP etch selectivity should begin with further investigation of the optimal mask layer (material, deposition method, thickness) and the pseudo-Bosch etch parameters. Another immediate research direction for the InP nanowire arrays is investigation of surface passivation techniques towards improved lifetimes. A simple starting point would be a wet chemical treatment with trioctylphosphine sulfide, which has previously been shown to passivate GaAs.[117] The ultimate goal for the etched InP nanowire arrays would be the fabrication of a peeled-off array into a complete photovoltaic device. The biggest hurdle here will likely be the contact scheme. In general, it would also be interesting to extend this work to other III-V materials, such as InGaP, and potentially tandem systems, as well.

# Appendix A: Supplementary Information on Modeling of Si|$WO_3$

## A.1 Surface Plasmon-Polariton of Aluminum

A plasmon resonance is a resonant oscillation of valence electrons in a material, typically a metal with high carrier concentration and minimal ohmic losses, which occurs when the real part of the relative permittivity crosses zero. This resonance can be excited by light when the frequency of light matches the resonant frequency of the material. The plasmon resonance of a material, $\omega_p$, can be calculated from Equation (38), where $n$ is its free electron concentration, $\epsilon_0$ is the vacuum permittivity, and $e$ and $m_e$ are the charge and mass of an electron, respectively.[6]

$$\omega_p = \sqrt{\frac{ne^2}{\varepsilon_0 m_e}} \tag{38}$$

At the interface between a dielectric material and a metal, a surface plasmon resonance can occur. This resonant frequency, $\omega_{sp}$, is red-shifted with respect to the plasmon resonance as a result of the surface confinement, and this red-shift can be calculated from Equation (39), according to the relative permittivity of the dielectric material, $\epsilon_{mat}$:[45]

$$\omega_{sp} = \frac{\omega_p}{\sqrt{1+\varepsilon_{mat}}} \tag{39}$$

Light can couple into a surface plasmon-polariton (SPP) mode at wavelengths greater than or equal to the surface plasmon resonant (SPR) frequency. The ability of light to couple into modes is determined by the dispersion relations, $\omega(k)$, of light and the material; when the frequency and momentum of light and the material are equal, this coupling freely occurs. However, the dispersion relation of light always lies to the left of that of the material (see Figure 54 below), meaning that an extra source of momentum is needed for the light to couple into the mode; nano-

structured features can provide this momentum. In the core/shell structure, the corners of the wire likely provide this momentum.

From Equation (41) and material data from Kittel,[6] aluminum's plasmon resonance is at $\lambda$=80 nm, which is in the UV region of the spectrum, like most metals. Using Equation (39), the surface plasmon-polariton resonance (SPPR) for an air|Al interface occurs at $\lambda$=113 nm. Figure 54 shows the dispersion relation for this interface. The dispersion relation for the SPP is calculated from Equation (40), where $\epsilon_1$ is the permittivity of aluminum, $\epsilon_2$ is the permittivity of the interfacial material (in this case, air: $\epsilon_2$=1), and $c$ is the speed of light:[45]

$$k = \frac{\omega}{c}\left(\frac{\varepsilon_1\varepsilon_2}{\varepsilon_1+\varepsilon_2}\right)^{1/2} \tag{40}$$

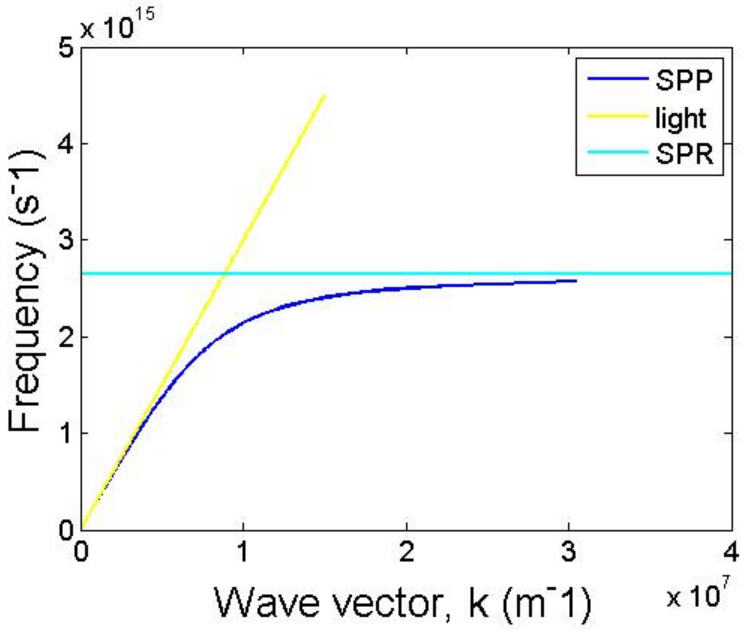


**Figure 54: Dispersion relation for an SPP mode along an air|Al interface overlaid with the dispersion relation of light and the resonant SPP mode of the air|Al interface.**

For an aluminum|$WO_3$ interface, the surface plasmon-polariton resonance is at $\lambda$=208 nm, implying that the entire AM1.5G spectrum can potentially couple into an SPP mode. As discussed in the main text, the existence of an SPP mode was probed via videos of the propagation in time of the electric field along the interface at different wavelengths. The decreased speed of light and evanescent decay of the electric field into the dielectric medium are the two main indicators of an SPP mode. The group velocity of light, *v*, is determined by the derivative of the dispersion relation, Equation (41).

$$\frac{\partial \omega}{\partial k} = \upsilon_g \tag{41}$$

For an SPP mode, the speed at which light propagates, the group velocity, is slower than that of light in free space, and the discrepancy between the two becomes more evident as the resonant frequency is approached (see Figure 54). By observing the propagation of the electric field at 200 nm on an air|Al surface and 250 nm on a $WO_3$|Al surface in the microwire structure, a visible decrease in the speed of propagation along the interface was observed. The evanescent decay of the electric field was readily observable for the air|Al interface, but was too small to unequivocally identify along the $WO_3$|Al interface. All of these characteristics of SPP modes disappeared at wavelengths below the SPR. Based on these observations, an SPP mode definitely contributes to the excessive absorption in the aluminum layer.

## A.2 Opaque Contact Designs and Results

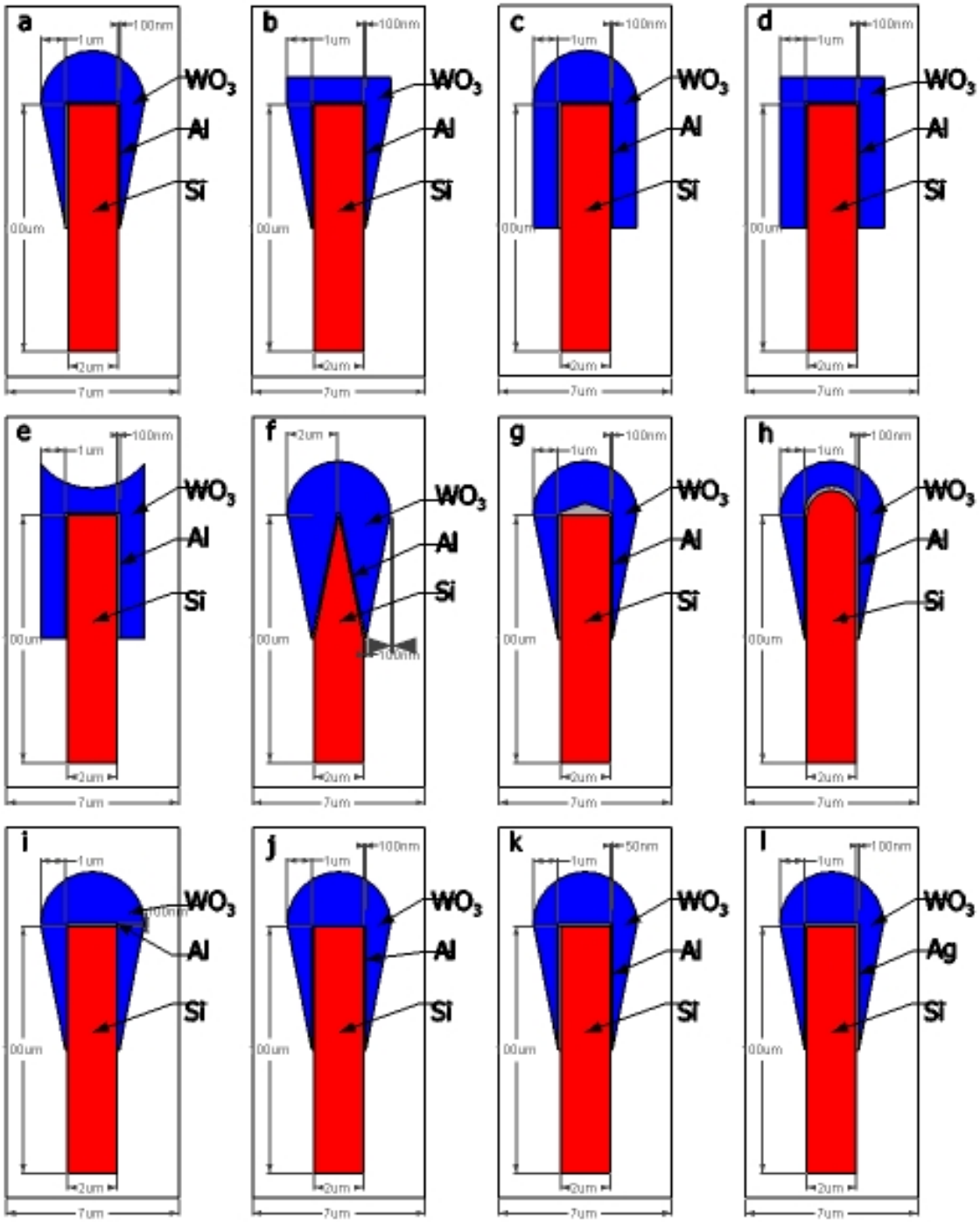

**Figure 55: (a) original design; (b) original design with flat top; (c) original design with untapered $WO_3$ coating; (d) original design combining b and c; (e) original design with opposite concavity; (f) original design with top half of Si shaped as a cone; (g) original design with conical Al; (h) original design with rounded Si and Al; (i) original design with side edges of Al removed; (j) original design with top edge of aluminum removed; (k) original design with 50nm of Al; (l) original design with Ag replacing Al.**

**Table 6: Current densities ($mA \cdot cm^{-2}$) for each variation on the opaque contact design from Figure 55.**

| Model | $j_{Si}$ | $j_{WO3}$ | $j_{Contact}$ | $j_{Ref}$ | $j_{Trans}$ |
|---|---|---|---|---|---|
| a* | 3.21 | 1.46 | 16.72 | 18.07 | 5.52 |
| b | 2.81 | 1.51 | 21.54 | 12.95 | 4.84 |
| c | 2.59 | 1.59 | 14.96 | 17.36 | 6.96 |
| d | 3.61 | 1.74 | 17.69 | 13 | 7.52 |
| e | 2.79 | 1.55 | 23.33 | 11.25 | 4.73 |
| F | 1.97 | 1.95 | 30.97 | 4.43 | 4.27 |
| g | 3.07 | 1.42 | 21.06 | 12.81 | 5.14 |
| h | 2.79 | 1.35 | 13.92 | 20.65 | 4.76 |
| I | 12.04 | 1.15 | 4.63 | 16.92 | 8.66 |
| J | 15.91 | 1.2 | 16.51 | 3.91 | 6 |

| | | | | | |
|---|---|---|---|---|---|
| K | 3.34 | 1.39 | 15.73 | 19.42 | 5.72 |
| L | 5.02 | 1.38 | 10.4 | 19.42 | 7.21 |

*Original opaque contact design discussed in text

## A.3 Transparent Contact Designs and Results

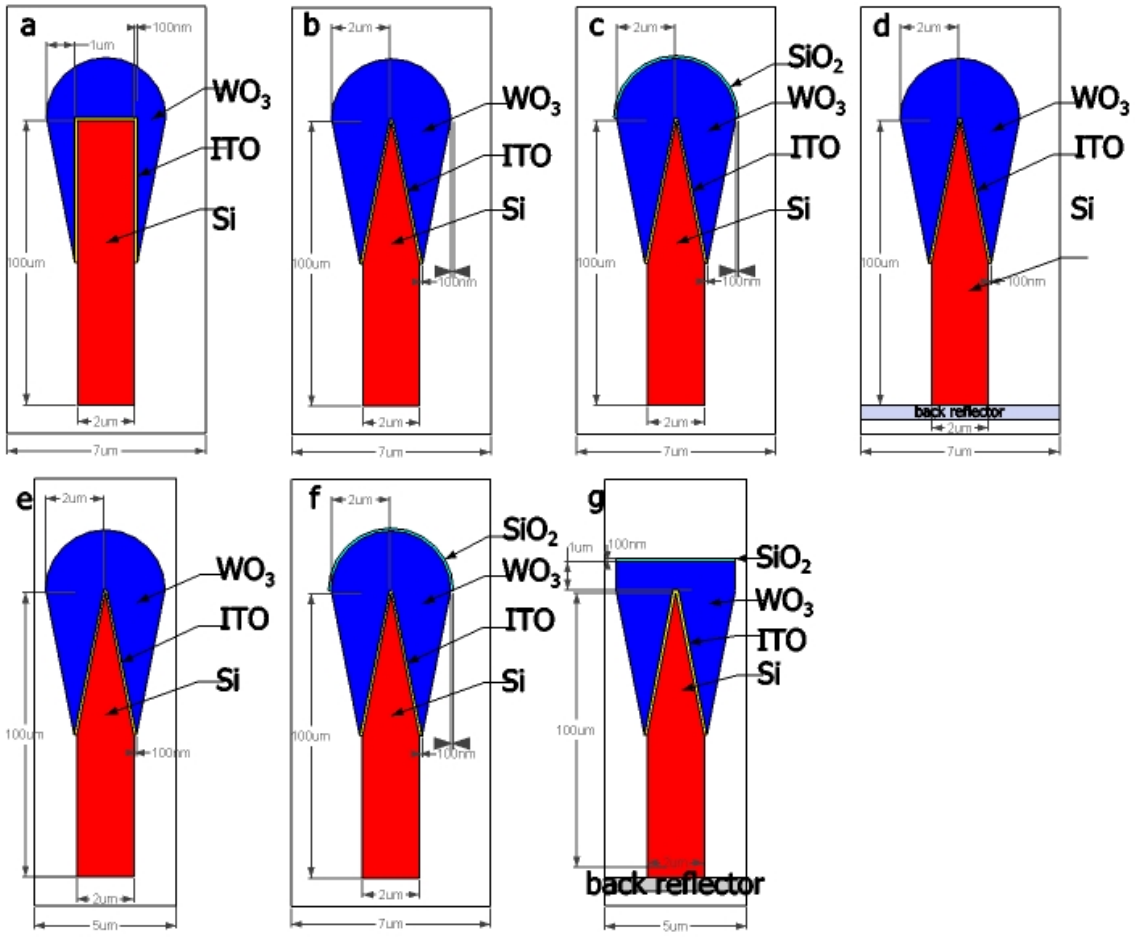


**Figure 56: (a) original transparent contact design; (b) original design with conical top half of Si; (c) design b with 100nm antireflective coating of $SiO_2$; (d) design b with a back reflector; (e) design b with an array pitch of 5µm; (f) combination of design c, d, and e; (g) optimized transparent contact structure.**

**Table 7: Current densities (mA·cm$^{-2}$) for each variation on the transparent contact design from Figure 56.**

| Model | $j_{Si}$ | $j_{WO3}$ | $j_{Contact}$ | $j_{Ref}$ | $j_{Trans}$ |
|---|---|---|---|---|---|
| a* | 28.31 | 1.02 | 2.11 | 5.69 | 7.86 |
| B | 25.58 | 1.91 | 4.82 | 2.47 | 8.83 |
| c** | 28.1 | 2.1 | 5.12 | 1.04 | 8.7 |
| D | 30.91 | 2.61 | 6.66 | 3.54 | 0 |
| E | 29.89 | 2.61 | 6.1 | 3.27 | 1.82 |
| F | 32.66 | 2.77 | 6.86 | 1.43 | 0 |
| g*** | 33.5 | 3.39 | 6.06 | 2.09 | 0 |

# Appendix B: Derivation of Leaky Waveguide Eigenvalue Equation

This derivation is adapted from Linyou Cao's thesis and begins with the electromagnetic wave equations, in which E and H are the electric and magnetic vectorial fields, respectively, ε is permittivity, and μ is the magnetic permeability.

$$\nabla^2 E + \omega^2 \mu\varepsilon E = 0 \tag{42}$$

$$\nabla^2 H + \omega^2 \mu\varepsilon H = 0 \tag{43}$$

The *r* and *ϑ* components of the electric and magnetic fields can be derived from the *z* components of the wave equation, and so the *z* components are considered below.

$$\frac{\partial^2 E_z}{\partial r^2} + \frac{1}{r}\frac{\partial E_z}{\partial r} + \frac{1}{r^2}\frac{\partial^2 E_z}{\partial \theta^2} + \frac{\partial^2 E_z}{\partial z^2} + \omega^2 \mu\varepsilon E_z = 0 \tag{44}$$

$$\frac{\partial^2 H_z}{\partial r^2} + \frac{1}{r}\frac{\partial H_z}{\partial r} + \frac{1}{r^2}\frac{\partial^2 H_z}{\partial \theta^2} + \frac{\partial^2 H_z}{\partial z^2} + \omega^2 \mu\varepsilon H_z = 0 \tag{45}$$

General, separation of variables solutions can be written for the above partial differential equations.

$$E_z(r,\theta,z) = R(r)e^{-j\beta z}\left(\mathrm{A}\cos\left(m\theta\right) + A'\sin\left(m\theta\right)\right) \tag{46}$$

$$H_z(r,\theta,z) = R(r)e^{-j\beta z}\left(\mathrm{B}\cos\left(m\theta\right) + B'\sin\left(m\theta\right)\right) \tag{47}$$

Symmetry, rotational invariance, and field orthogonality leads to the simplification of these field equations.

$$E_z(r,\theta,z) = R(r)e^{-j\beta z}\cos\left(m\theta\right) \tag{48}$$

$$H_z(r,\theta,z) = R(r)e^{-j\beta z}\sin\left(m\theta\right) \tag{49}$$

Substituting these solutions into the partial differential equations for the z-components, multiplying each term by $r^2$ and rearranging gives the following equation, which takes the form of a cylindrical Bessel's differential equation.

$$r^2 \frac{\partial^2 R}{\partial r^2} + r \frac{\partial R}{\partial r} + \left( \left( \omega^2 \mu\varepsilon - \beta^2 \right) r^2 - m^2 \right) R = 0 \tag{50}$$

Therefore, the radial dependence of the *z* field components can be written as a Bessel function. At this point, the solutions inside the cylinder and outside the cylinder diverge because the solution inside the cylinder is real and is best described by a Bessel function of the first kind, *J(r)*, and the solution outside the cylinder is complex for leaky modes and is best described by a Hankel function of the first kind, *H(r)*. Additionally, the $\omega^2\mu\varepsilon$ term is divided into $\omega^2\mu_0\varepsilon_0$ and $\mu_r\varepsilon_r$ and substituted with $k_0^2$, the free space wavevector, and $n^2$, the refractive index. The following equations, for inside ($E_{z,cyl}$) and outside ($E_{z,out}$) the cylinder, respectively, are written for the electric field, where $A_1$ and $A_2$ are unknown coefficients.

$$E_{z,cyl}(r,\theta,z) = A_1 J_m \left( \left( n_{cyl}^2 k_0^2 - \beta^2 \right)^{1/2} r \right) e^{-j\beta z} \cos\left( m\theta \right) \tag{51}$$

$$E_{z,out}(r,\theta,z) = A_2 H_m \left( \left( n_{out}^2 k_0^2 - \beta^2 \right)^{1/2} r \right) e^{-j\beta z} \cos\left( m\theta \right) \tag{52}$$

For further simplification, the transverse components of the wavevector inside and outside the cylinder, $k_{cyl}$ and $k_{out}$, are defined as the radial coefficient in the Bessel argument.

$$E_{z,cyl}(r,\theta,z) = A_1 J_m \left( k_{cyl} r \right) e^{-j\beta z} \cos\left( m\theta \right) \tag{53}$$

$$E_{z,out}(r,\theta,z) = A_2 H_m \left( k_{out} r \right) e^{-j\beta z} \cos\left( m\theta \right) \tag{54}$$

$$H_{z,cyl}(r,\theta,z) = B_1 J_m\left(k_{cyl} r\right) e^{-j\beta z} \sin\left(m\theta\right) \tag{55}$$

$$H_{z,out}(r,\theta,z) = B_2 H_m\left(k_{out} r\right) e^{-j\beta z} \sin\left(m\theta\right) \tag{56}$$

Using continuity of the *z* component of the electric and magnetic fields at the cylinder interface (*r*=*a*), the number of unknowns can be reduced from four to two, shown below for the electric field.

$$E_{z,cyl}\Big|_{r=a} = E_{z,out}\Big|_{r=a} \tag{57}$$

$$A_1 J_m\left(k_{cyl} a\right) = A_2 J_m\left(k_{out} a\right) = A \tag{58}$$

The *z* components of the electric and magnetic fields can then be re-written with only two unknowns, *A* and *B*.

$$E_{z,cyl}(r,\theta,z) = A\frac{J_m\left(k_{cyl} r\right)}{J_m\left(k_{cyl} a\right)} e^{-j\beta z} \cos\left(m\theta\right) \tag{59}$$

$$E_{z,out}(r,\theta,z) = A\frac{H_m\left(k_{out} r\right)}{H_m\left(k_{out} a\right)} e^{-j\beta z} \cos\left(m\theta\right) \tag{60}$$

$$H_{z,cyl}(r,\theta,z) = B\frac{J_m\left(k_{cyl} r\right)}{J_m\left(k_{cyl} a\right)} e^{-j\beta z} \sin\left(m\theta\right) \tag{61}$$

$$H_{z,out}(r,\theta,z) = B\frac{H_m\left(k_{out} r\right)}{H_m\left(k_{out} a\right)} e^{-j\beta z} \sin\left(m\theta\right) \tag{62}$$

The continuity of the $\vartheta$ components of the electric and magnetic fields are used to eliminate the remaining unknowns to obtain the eigenvalue equation. The $\vartheta$ components, $E_\vartheta$ and $H_\vartheta$, are calculated from the following equations from Snyder and Love.[75]

$$E_{\theta,cyl} = \frac{j}{k_{cyl}^2}\left(\frac{\beta}{r}\frac{\partial E_z}{\partial \theta} - \left(\frac{\mu_0}{\varepsilon_0}\right)^{1/2} k_0 \frac{\partial H_z}{\partial r}\right) \tag{63}$$

$$H_{\theta,cyl} = \frac{j}{k_{cyl}^2}\left(\frac{\beta}{r}\frac{\partial H_z}{\partial \theta} + \left(\frac{\mu_0}{\varepsilon_0}\right)^{1/2} \varepsilon_{r,cyl}\mu_{r,cyl} k_0 \frac{\partial E_z}{\partial r}\right) \tag{64}$$

The above equations combined with the continuity of the $\vartheta$ components gives the following two equations.

$$A\left(\frac{\beta m}{a}\right)\left(\frac{1}{k_{cyl}^2} - \frac{1}{k_{out}^2}\right) = -Bk_0\left(\frac{\mu_0}{\varepsilon_0}\right)^{1/2}\left(\frac{J_m'\left(k_{cyl}a\right)}{k_{cyl}J_m'\left(k_{cyl}a\right)} - \frac{H_m'\left(k_{out}a\right)}{k_{out}H_m'\left(k_{out}a\right)}\right) \tag{65}$$

$$B\left(\frac{\beta m}{a}\right)\left(\frac{1}{k_{cyl}^2} - \frac{1}{k_{out}^2}\right) = Ak_0\left(\frac{\varepsilon_0}{\mu_0}\right)^{1/2}\left(\frac{\varepsilon_{r,cyl}\mu_{r,cyl}J_m'\left(k_{cyl}a\right)}{k_{cyl}J_m'\left(k_{cyl}a\right)} - \frac{\varepsilon_{r,out}\mu_{r,out}H_m'\left(k_{out}a\right)}{k_{out}H_m'\left(k_{out}a\right)}\right) \tag{66}$$

Combining these two equations to eliminate *A* and *B* gives the eigenvalue equation for the leaky modes of a cylindrical dielectric waveguide. The ± sign arises from the arbitrary selection of sine and cosine for the $E_z$ and $H_z$ field components and analysis of the field profiles leads to the designation of + for HE ($E_z$ dominant) and – for EH ($H_z$ dominant).

$$\begin{aligned}&\pm\left(\frac{1}{k_{cyl}^2} - \frac{1}{k_{out}^2}\right)^2\left(\frac{\beta m}{k_0 a}\right)^2 \\ &= \left(\frac{\varepsilon_{r,cyl}\mu_{r,cyl}}{k_{cyl}}\frac{J_m'\left(k_{cyl}a\right)}{J_m\left(k_{cyl}a\right)} - \frac{\varepsilon_{r,out}\mu_{r,out}}{k_{out}}\frac{H_m'\left(k_{out}a\right)}{H_m\left(k_{out}a\right)}\right)\left(\frac{1}{k_{cyl}}\frac{J_m'\left(k_{cyl}a\right)}{J_m\left(k_{cyl}a\right)} - \frac{1}{k_{out}}\frac{H_m'\left(k_{out}a\right)}{H_m\left(k_{out}a\right)}\right)\end{aligned} \tag{67}$$

# Appendix C: Coupled Optoelectronic Simulations with Lumerical FDTD and Synopsys TCAD Sentaurus

This appendix describes the general procedure for coupling Lumerical FDTD simulations to Synopsys TCAD Sentaurus. This method is a version of Mike Kelzenberg's method that has been updated to be compatible with later versions of Sentaurus. This appendix includes three separate sets of code that are needed to insert the charge carrier generation profiles calculated from Lumerical results into the Synopsys TCAD Sentaurus simulations. A complete example of this method can be found on the Atwater group wiki (upload date: November 2013).

At the time these simulations were run, this method only worked if all Sentaurus coordinates were positive because the PMIUserField variables extracted the absolute value only (see "xy.cmd" file). This fault was reported to Synopsys and may have been fixed.

The first step is to calculate the carrier generation profile from Lumerical results using the spatially recorded electric field and relative permittivity. For single wavelength Lumerical simulations, use of an override mesh is recommended so that each simulation has an identical mesh. This identical mesh facilitates the creation of the summed carrier generation profile. The carrier generation profile with its *x* and *y* coordinates should be written to a .mat file and saved to the Sentaurus project folder. Additionally, the edges of the *x* and *y* coordinates should be extended very slightly to avoid getting an NaN error from the Matlab interpolation function used in the next step.

The *xy.cmd* shown at the end of this Appendix (Code File 1) extracts the mesh coordinates from the Sentaurus simulation. This file should also be placed inside the Sentaurus project folder (prior to running the sde set up) and the Placements {} commands, shown for silicon here, should be repeated for each material in the simulation.

The end of the sde command file in Sentaurus needs to contain the lines listed in Code File 2 (below). These lines create an empty optical generation set for each region listed (list all regions) and extract the Sentaurus mesh using the xy.cmd file.

The first tdx file (Code File 3 below) outputs the dataset numbers for the PMIUserFields and the OpticalGeneration. These numbers are required for the second tdx file (Code File 4 below), where *ndvx* should be defined as the dataset number for PMIUserField0, *ndvy* as PMIUserField1, and *ndvog* as OpticalGeneration. Additionally, the .bashrc file needs to point to the 2013 version (or newer) of Matlab to avoid any errors when running the second tdx file. This second tdx file is the script that actually interpolates the Lumerical results onto the Sentaurus mesh.

## Code file 1: xy.cmd

```
Definitions {
  AnalyticalProfile "XPosition" {
    Species = "PMIUserField0"
    Function = General(init="", function = "x", value = 10)
  }
  AnalyticalProfile "YPosition" {
    Species = "PMIUserField1"
    Function = General(init="", function = "y", value = 10)
  }
}

Placements {
  AnalyticalProfile "XPosition" {
    Reference = "XPosition"
    EvaluateWindow {
      Element = material ["Silicon"]
    }
  }
  AnalyticalProfile "YPosition" {
    Reference = "YPosition"
    EvaluateWindow {
      Element = material ["Silicon"]
    }
  }
```

```
}
```

## Code File 2: Sde Components

```
# create opticalgeneration dataset and extract mesh for modification with tcl script

(sdedr:define-constant-profile "OptGen" "OpticalGeneration" 0.0)
(sdedr:define-constant-profile-region "OptGen" "OptGen" "n_Si")
(sdedr:define-constant-profile-region "OptGen" "OptGen" "p_Si")
(sdedr:append-cmd-file "xy.cmd")
```

## Code File 3: Tdx File 1

```
set inp n@node|sde@_msh.tdr
TdrFileOpen $inp

# loop through geometries
set ng [TdrFileGetNumGeometry $inp]
puts "Number of Geometries: $ng"

for {set ig 0} {$ig < $ng} {incr ig} {
        set gname [TdrGeometryGetName $inp $ig]
        puts "Geometry $ig is $gname"
        set ns [TdrGeometryGetNumState $inp $ig]
        set nr [TdrGeometryGetNumRegion $inp $ig]
        puts "Number of States: $ns"
        puts "Number of Regions: $nr"
        # loop through states
        for {set is 0} {$is < $ns} {incr is} {
                set sname [TdrStateGetName $inp $ig $is]
                puts "State $is is $sname"
                # loop through regions
                for {set ir 0} {$ir < $nr} {incr ir} {
                        set rname [TdrRegionGetName $inp $ig $ir]
                        puts "Region $ir is $rname"
                        # loop through datasets
                        set nd [TdrRegionGetNumDataset $inp $ig $ir $is]
                        for {set id 0} {$id < $nd} {incr id} {
                                set dname [TdrDatasetGetName $inp $ig $ir $is $id]
                                puts "Dataset $id is $dname"
                                # loop through data values
                                set nv [TdrDatasetGetNumValue $inp $ig $ir $is $id]
                                puts "Number of Values: $nv"
                        }
```

```
                }
        }
}

TdrFileClose $inp
```

## Code File 4: Tdx File 2

```
# specify dataset values of x,y,and optical generation

set ndvx 3
set ndvy 4
set ndvog 5
set ni 1

set inp n@node|sde@_msh.tdr
set out n@node|sde@_optgen.tdr
TdrFileOpen $inp

# loop through geometries
set ng [TdrFileGetNumGeometry $inp]
for {set ig 0} {$ig < $ng} {incr ig} {
        set ns [TdrGeometryGetNumState $inp $ig]
        set nrtot [TdrGeometryGetNumRegion $inp $ig]
        # subtract 2 from nr to avoid looping through contacts
        # make sure your contacts are the final 2 regions
        set nr [expr $nrtot - 2]
        # loop through states
        for {set is 0} {$is < $ns} {incr is} {
                # loop through regions
                for {set ir 0} {$ir < $nr} {incr ir} {
                        set rname [TdrRegionGetName $inp $ig $ir]
                        # create file for writing data to be processed
                        # create file for processing this region's data
                        set filename n@node|sde@_optgen_$rname.csv
                        set fileId [open $filename "w"]
                        # loop through data values of x, y, and optgen datasets and modify
optgen
                        set nv [TdrDatasetGetNumValue $inp $ig $ir $is $ndvog]
                        puts "Now processing $rname region with $nv datapoints..."
                        for {set iv 0} {$iv < $nv} {incr iv} {
                                set xi [TdrDataGetComponent $inp $ig $ir $is $ndvx $iv $ni $ni]
                                set yi [TdrDataGetComponent $inp $ig $ir $is $ndvy $iv $ni $ni]
                                set ni [TdrDataGetComponent $inp $ig $ir $is $ndvog $iv $ni
$ni]
                                puts $fileId "$xi $yi 0.0"
```

```
                        }
                        # run matlab which processes data
                        close $fileId
                        # tried a couple of things to suppress matlab GUI, but can't get it to
work properly
                        # global env
                        # set olddisplay $env(DISPLAY)
                        # set env(DISPLAY) ""
                        # exec matlab -nojvm -nodesktop -nodisplay -nosplash
"optgen('$filename'); quit;"
                        exec matlab -nosplash -r "optgen('$filename'); quit;"
                        # set env(DISPLAY) $olddisplay
                        source output.tcl
                }
        }
}

TdrFileSave $inp $out
TdrFileClose $inp
```

# Appendix D: Light Absorption Enhancement via Mie Scatterers on Wide Bandgap Photoanodes

In Chapter 3, methods for enhancing the optoelectronic performance of a wide bandgap photoanode, $WO_3$, deposited on Si microwires were discussed. This appendix contains a brief study of light absorption enhancement in planar films of wide bandgap photoanodes, using bismuth vanadate ($BiVO_4$) as an example, via the use of cylindrical Mie scatterers. The absorption enhancements obtained from cylindrical Mie scatterers arise from the same physics that govern the light absorption in sparse nanowire arrays, discussed in detail in Chapter 4. They reduce reflection and also scatter the incident beam to enable longer optical path lengths through the underlying thin film. This technique has been previously demonstrated on thin film Si solar cells by Spinelli et al.[48]

$BiVO_4$ is another promising preliminary photoanode candidate because it is stable under basic and oxidizing conditions and has a slightly smaller bandgap (2.4 eV) than $WO_3$, which gives it a limiting efficiency of around 8%.[118] However, the carrier transport properties of $BiVO_4$ are quite poor, and thus, enhancement of light absorption in thin films is essential to maximizing its efficiency. Photoelectrochemical measurements of $BiVO_4$ grown in-house indicate an optimal thickness of 200 nm; therefore, the light absorption optimization results shown in this work study a 200 nm thin film of $BiVO_4$ contacted with 100nm FTO (fluorine-doped tin oxide) to its tandem partner, an optically thick planar silicon substrate. Square lattice arrays of $BiVO_4$, $SiO_2$ and $TiO_2$ cylinders spaced 400 nm apart with varying diameters and heights of 100 nm were placed directly on top of the $BiVO_4$ thin film.

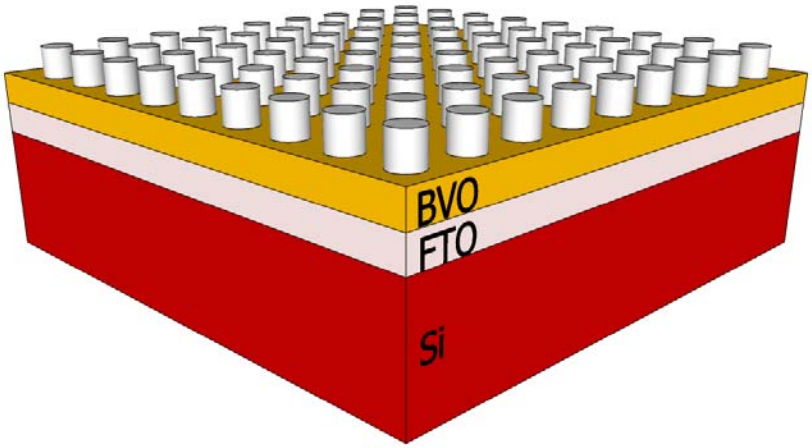


**Figure 57: Schematic of the modeled structure consisting of an optically thick planar layer of Si, a 100 nm layer of FTO (fluorine-doped tin oxide) and a 200 nm thin film of $BiVO_4$ patterned with 100 nm tall cylindrical scatterers in a square array with 400 nm spacing; cylinders vary in radius depending on their material ($BiVO_4$, $SiO_2$, or $TiO_2$).**

Refractive index for $BiVO_4$ was obtained from Zhao et al., who performed theoretical calculations of the refractive index and absorption coefficient of the different crystalline orientations of $BiVO_4$.[119] The following calculations used the polycrystalline data, but it may be important in future experiments with single crystal $BiVO_4$ to consider its optical anisotropy. This refractive index data was found to be in good agreement with other reported experimental measurements.[120,121] Refractive index data for spray-pyrolyzed FTO was obtained from Wang et. al.[122] Refractive index data for $TiO_2$ was measured experimentally with a spectroscopic ellipsometer by M. Kelzenberg. The Lumerical built-in refractive index data for Si and $SiO_2$ were also used.

The optimum radii for $BiVO_4$, $TiO_2$, and $SiO_2$ scatterers were determined from the leaky waveguide eigenvalue equation to be 60, 60, and 120 nm, which places the $TM_{11}$ resonance near the band

edge of $BiVO_4$ (~515 nm). Figure 58 shows the resulting absorption spectra for the $BiVO_4$ thin film compared to the bare planar thin film. Integration these absorption spectra weighted with the AM1.5G spectrum up to the band edge of $BiVO_4$ determined predicted absorbed current densities of 2.27, 2.77, 2.75, and 2.49 $mA \cdot cm^{-2}$ for the bare $BiVO_4$ and the $BiVO_4$ patterned with $BiVO_4$, $TiO_2$, and $SiO_2$ cylinders, respectively. These results reveal that all scatterers improve the light absorption in the $BiVO_4$ thin film. In particular, the $BiVO_4$ scatterers are the most effective, but that the $TiO_2$ scatterers also perform quite well. The $BiVO_4$ scatterers outperform the $TiO_2$ scatterers because they increase the amount of $BiVO_4$ and also because the field enhancement is most prominent in the cylinders themselves. If only the absorption in the thin film is considered, then the case of $BiVO_4$ scatterers only has a predicted absorbed current density of 2.52 $mA \cdot cm^{-2}$. The $TiO_2$ scatterers effectively enhance absorption due to their high refractive index; however, some loss is incurred in the blue (300-350 nm) due to the absorption of $TiO_2$ above the band edge. The low refractive index of $SiO_2$ results in low field enhancement factors and less significant absorption enhancements than in the cases of $TiO_2$ and $BiVO_4$ scatterers.

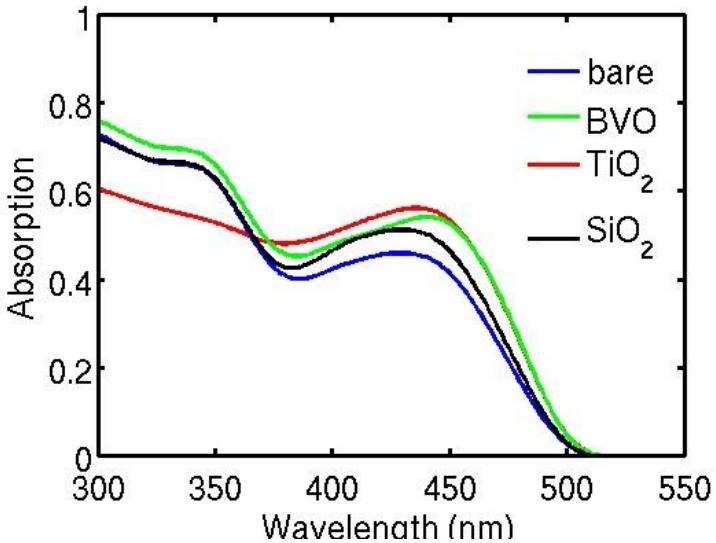


**Figure 58: Simulated light absorption spectra for a 200 nm thin film of $BiVO_4$ patterned with 60, 60, and 120 nm radii cylinders of $BiVO_4$, $TiO_2$, and $SiO_2$, respectively, in a square lattice with a 400 nm spacing.**

Based on these results, the incorporation of $TiO_2$ scatterers represents a promising route to enhance absorption in $BiVO_4$ thin films. These scatterers could be easily fabricated on top of as-grown $BiVO_4$ thin films using $TiO_2$ sol gel and a nanoimprint process.

# Bibliography


[1] U.S. Energy Information Administration (2011). *International Energy Outlook,* Washington D.C.

[2] M. Walter, E. Warren, J. McKone, S. Boettcher, Q. Mi, E. Santori, and N.S. Lewis, "Solar water-splitting cells," *Chem. Rev.* 110, 6446-6473 (2010).

[3] R. Perez, "Making the case for solar energy" *Daylight & Architecture Magazine* 9, 11-17, (2008).

[4] U.S. Energy Information Administration (2014). *Annual Energy Outlook 2014*, Washington D.C.

[5] U.S. Energy Information Administration (2011). *Annual Energy Review 2010*, Washington D.C.

[6] C. Kittel, *Introduction to Solid State Physics, 7th ed.*, New York, NY: Wiley & Sons, Inc (1996).

[7] S. Sze and K. Ng, *Physics of Semiconductor Devices, 3rd ed.*, Hoboken, NJ: John Wiley & Sons (2007).

[8] A.J. Bard and L.R. Faulkner, *Electrochemical Methods: Fundamentals and Applications, 2nd ed.*, New York, NY: John Wiley & Songs (2000).

[9] W. Shockley, and H. Queisser, "Detailed balance limit of efficiency of p-n junction solar cells," *J. Appl. Phys.* 32, 510-519 (1961).

[10] J. Spurgeon and N.S. Lewis, "Proton exchange membrane electrolysis sustained by wáter vapor," *Energy Environ. Sci* 4, 2993-2998 (2011).

[11] M. Tavares, S. Machado, and L. Mazo, "Study of hydrogen evolution in acid médium on Pt micro electrodes," *Electrochimica Acta* 46, 4359-4369 (2001).

[12] M. Lyons, and S. Floquet, "Mechanism of oxygen reactions at porous oxide electrodes. Part 2-Oxygen evolution at $RuO_2$, $IrO_2$ and $Ir_xRu_{1-x}O_2$ electrodes in aqueous acid and alkaline solution," *Phys. Chem. Chem. Phys.* **2011**, 13, 5314-5335.

[13] S. Trasatti, "Work function, electronegativity, and electrochemical behavior of metals. Electrolytic hydrogen evolution in acid solutions," *J. Electroanal. Chem.* 39, 163-184 (1972).

[14] M. Miles, "Evaluation of electrocatalysts for water electrolysis in alkaline-solutions," *J. Electroanal. Chem.* 60, 89-96 (1975).

[15] S. Trasatti, "Electrocatalysis by oxides – Attempt at a unifying approach," *J. Electroanal. Chem.* 11, 125-131 (1980).

[16] A. Polman and H.A. Atwater, "Photonic design principles for ultrahigh-efficiency photovoltaics," *Nat. Mat.* 11, 174-177 (2012).

[17] E. Warren, S. Boettcher, M. Walter, H.A. Atwater, and N.S. Lewis, "pH-independent, 520 mV open circuit voltages of Si/methyl viologen(2+/+) contacts through use of radial n(+)p-Si junction microwire array photoelectrodes," *J. Phys. Chem. C* 115, 594-598 (2011).

[18] H. Gerischer, "Stability of semiconductor electrodes against photodecomposition," *J. Electroanal. Chem.* 82, 133-143 (1977).

[19] S. Chen and L.W. Wang, "Thermodynamic oxidation and reduction potentials of photocatalytic semiconductors in aqueous solution," *Chem. Mater.* 24(18), 3659-3666 (2012).

[20] S. Hu, M.R. Shaner, J. Beardslee, M. Lichtermann, B. Brunschwig, and N.S. Lewis, "Amorphous $TiO_2$ coatings stabilize Si, GaAs, and GaP photoanodes for efficient water oxidation," *Science* 344, 1005-1009 (2014).

[21] B. Kayes, H.A. Atwater, and N.S. Lewis, "Comparison of the device physics principles of planar and radial p-n junction nanorod solar cells," *J. Appl. Phys.* 97, 114302 (2005).

[22] E. Ertekin, P. Greaney, D. Chrzan, and T. Sands, "Equilibrium limits of coherency in strained nanowire heterostructures," *J. Appl. Phys.* 97, 114325 (2005).

[23] E. Garnett and P. Yang, "Light trapping in silicon nanowire solar cells," *Nano Lett.* 10, 1082-1087 (2010).

[24] L. Cao, P. Fan, A. Vasudev, J. White, Z. Yu, W. Cai, J. Schuller, S. Fan, and M. Brongersma, "Semiconductor nanowire optical antena solar absorbers," *Nano Lett.* 10, 439-445 (2010).

[25] S. Haussener, C. Xiang, J. Spurgeon, S. Ardo, N.S. Lewis, and A. Weber, "Modeling, simulation, and design criteria for photoelectrochemical water-splitting systems," *Energy Env. Sci.* 5, 9922-9935 (2012).

[26] M. May, H. Lewerenz, F. Dimroth, D. Lackner, and T. Hannappel, "Efficient solar-to-hydrogen conversion by tailored operando interface transformation," *Submitted to Nat. Comm*.

[27] A. Munoz, C. Heine, M. Lublow, H. Klemm, N. Szabo, T. Hannappel, and H. Lewerenz, "Photoelectrochemical conditioning of MOVPE p-InP films for light-induced hydrogen evolution: chemical, electronic and optical properties," *ECS J. Solid State Sci. Technol.* 2, Q51 (2013).
[28] E. Cussler, *Diffusion: Mass Transfer in Fluid Systems, 2nd ed.*, Cambridge, UK: Cambridge University Press (1997).
[29] G. Pourcelly, "Membranes of low and medium temperature fuel cells. State of the art and new trends," *Petroleum Chem.* 51, 480-491 (2011).
[30] A. Berger, R.A. Segalman, and J. Newman, "Material requirements for membrane separators in a water-splitting photoelectrochemical device," *Energy Env. Sci.* 7 (4), 1468-1476 (2014).
[31] M.D. Kelzenberg, *Silicon Microwire Photovoltaics*, California Institute of Technology (2010).
[32] M.R. Shaner, K.T. Fountaine, S. Ardo, R.H. Corridan, H.A. Atwater, and N.S. Lewis, "Photoelectrochemistry of core-shell tandem junction n-p+ -Si/n-$WO_3$ microwire array photoelectrodes," *Energy Env. Sci.* **7**, 779-790 (2014).
[33] B.M. Kayes, M.A. Filler, M.C. Putnam, M.D. Kelzenberg, N.S. Lewis, and H.A. Atwater, "Growth of vertically aligned Si wire arrays over large areas (>1 $cm^2$) with Au and Cu catalysts," *Appl. Phys .Letters* 91(10), 103110 (2007).
[34] J.R. Bolton, S.J. Strickler and J.S. Connolly, "Limiting and realizable efficiencies of solar photolysis of water," *Nature* **316**(6028), 495-500 (1985).
[35] R.E. Rocheleau and E.L. Miller, "Photoelectrochemical production of hydrogen: Engineering loss analysis," *Int. J. Hydrogen Energy* **22**(8), 771-782 (1997).
[36] T. Iwai, "Temperature dependence of the optical absorption edge of tungsten trioxide single crystal," *J. Phys. Soc. Jpn.* **115**(9), 1596-1600 (1960).
[37] W.A. Gerrard, "Photoelectrolysis using a tungsten-oxide anode in chlorine and sulfate-solutions," *J. Electroanal.Chem.* **86**(2), 421-424 (1978).
[38] Q. Mi, B. Zhanaidarova, B. Brunschwig, H. Gray, and N.S. Lewis, "A quantitative assessment of the competition between water and anion oxidation at $WO_3$ photoanodes in acidic aqueous electrolytes," *Energy & Environ. Sci.* 2, 5694-5700 (2012).
[39] A. Subrahmanyam and A. Karuppasamy, "Optical and electrochromic properties of oxygen sputtered tungsten oxide (WO3) thin films," *Solar Energy Materials and Solar Cells* **91**(4), 266-274 (2007).
[40] K. Sugiyama, H. Ishii, Y. Ouchi, and K. Seki, "Dependence of indium-tin-oxide work function on surface cleaning method as studied by ultraviolet and x-ray photoemission spectroscopies," *J. Appl.Phys.* **87**(1), 295-298 (2000).
[41] E.L. Warren, S.W. Boettcher, M.G. Walter, H.A. Atwater, and N.S. Lewis, "pH-independent, 520mV open-circuit voltages of Si/methyl viologen(2+/+) contacts through use of radial n(+)p-Si junction microwire array photoelectrodes," *J. Phys. Chem. C* 115(2), 594-598 (2011).
[42] A. Leenheer, *Light to electrons to bonds: Imaging water splitting and collecting photoexcited carriers,* California Institute of Technology (2013**).**
[43] K.R. Reyes-Gil, B.S. Brunschwig, and N.S. Lewis, "Enhanced photogenerated carrier diffusion and quantum yields in highly ordered porous $WO_3$ photoanodes for solar water oxidation," *unpublished manuscript*, 1-35.
[44] J. Berak and M. Sienko, "Effect of oxygen-deficiency on electrical transport properties of tungsten trioxide crystals," *J. Solid State Chem.* 2, 109-133 (1970).
[45] H. Raether, *Surface Plasmons*, Berlin: Springer-Verlag (1998).
[46] L. Hu and G. Chen, "Analysis of optical absorption in silicon nanowire arrays for photovoltaic applications," *Nano Lett.* 7, 3249-3252 (2007).
[47] O. Muskens, J.G. Rivas, R.E. Algra, E.P.A.M. Bakkers, and A. Lagendijk, "Design of light scattering in nanowire materials for photovoltaic applications," *Nano Lett.* 8, 2638-2642 (2008).
[48] P. Spinelli, M.A. Verschuuren, and A. Polman, "Broadband omnidirectional antireflection coating based on subwavelength surface Mie resonators," *Nat. Comm.* 3, 692:1-5 (2012).
[49] C. Lin and M.L. Povinelli, "Optical absorption enhancement in silicon nanowire arrays with a large lattice constant for photovoltaic applications," *Opt. Exp.* 17, 19371-19381 (2009).

[50] J. Li, H. Yu, S.M. Wong, X. Li, G. Zhang, P. G. Lo, and D.L. Kwong, "Design guidelines of periodic Si nanowire arrays for solar cell application,"*Appl. Phys. Lett.* 95, 243113:1-3 (2009).
[51] L. Wen, Z. Zhao, X. Li, Y. Shen, H. Guo, and Y. Wang, "Theoretical analysis and modeling of light trapping in high efficiency GaAs nanowire array solar cells," *Appl. Phys. Lett.* 99, 143116:1-3 (2011).
[52] Z. Fan, R. Kapadia, P.W. Leu, X. Zhang, Y.L. Chueh, K. Takei, K. Yu, A. Jamshidi, A.A. Rathore, D.J. Ruebusch, M. Wu, and A. Javey, "Ordered arrays of dual-diameter nanopillars for maximized optical absorption," *Nano Lett.* 10, 3823-3827 (2010).
[53] L. Cao, J.S. White, J.S. Park, J.A. Schuller, B.M. Clemens, and M.L. Brongersma, "Engineering light absorption in semiconductor nanowire devices," *Nat. Mat.* 8, 643-647 (2009).
[54] S.K. Kim, R.W. Day, J.F. Cahoon, T.J. Kempa, K.D. Song, H.G. Park, and C.M. Lieber, "Tuning light absorption in core/shell silicon nanowire photovoltaic devices through morphological design," *Nano Lett.* 12, 4971-4976 (2012).
[55] K. Seo, M. Wober, P. Steinvurzel, E. Schonbrun, Y. Dan, T. Ellenbogen, and K.B. Crozier, "Multicolored vertical silicon nanowires," *Nano Lett.* 11, 1851-1856 (2011).
[56] M.D. Kelzenberg, S.W. Boettcher, J.A. Petykiewicz, D.B. Turner-Evans, M.C. Putnam, E.L. Warren, J.M. Spurgeon, R.M. Briggs, N.S. Lewis, and H.A. Atwater, "Enhance absorption and carrier collection in Si wire arrays for photovoltaic applications," *Nat. Mat.* 9, 239-244 (2010).
[57] J. Kupec and B. Witzigmann, "Dispersion, wave propagation and efficiency analysis of nanowire solar cells," *Opt. Exp.* 17, 10399-10410 (2009).
[58] R.R. LaPierre, "Theoretical conversion efficiency of a two-junction III-V nanowire on Si solar cell," *J. Appl. Phys.* 109, 014310:1-6 (2011).
[59] M. Heiss, E.Russo-Averchi, A. Dalmau-Mallorqui, G. Tutuncuoglu, F. Matteini, D. Ruffer, S. Conesa-Boj, O. Demichel, E. Alarcon-Llado, and A. Foncuberta-Morral, "III-V nanowire arrays: Growth and light interaction," *Nanotech.* 25, 014015:1-9 (2014).
[60] J. Noborisaka, J. Motohisa, and T. Fukui, "Catalyst-free growth of GaAs nanowires by selective-area metalorganic vapor-phase epitaxy," *Appl. Phys. Lett.* 86, 213102:1-3 (2005).
[61] G. Mariani, P. Wong, A.M. Katzenmeyer, F. Leonard, J. Shapiro, and D.L. Huffaker, "Patterned radial GaAs nanopillar solar cells," *Nano Lett.* 11, 2490-2494 (2011).
[62] T. Martensson, P. Carlberg, M. Borgstrom, L. Montelius, W. Seifert, and L. Samuelson, "Nanowire arrays defined by nanoimprint lithography," *Nano Lett.* 4, 699-702 (2004).
[63] A. Deinega and S. John, "Solar power conversion efficiency in modulated silicon nanowire photonic crystals," *J. Appl. Phys.* 112, 074327:1-7 (2012).
[64] L. Hong, Rusli, X. Wang, H. Zheng, H. Wang, and H.Y. Yu, "Design guidelines for slanting silicon nanowire arrays for solar cell application," *J. Appl. Phys.* 114, 084303:1-6 (2013).
[65] A. Chutinan and S. John, "Light trapping and absorption optimization in certain thin-film photonic crystal architectures," *Phys. Rev. A* 78, 023825:1-15 (2008).
[66] B.C.P. Sturmberg, K.B. Dossou, L.C. Botten, A.A. Asatryan, C.G. Poulton, C. Martijn de Sterk, and R.C. McPhedran, "Modal analysis of enhanced absorption in silicon nanowire arrays," *Opt. Exp.* 19, A1067-1081 (2011).
[67] S. Hu, C. Chi, K.T. Fountaine, M. Yao, H.A. Atwater, P.D. Dapkus, N.S. Lewis, and C. Zhou, "Optical, electrical, and solar energy-conversion properties of gallium arsenide nanowire-array photoanodes," *Energy Environ. Sci.* 6, 1879-1890 (2013).
[68] G. Grzela, R. Paniagua-Dominguez, T. Barten, Y. Fontana, J.A. Sanchez-Gil, and J.G. Rivas, "Nanowire antenna emission," *Nano Lett.* 12, 5481-5486 (2012).
[69] Y. Yu and L. Cao, "Coupled leaky mode theory for light absorption in 2D, 1D, and 0D semiconductor nanostructures," *Opt. Exp.* 20, 13847-13856 (2012).
[70] Y.M. Chang, J. Shieh, and J.Y. Juang, "Subwavelength antireflective Si nanostructures fabricated by using the self-assembled silver metal-nanomask," *J. Phys. Chem. C* 115, 8983-8987 (2011).
[71] S. Patchett, M. Khorasaninejad, O. Nixon, and S.S. Saini, "Effective index approximation for ordered silicon nanowire arrays," *JOSA B* 30, 306-313 (2013).
[72] C.M. Gronetand N.S. Lewis, "n-type GaAs photoanodes in acetonitrile: Design of a 10.0% efficient photoelectrode" *Appl. Phys. Lett.* 43, 115–117 (1983).

[73] L.G. Casagrande, A. Juang and N.S. Lewis, "Photoelectrochemical Behavior of n-GaAs and n-$Al_xGa_{1-x}As$ in $CH_3CN$," *J. Phys. Chem. B* 104, 5436–5447 (2000).
[74] B. Ba, H. Cachet, B. Fotouhi, and O. Gorochov, "Orientation-dependent electronic properties of n-type GaAs in contact with various redox systems in acetonitrile and methanol," *Semi. Sci. Tech.* 9, 1529–1534 (1994).
[75] A.W. Snyder and J.D. Love, *Optical Waveguide Theory*, Springer (1983).
[76] L. Cao, *Optical Resonances of Semiconductor Nanowires*, Stanford University (2010).
[77] G. Grzela, *Directional Light Emission and Absorption by Semiconductor Nanowires*, Eindhoven University of Technology (2013).
[78] Y. Yu and L. Cao, "Coupled leaky mode theory for light absorption in 2D, 1D, and 0D semiconductor nanostructures," *Opt. Exp.* 20, 13847-13856 (2012).
[79] N. Anttu and H.Q. Xu, "Efficient light management in vertical nanowire arrays for photovoltaics," *Opt. Exp.* 21, A558-A575 (2013).
[80] B. Wang and P.W. Leu, "Tunable and selective resonant absorption in vertical nanowires," *Opt. Lett.* 37(18), 3756-3758 (2012).
[81] J.D. Joannopoulos, S.G. Johnson, J.N. Winn, and R.D. Meade, *Photonic Crystals: Molding the Flow of Light, 2nd edition*, Princeton University Press (2008).
[82] C. Vandenbem and J.P. Vigneron, "Mie resonances of dielectric spheres in face-centered cubic photonic crystals," *JOSA* 22(6), 1042-1047 (2005).
[83] B.C.P. Sturmberg, K.B. Dossou, L.C. Botten, A.A. Asatryan, C.G. Poulton, R.C. McPhedran, and C. Martijn de Sterke, "Optimizing photovoltaic charge generation of nanowire arays: A simple semi-analytic approach," *ACS Phot.* 1, 683-689 (2014).
[84] E. Yablonovitch, "Statistical ray optics," *J. Opt. Soc. Am.* 72, 899-907 (1982).
[85] Z. Yu, A. Raman, and S. Fan, "Fundamental limit of nanophotonic light trapping in solar cells," *PNAS* 107, 17491-17496 (2010).
[86] D.M. Callahan, J.N. Munday, and H.A. Atwater, "Solar cell light trapping beyond the ray optic limit," *Nano Lett.* 12, 214-218 (2011).
[87] S.L. Diedenhofen, O.T.A. Janssen, G. Grzela, E.P.A.M. Bakkers, and J.G. Rivas, "Strong geometrical dependence of the absorption of light in arrays of semiconductor nanowires," *ACS Nano* 5, 2316-2323 (2011).
[88] H. Cansizoglu, M.F. Cansizoglu, M. Finckenor, and T. Karabacak, "Optical absorption properties of semiconducting nanostructures with different shapes," *Adv. Opt. Mat.* 1, 158-166 (2013).
[89] D.M. Callahan, K.A.W. Horowitz, and H.A. Atwater, "Light trapping in ultrathin silicon photonic crystal superlattices with randomly-textured dielectric incouplers," *Opt. Exp.* 21, 30315-30326 (2013).
[90] C.X. Lin, N.F.Huang, and M.L.Povinelli, "Effect of aperiodicity on the broadhand reflection of silicon nanorod structures for photovoltaics," *Opt. Exp.* 20, A125-A132 (2012).
[91] K. Vynck, M. Burresi, F. Riboli, and D.S. Wiersma, "Photon management in two-dimensional disordered media," *Nat. Mat.* 11, 1017-1022 (2012).
[92] K.X.Wang, Z. Yu, V. Liu, Y. Cui, and S. Fan, "Absorption enhancement in ultrathin crystalline silicon solar cells with antireflection and light-trapping nanocone gratings," *Nano Lett.* 12, 1616-1619 (2012).
[93] B.C.P. Sturmberg, K.B. Dossou, L.C. Botten, A.A. Asatryan, C.G. Poulton, R.C. McPhedran, and C. Martijn de Sterke, "Nanowire array photovoltaics: radial disorder versus design for optimal efficiency," *Appl. Phys. Lett.* 101, 173902: 1-4 (2012).
[94] H. Alaeian, A.C. Atre, and J.A. Dionne, "Optimized light absorption in Si wire array solar cells," *J. Opt.* 14, 024006: 1-6 (2012).
[95] J. Jung, Z. Guo, S. Jee, H. Um, K. Park, and J. Lee, "A strong antireflective solar cell prepared by tapering silicon nanowires," *Opt. Exp.* 18, A286-292 (2010).
[96] P. Mohan, J. Motohisa, and T. Fukui, "Controlled growth of highly uniform, axial/radial direction-defined, individually addressable InP nanowire arrays," *Nanotech.* 16, 2903-2907 (2005).
[97] E.E. Barton, D.M. Rampulla, and A.B. Bocarsly, "Selective solar-driven reduction of $CO_2$ to methanol using a catalyzed p-GaP based photoelectrochemical cell," *J. Am. Chem. Soc.*, 2008, 130(20), 6342-6344.
[98] G.B. Stringfellow *Organometallic Vapor-Phase Epitaxy*, Oxford, UK: Academic Press (1998).

[99] J. Wallentin, L.B.Poncela, A.M. Jansson, K. Mergenthaler, M. Ek, D. Jacobsson, L.R. Wallenberg, K. Deppert, L. Samuelson, D.Hessman, and M.T. Borgstrom, "Single GaInP nanowire p-i-n junctions near the direct to indirect bandgap crossover point," *Appl. Phys. Lett.* 100(25), 251103 (2012).

[100] S. Bhunia, T. Kawamura, Y. Watanabe, S. Fujikara, and K. Tokushima, "Metalorganice vapor-phase epitaxial growth and characterization of vertical InP nanowires," *Appl. Phys. Lett.* 83(16), 3371-3373 (2003).

[101] M. Mattila, T. Hakkarainen, and H. Lipsanen, "Catalyst-free fabrication of InP and InP(N) nanowires by metalorganic vapor phase epitaxy," *J. Crystal Growth* 298, 640-643 (2007).

[102] C.J. Novotny and P.K.L. Yu, "Vertically aligned, catalyst-free InP nanowires grown by metalorganic chemical vapor deposition," *Appl. Phys. Lett.* 87(20), 203111 (2005).

[103] J. Tatebayashi, A. Lin, P.S. Wong, R.F. Hick, and D.L. Huffaker, "Visible light emission from self-catalyzed GaInP/GaP core-shell double heterostructure nanowires on silicon," *J. Appl. Phys.* 108(3), 034315 (2010).

[104] P. Mohan, J. Motohisa, and T. Fukui, "Controlled growth of highly uniform, axial/radial direction-defined, individually addressable InP nanowire arrays," *Nanotech.* 16(12), 2903-2907 (2005).

[105] H.J. Chu, T.W. Yeh, L. Stewart, and P.D. Dapkus, "Wurtzite InP nanowire arrays grown by selective area MOCVD," *Physica Status Solidi C* 7(10), 2494-2497 (2010).

[106] S. Adachi, *Physical Properties of III-V Semiconductor Compounds*, Wiley (1992).

[107] M.D. Henry, *ICP Etching of Silicon for Micro and Nanoscale Devices*, California Institute of Technology (2010).

[108] F. Karouta, "A practical approach to reactive ion etching," *J. Phys. D: Appl. Phys.* 14, 233501 (2014).

[109] M.J. Shearn II, *Silicon Integrated Optics, Fabrication and Characterization*, California Institute of Technology (2010).

[110] B. Docter, E.J. Geluk, M.J.H. Sander-Jochem, F. Karouta, and M.K. Smit, "Deep etching of DBR gratings in InP using $Cl_2$ based ICP processes," *IEEE Proc.* (2006).

[111] M.S. Gudiksen, J. Wang, and C.M. Lieber,"Size-dependent photoluminescence from single indium phosphide nanowires," *J. Phys. Chem. B* 106, 4036-4039 (2002).

[112] M. Mattila, T. Hakkarainen, M. Mulot, and H. Lipsanen, "Crystal-structure-dependent photoluminescence from InP nanowires," *Nanotech.* 17, 1580-1583 (2006).

[113] K.A. Dick, P. Caroff, J. Bolinsson, M.E. Messing, J. Johansson, K. Deppert, L.R. Wallenberg, and L. Samuelson, "Control of III-V nanowire crystal structure by growth parameter tuning," *Semicond. Sci. Technol.* 25, 024009 (2010).

[114] D.M. Fryauf, J. Zhang, K.J. Norris, J.J.D. Leon, M.M. Oye, M. Wei, and N.P. Kobayashi, "Photoluminescence blue shift of indium phosphide nanowire networks with aluminum oxide coating," *Phys. Stat. Solid. RRL* 8(7), 663-667 (2014).

[115] J.M. Spurgeon, J.M. Velazquez, and M.T. McDowell, "Improving $O_2$ production of $WO_3$ photoanodes with $IrO_2$ in acidic aqueous electrolyte," *Phys. Chem. Chem. Phys.* 16(8) 3623-3631 (2014).

[116] S. Assali, I. Zardo, S. Plissard, D. Kriegner, M.A. Verheijen, G. Bauer, A. Meijerink, A. Belabbes, F. Bechstedt, J.E.M. Haverkort, and E.P.A.M. Bakkers, "Direct band gap wurtzite gallium phosphide nanowires," *Nano Lett.* 13, 1559-1563 (2013).

[117] M.T. Sheldon, C.N. Eisler, and H.A. Atwater, "GaAs passivation with trioctylphosphine sulfide for enhanced solar cell efficiency and durability," *Adv. Energy Mat.* 2, 339-344 (2012).

[118] Y. Park, K.J. McDonald, and K. Choi, "Progress in bismuth vanadate photoanodes for use in solar water oxidation," *Chem. Soc. Rev.* 42, 2321-2337 (2013).

[119] Z. Zhao, Z. Li, and Z. Zou, "Electronic structure and optical properties of monoclinic clinobisvanite $BiVO_4$," *PCCP* 13, 4746-4753 (2011).

[120] H. Luo, A.H. Mueller, T.M. McCleskey, A.K. Burrell, E. Bauer, and Q.X. Jia,, "Structure and photoelectrochemical properties of $BiVO_4$ thin films," *J.Phys. Chem. C* 112, 6099-6102 (2008).

[121] J.F. Li, A.S. Bhalla, and L.E. Gross, "Temperature sensitivity of the optical constants of $BiVO_4$," *Opt. Comm.* 92, 115-118 (1992).

[122] K. Wang, Y. Hua, J. Wang, C. Song, S. Jia, G. Han, and Y. Liu, "Optical and structural characterization of $SnO_2$:F/$SiC_xO_y$ tandem thin films by spectroscopic ellipsometry," *Thin Solid Films* 540, 84-91 (2013).